

APPLICATIONS OF SPATIAL FREQUENCY
MODULATION FOR IMAGING IN CELL
DEFORMATION CYTOMETRY

by
Jacob A. Neumann

© Copyright by Jacob A. Neumann, 2018

All Rights Reserved

A thesis submitted to the Faculty and the Board of Trustees of the Colorado School of Mines in partial fulfillment of the requirements for the degree of Master of Science (Applied Physics).

Golden, Colorado

Date _____

Signed: _____

Jacob A. Neumann

Signed: _____

Dr. Jeffrey A. Squier
Thesis Advisor

Golden, Colorado

Date _____

Signed: _____

Dr. Uwe Greife
Professor and Head
Department of Physics

ABSTRACT

In this thesis, we develop two novel system architectures for the measurement of the flow position, size, and shape of red blood cells flowing in a microfluidic channel for the primary purpose of cell elasticity cytometry. The current state of the art relies upon the use of expensive high speed (of order 100 fps) CCD cameras to observe optically stretched red blood cell relaxing from a stretched state. This method also requires the use of computationally expensive edge finding techniques in order to convert the images into useful size information, which is then used to compute the cell elasticity. Our designs are fundamentally derived from the technique SPaItial Frequency modulation for Imaging (SPIFI). SPIFI is a microscopy technique prized for its ability to recover one and two dimensional information using a single element detector, such as a photodiode, instead of a camera. By applying a spatially varying frequency modulation to the excitation source, spatial information is encoded in the frequency spectrum of the beam. The light emitted by the microscope objective can subsequently be collected and analyzed through examination of its periodogram. Because each frequency component is mapped to a spatial location, the amplitude of the periodogram can be used to create an image of our specimen.

We propose two systems that take advantage of the underlying principle of SPIFI (that higher dimensional information can be collected using a single element detector by using spatial modulation of light). The first uses a static Cartesian coordinate SPIFI mask placed directly above a microfluidic channel. We showed qualitatively that such a system is capable of determining the flow position of a target in a microfluidic flow and its size using computational and experimental methods. Our experiment used a laser beam scanning across a mask as a macroscopic correlate of a fluorescent target flowing beneath a mask. Under a set of restrictions generally met by red blood cells, it is even capable of recovering limited information about the shape of the cell. However, the static mask system is unable

to provide reliable shape and size information about the target if its size is changing due to the time-frequency uncertainty principle and the coupling of the target flow speed with frequency and temporal window parameters. High flow speed can cause cell deformation, complicating elasticity measurements. We also demonstrate for the first time that femtosecond laser micromachined masks are capable of modulating light of wavelength 632 nm and 800 nm sufficiently for conventional SPIFI applications, allowing masks to be produced more cheaply and with greater flexibility of configuration.

The second system relies on a spinning SPIFI mask, best described in terms of radial coordinates. The frequency and temporal window are entirely controlled by the mask and spin motor properties, allowing it measure the size of a red blood cell relaxing from a stretched state. We show mathematically that the system collapses the two dimensional information of the target into a one dimensional function which is directly recovered by the examining the periodogram of the signal produced by our system. We then show that we can recover shape information from this function. We also show that our model qualitatively matches experimental results using macroscopic opaque targets.

Both techniques that we demonstrate require further development which can be accomplished rapidly. However, the spinning mask architecture has the most potential due to its ability to measure cell size as it relaxes from a stretched state. As such, further research on the spinning mask system ought to be prioritized.

TABLE OF CONTENTS

ABSTRACT	iii
LIST OF FIGURES AND TABLES	viii
LIST OF ABBREVIATIONS	xii
ACKNOWLEDGMENTS	xiii
DEDICATION	xiv
CHAPTER 1 INTRODUCTION	1
CHAPTER 2 SPIFI MICROSCOPY: CONCEPTS AND PRINCIPALS	5
2.1 Motivation	5
2.2 1-D Line SPIFI with a Spinning Mask	7
2.3 1-D Line SPIFI with a Static Mask	12
2.4 2-Dimensional SPIFI	13
2.5 The Bottom Line	15
CHAPTER 3 THE BEGINNING OF THE JOURNEY	16
CHAPTER 4 MICROFLUIDIC CHANNEL FLOW POSITION AND SIZE CHARACTERIZATION WITH STATIC MODULATION MASKS	19
4.1 Fundamentals and a Primitive Modulation Mask	19
4.2 Mathematical Modeling of Masks	23
4.3 An In Depth Examination of the Primitive Modulation Mask	29
4.4 Modulation Masks for Flow Position Measurement	37
4.4.1 A 3 Row Modulation Mask: Case I	37

4.4.2	A 3 Row Modulation Mask: Case II	43
4.4.3	A 3 Row Modulation Mask: Case III	46
4.4.4	The 3 Row Modulation Mask: A Review	48
4.4.5	A 5 Row Modulation Mask: Case I	49
4.4.6	A 5 Row Modulation Mask: Case II	52
4.4.7	The 5 Row Modulation Mask: A Review and Closer Examination	54
4.5	Laser Micromachined Masks: A brief aside	56
4.6	Experimental Verification of Proof of Concept	57
4.6.1	Simple Testing: Advantages and Reasoning	57
4.6.2	Rudimentary Testing with a Light Based Target	58
4.7	Assigning Meaning to the Shape of the Periodogram	68
4.8	Of Advantages, Disadvantages, and Our Next Steps	73
CHAPTER 5 CELL SIZE MEASUREMENT AND SHAPE CHARACTERIZATION WITH SPINNING MODULATION MASKS		77
5.1	A Spinning Mask Thought Experiment	77
5.2	A Proposed Spinning Mask System	80
5.3	Model and Mathematical Framework	83
5.4	Recovering Shape Information from the Area Function	89
5.5	Experiment and Results	96
5.6	The Next Steps	107
CHAPTER 6 UNTIL NEXT TIME, DEAR READER		110
6.1	A Quick Review	110
6.2	A Final Farewell	114

REFERENCES CITED 115

APPENDIX A OCTAVE CODE FOR STATIC MASK SIGNAL PREDICTION . . 117

 A.1 Detector Output Waveform Modeling 117

 A.2 Octave Code for Creating a Matrix Representation Circular Target 118

APPENDIX B FURTHER EXPLORATION OF THE AREA FUNCTION 119

APPENDIX C SUPPLEMENTAL ELECTRONIC FILES 124

LIST OF FIGURES AND TABLES

Figure 2.1	Multiphoton absorption within a sample	6
Figure 2.2	Basic SPIFI Set Up	7
Figure 2.3	Spinning Mask and Excitation Beam	8
Figure 2.4	Static Mask and Excitation Beam	12
Figure 2.5	A cascaded orthogonal mask 2-D SPIFI microscope	14
Figure 3.1	Static modulation mask placed directly above a microfluidic channel.	17
Figure 4.1	Primitive static modulation mask placed directly above a microfluidic channel.	20
Figure 4.2	Predicted waveform for a 3 units long target with a modulation mask with a spatial period of 6 units.	26
Figure 4.3	Predicted waveform for a 3 units long target with a modulation mask with a spatial period of 10 units.	28
Figure 4.4	Images of Matrix Representations of Circular Targets with Various Resolutions.	28
Figure 4.5	Square Target and Primitive Modulation Mask	29
Figure 4.6	Predicted intensity waveform for a square target under a primitive mask	30
Figure 4.7	Circular target and primitive modulation mask	30
Figure 4.8	Predicted intensity waveform for a circular target under a primitive mask	31
Figure 4.9	Periodogram of predicted signal for a circular target under a primitive mask	32
Figure 4.10	Periodogram with a Blackman and a Hanning window.	33
Figure 4.11	1D Representation of a circular target, and predicted intensity signal.	35

Figure 4.12	A 3 row modulation mask.	38
Figure 4.13	Intensity Signals From 3 Row Modulation Mask.	39
Figure 4.14	Periodogram of Intensity Signals From 3 Row Modulation Mask.	40
Figure 4.15	A 3 row modulation mask with with a circular target flowing beneath both row 1 and row 2.	43
Figure 4.16	Intensity signal produced by target flowing beneath 2 rows equally	44
Figure 4.17	Periodogram of intensity signal produced by target flowing beneath 2 rows equally	45
Figure 4.18	A 3 row modulation mask with with a circular target flowing beneath both row 2 and row 3.	46
Figure 4.19	Intensity signal produced by target flowing beneath rows 2 and 3	47
Figure 4.20	Periodogram of intensity signal produced by target flowing beneath 2 rows unequally	47
Figure 4.21	A 5 channel modulation mask with the target flowing in the center	50
Figure 4.22	Intensity signal produced by target flowing beneath rows 2, 3, and 4. . . .	51
Figure 4.23	Peridogram of intensity signal produced by target flowing beneath rows 2, 3, and 4.	52
Figure 4.24	A 5 channel modulation mask with the target flowing off center beneath rows 3, 4, and 5	53
Figure 4.25	Peridogram of intensity signal produced by target flowing beneath rows 3, 4, and 5.	53
Figure 4.26	System Schematic to determine flow position measurement viability using a static modulation mask.	60
Figure 4.27	2D Cartesian Masks Laser Micromachined onto a glass microscope slide. Image courtesy of Nathan Worts.	61
Figure 4.28	Trace of low spatial frequency sweep with a red diode laser	62
Figure 4.29	Periodogram of Low Frequency Signal	63

Figure 4.30	Trace of high spatial frequency sweep with a red diode laser	65
Figure 4.31	Periodogram of High Frequency Signal	66
Figure 4.32	Trace of intermediate frequency sweep with a Ti:Sapphire laser	67
Figure 4.33	Trace of high sweep with a Ti:Sapphire laser	67
Figure 4.34	Frequency Modulated Line and Rectangular Cursor	69
Figure 4.35	Frequency Modulated Line and Rectangular Cursor	70
Figure 5.1	Frequency Modulated Line and Rectangular Cursor	81
Figure 5.2	Frequency Modulated Line and Rectangular Cursor	82
Figure 5.3	Frequency Modulated Line and Rectangular Cursor	91
Figure 5.4	2 Sets of Targets with Equal Area Functions	92
Figure 5.5	Identical Targets with Different Orientations Producing Different Area Functions	93
Figure 5.6	Frequency Modulated Line and Rectangular Cursor	97
Figure 5.7	Time Varying Signal From Spinning Mask System Without a Target	99
Figure 5.8	Signal Periodogram From Spinning Mask Signal Without a Target	100
Figure 5.9	Modulation Cursor Area Function	101
Figure 5.10	Time Carying Signal from Spinning Mask System With a Circular Target	102
Figure 5.11	Time Carying Signal from Spinning Mask System With a Circular Target	102
Figure 5.12	Time Carying Signal from Spinning Mask System With a Circular Target	103
Figure 5.13	Time Carying Signal from Spinning Mask System With a Circular Target	104
Figure 5.14	Time Varying Signal from Spinning Mask System With a Circular Target	106

Figure A.1	Octave code for Detector Output Waveform Modeling	117
Figure A.2	Octave code for Matrix Representation of Circular Targets	118
Figure B.1	Page 1 of Mathematica Notebook	120
Figure B.2	Page 2 of Mathematica Notebook	121
Figure B.3	Page 3 of Mathematica Notebook	122
Figure B.4	Page 4 of Mathematica Notebook	123
Table 4.1	5 channel modulation mask row spatial periods and temporal frequencies.	50

LIST OF ABBREVIATIONS

Spatial Frequency modulation for Imaging	SPIFI
Charge-Coupled Device Camera	CCD Camera
Fast Fourier Transform	FFT
Spatial Light Modulator	SLM
Finite Impulse Response	FIR
Infinite Impulse Response	IIR
Discrete Fourier Transform	DFT
Short Time Fourier Transform	STFT
Field Programmable Gate Array	FPGA

ACKNOWLEDGMENTS

I would like to offer my gratitude do Dr. Jeffrey Squier for his aid as thesis advisor, and both Dr. Micahel Young and Nathan Worts for their invaluable support and patience with my incessant questions. To my wife, Janessa, thank you for putting up with the late nights, the stress punctuated by moments of jubilation, and supporting me throughout the entire experience.

This work is dedicated to my grandfather, Dr. Herschel Neumann,
whose pursuit and love of physics inspired my own path.

CHAPTER 1

INTRODUCTION

The mechanical properties of cells have been shown to be directly related to human health and disease [1, 2]. Specifically, the modulus of elasticity of various human cells are directly affected by a wide array of diseases and health conditions. These include cancer, malaria, and sickle cell anemia [3]. Such measurements fall under the category of cell cytometry. The emerging field of utilizing biomechanics in human medicine is promising. Cell deformation cytometry, for example, has the potential for both research and diagnostic applications [3]. Deformation of cells can be accomplished through the use of optical stretchers. Optical stretchers, also known as optical traps, utilize lasers to impart forces on the order of tens of piconewtons [4, 5] to the target cells. Red blood cells, having a mean diameter of $8 \mu\text{m}$ [6], are most naturally observed while flowing through microfluidic channels.

Optical stretchers, first demonstrated in 1970, function using the principle of radiation pressure [7]. They are constructed using two opposing laser beams with identical intensity profiles. Each beam must also be slightly divergent [8]. This configuration of lasers accomplishes two things. First, it creates a stable trap with a restoring force. Photons, which carry momentum, will refract at the interfaces of the cell, changing their momentum. For momentum to be conserved, some of this momentum must be imparted onto the cell, which therefore applies a force to the cell. Provided that the cell has a higher index of refraction than whatever medium it is in (which is true of cells in water), the light will impart momentum in such a way as to produce restoring force on the center of gravity of the cell if it drifts away from equilibrium [8]. While the net force on the cell is indeed zero at the center of the trap due force symmetry, a cell is an extended body, not a point mass. Given that refraction takes place at the edges of the cell, the forces will primarily be applied to the surface, causing the cell to stretch parallel to the direction of the opposing beams [8].

The noninvasive nature and force scale lend themselves directly to the stretching of living cells. However, at present, cell deformation cytometry has several limitations. In order for cell deformation measurements to be useful, they must be conducted on a statistically meaningful number of cells [3]. These sorts of measurements used to be done one cell at a time, leading to throughputs of 10 to 100 cells per hour[1]. Such measurement speeds were hardly conducive to widespread research of the biomechanical properties of cells, since, at a minimum, thousands of cells need to be analyzed for the information to be useful.

In 2010, I. Sraj *et al* demonstrated a new technique that increases throughputs up to 100 cells/s [1]: a substantial improvement which represents the current state of the art for red blood cell deformation cytometry. Again, increased rates are essential to making cell deformation cytometry more useful for both diagnostic and research purposes. The technique used by I. Sraj *et al* is fairly simple, but is remarkably powerful. Red blood cells flow through a microfluidic channel, and are stretched using a diode-bar optical stretcher. The diode-bar stretcher operates on the same principles as a more conventional optical stretcher. However, instead of having a single stable point where stretching occurs, the cells are stretched along a laser beam line [5]. The extended beam line, when oriented parallel to the cell flow, allows the red blood cell to be stretched without pausing the flow. I. Sraj *et al* utilized a 5 Watt, 1 x 200 μm single laser emitter, generating 808 nm light for in flow cell stretching [1]. The microfluidic channels utilized were 15 μm deep and 150 μm wide [1].

Care must be taken not to deform the cell (of diameter 6 to 8 μm) more than about 15%, as doing so can result in permanent deformation[1]. As the cell relaxes, images are collected. Given that the time constant of the red blood cell relaxation is $\tau = 0.10 \pm 0.02\text{s}$, the image sampling rate must be about an order of magnitude faster in order to collect sufficient data. [1, 2]. These images are collected using a high frame rate (100 frames per second was used by I. Sraj *et al*) CCD camera as the cell is stretched and then relaxes to its rest state[1]. A 2 to 3% stretch along the major axis of the cell was achieved by I. Sraj *et al*, and was sufficient for elasticity measurement [1]. These images are then processed by a

contour detection algorithm to quantify how the shape of the cell changes with time. These measurements are then used to compute the elastic modulus of the target red blood cell by examining how long the cell takes to relax from a stretched state[1]. Specifically, a simple exponential decay function fits the cell relaxation profile [1].

While the method does achieve high enough throughputs to be viable for some research applications, it is not without its drawbacks. First, the image analysis required to compute the red blood cell elasticity is somewhat computationally expensive. The second, and largest draw back is the use of a Charge-Coupled Device (CCD) camera. High speed CCD cameras can easily cost \$ 5000. In order to increase throughput, it would be desirable to parallelize this set up by having several microfluidic streams. This would require the purchase of multiple CCD cameras, which drives up the cost of the system substantially. Due to the high cost, only the most well funded laboratories would be in a position to construct such a set up. The cost poses a serious obstacle for inexpensive implementation and widespread deployment of cell deformation cytometry systems. The final drawback to this system is that it falls under the category of “lab surrounding a chip” instead of a “lab on a chip”. Miniaturization of a cell deformation cytometry system is another crucial aspect that must be developed, and the closer one can get to the “lab on a chip” ideal, the more mobile it will be. The ability of a cell deformation cytometry system to be easily portable is crucial to field deployment, making it more viable for diagnostic applications.

In this thesis, we present two novel methods for measuring cell size in a microfluidic channel utilizing a single element detector, based on principals of of a technique called SPatIal Frequency modulation for Imaging, or SPIFI. The proposed techniques would be used instead of a CCD camera to observe how a stretched cell relaxes back to its rest state over time. We recall that the relaxation time observed by Sraj I. *et al* was approximately $\tau = 0.10 \pm 0.02$ s The key advantage that these proposed techniques have is their low expense, making parallelization and widespread more viable. Additionally, we present a novel method of measuring the flow position of a target in a microfluidic flow using a similar approach.

The goal of this research is to determine the viability of these methods. The ultimate intent of this direction of research is to design a high throughput (of order 1000 cells/s) cell deformation cytometry system that can be inexpensively implemented and readily deployed. The hope is that such a device would be financially accessible enough to be used in a large number of labs and be used in regions of the world where other forms of diagnostics are not available or impractical. Obviously, the time constraints of a masters' thesis preclude seeing the concepts fully turned into a viable system. Thus our goal is to demonstrate a proof of concept for these new techniques so as to justify further work and in this area by others, hopefully one day bringing such a system to fruition.

CHAPTER 2

SPIFI MICROSCOPY: CONCEPTS AND PRINCIPALS

The concepts used to design the proposed new methods for cell measurement in a microfluidic channel rely on principals borrowed from SPIFI microscopy. As such, it is appropriate to give a brief survey of the motivation and techniques that SPIFI uses. There are a few different approaches utilized by SPIFI, all of which will be summarized, as the different approaches informed and inspired this research substantially. The work done in the field of SPIFI microscopy was critical to our thesis, and those who furthered it have our thanks.

2.1 Motivation

The core concepts of SPIFI were first shown by Sanders, et al. in 1991 [9]. This work was further developed into the more modern techniques by Futia, et al in 2011. Development of SPIFI was, in part, motivated by the goal of rapid imaging in scattering media, such as biological tissue. Conventional multiphoton microscopy, for instance, can produce images up to $500 \mu\text{m}$ deep within tissue samples[10–12]. For biological applications, the laser light has wavelengths between 700 and 1000 nm with ultra short pulse durations: optimally on the order of 100 fs [12–14]. The infrared band is wonderful for imaging as most biological samples have low absorption coefficients in this regime [14]. An average power of 700 -100 mW is also typical, as such power levels prevent tissue damage[14]. Ti:Sapphire lasers are well suited for producing light of the appropriate wavelength and pulse duration, and are often utilized for biological multiphoton microscopy. The approach uses nonlinear optical effects, including two-photon excitation fluorescence, second-harmonic generation, third-harmonic generation, sum-frequency generation, and stimulated Raman scattering [11].

In order to take advantage of these nonlinear effects, photon fluxes greater than 5×10^{24} photons $\text{cm}^{-2}\text{s}^{-1}$ are needed [12, 14]. The use of infrared light (which is poorly absorbed by tissue) allows focal points to exist hundreds of micrometers within the sample. The

requirement for high photon flux means that the nonlinear behavior of interest will take place around the focal point. By taking advantage of these nonlinear effects, lower energy light (infrared instead of ultraviolet) can be used, resulting in less collateral damage to the sample as the light moves through to the target to the focal point, as shown in Figure 2.1. By focusing the light at one point within the sample and then collecting all of the light with a single pixel detector, such as a photodiode, the issue of scattering is minimized. Multiphoton microscopy has allowed for less invasive imaging to be done on living tissue and animals [12].

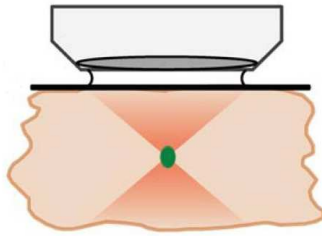


Figure 2.1: Multiphoton absorption within a sample [13]

Unfortunately, conventional multiphoton microscopy is not without a weakness: it can image only one point on the sample at a time. If multiple sample locations are imaged, the issue of scattering returns with a vengeance. A single pixel photoelectric would have to be replaced with a multiple pixel measurement device, such as a CCD. Because biological media scatters light strongly, the signal to noise ratio is decreased. This slows down practical imaging considerably, as it forces the beam to perform a raster scan across the whole sample to construct a complete image.

SPIFI was an answer to this problem. SPIFI is an imaging technique that allows multiple parts of the sample to be imaged (several points at different depths, a line on the sample, or even a two dimensional region of the sample) simultaneously using an extended excitation beam while still making use of a single element photodetector. The exact techniques and principles will be discussed in the next sections.

2.2 1-D Line SPIFI with a Spinning Mask

The underlying principle used by SPIFI is that the excitation beam has its intensity modulated spatially across the spatial extent of the beam at an intermediate image plane. The source of the excitation beam is generally a laser, though the use of light emitting diodes has been shown to a viable option [15]. Each pixel in the excitation beam, and therefore on the sample, has a unique modulation frequency [16]. Light from the sample can then be collected using a single element detector, such as a photodiode or a photomultiplier tube. The voltage output of the detector will be a time varying signal that is encoded with spatial information about the object, and can be recovered by examining its periodogram [16].

One method of applying a spatial frequency modulation to the excitation beam is shown in Figure 2.2. An excitation beam (generally produced by a laser) is sent through a cylindrical lens, which focuses the input light into a line.

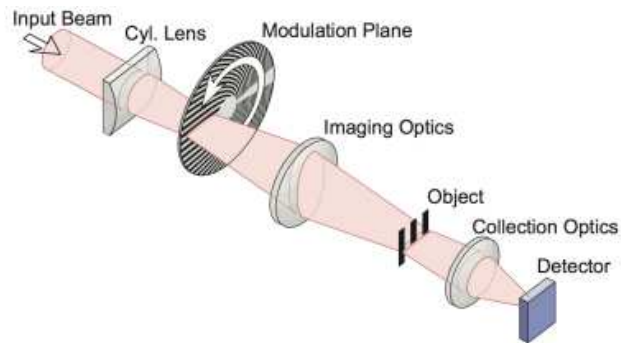


Figure 2.2: Basic SPIFI Set Up [16]

The beam cursor is then focused onto the spinning mask, which applies an intensity modulation with a linear frequency chirp along the radius of the mask, as shown in Figure 2.3. With the spatial information encoded in temporal intensity modulation, the excitation beam is then imaged to the specimen plane. The light is subsequently collected and measured by a single element detector.

Figure 2.3 illustrates the nature of the intensity modulation frequency sweep. Parts of the beam closer to the center of the mask get modulated at a lower frequency than parts

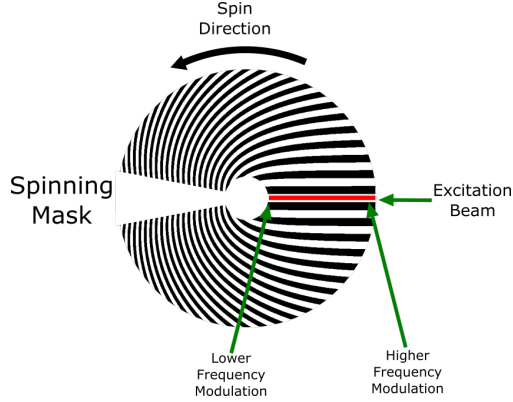


Figure 2.3: Spinning Mask and Excitation Beam

closer to the edge. This relationship will be more apparent when we define its modulation properties. The mask is designed to have a linear chirp along its radius, translating into a linear intensity modulation frequency sweep of the excitation beam. The spinning masks that are generally used are defined by [16]

$$m(R, \theta) = \frac{1}{2} + \frac{1}{2} \cos[(k_0 + \Delta k R)\theta] \quad (2.1)$$

where R is the radial coordinate, and θ is the angular coordinate relative to the center of the mask. k_0 and Δk are free parameters, that control the frequency composition of the modulated excitation beam. By knowing the exact parameters of the mask and rate of spin, one can determine the exact mapping of spatial locations to temporal frequencies [15]. By scanning the line cursor across the extent of the imaging objective, it is possible to create a complete image of the target.

The theory and mathematical machinery of spinning mask SPIFI is derived and developed in [16], and is detailed here. The mathematical approach used for 1D line SPIFI is directly used in one of the proposed cell size measurement techniques, and is therefore necessary to review.

We begin by examining the transverse excitation beam that has been focused to a line by a cylindrical lens in the modulation dimension (we shall use x). The field can be modeled

as

$$E(x, t) = E_0 u(x) e^{i\omega_0 t} \quad (2.2)$$

where $u(x)$ is the normalized spatial profile field along the line and w_0 is the optical carrier frequency. This excitation beam is then modulated in both the spatial and temporal domains by the spinning mask, represented as a time and space dependent function $m(x, t)$. Finally, the modulated beam encounters with the sample. The interaction can be modeled by multiplying the field by a spatially varying function, $g(x)$, which models the transmission of light through the sample. When working with fluorescent microscopy, $g(x)$ can be used to represent the concentration of fluorophores, so that the field becomes the light emitted by the sample, instead of blocked by the sample. With this information, we can determine that the electric field at the focal plane of the imaging objective can be modeled as

$$E(x, t) = E_0 u(x) m(x, t) g(x) e^{i\omega_0 t}. \quad (2.3)$$

Single element detectors, such as photodiodes do not measure the electric field, but the intensity. The intensity of light at the object is therefore given by

$$I(x, t) = I_0 |u(x) m(x, t) g(x)|^2. \quad (2.4)$$

When using a spinning modulation mask defined by Equation 2.1 to modulate a beam line, we can model its modulation properties with

$$m(x, t) = \frac{w(t)}{2} [1 + \cos(2\pi\kappa xt)] \quad (2.5)$$

where $w(t) = \text{rect}(\frac{t}{T_m})$ (T_m is the rotational period of the mask) and $\kappa = \frac{\Delta k}{T_m}$. Recall that Δk is a free parameter used to define the modulation pattern in Equation 2.1. It is worth noting that $w(t)$ is a window function, representing one cycle of the rotating mask. Plugging Equation 2.5 into Equation 2.3, we can model the intensity of light transmitted through (or emitted from) the imaging objective as

$$I(x, t) = I_0 \frac{1}{4} |u(x) g(x) w(t)|^2 \left[\frac{3}{2} + 2 \cos(2\pi\kappa xt) + \frac{1}{2} \cos(4\pi\kappa xt) \right] \quad (2.6)$$

This light is imaged to a single element detector, which measures the intensity in question. Specifically, it will generate a time varying signal (a photocurrent) that can be described by

$$s(t) = \gamma \int I(x, t) dx \quad (2.7)$$

where γ is a catch-all constant factor used to account for things such as detector efficiency, and the integral is computed over the extent of the detector. Assuming that the optics are properly set up, all light from the sample will be mapped to the detector, so no information will be lost. The signal generated can be written as $s(t) = \frac{\gamma I_0}{4} [s_0(t) + s_1(t) + s_2(t)]$, where the terms are:

$$s_0 = \frac{3}{2} w(t) \int |u(x)g(x)|^2 dx \quad (2.8)$$

$$s_1(t) = \Re\{|w(t)|^2 \int |u(x)g(x)|^2 e^{j2\pi\kappa t x} dx + c.c\} \quad (2.9)$$

$$s_2(t) = \Re\{\frac{1}{4}|w(t)|^2 \int |u(x)g(x)|^2 e^{j4\pi\kappa t x} dx + c.c\}. \quad (2.10)$$

The cosine terms in Equation 2.7 are converted to the real part of complex exponentials for mathematical convenience and to allow for a clever application of Fourier analysis. We restrict our focus to $s_1(t)$ and $s_2(t)$: the two harmonics of the fundamental modulation frequency. Both sidebands contain the same information, so we shall further restrict our attention to the first sideband, Equation 2.9. Upon closer examination, Equation 2.9 looks like a spatial Fourier transform. Indeed, by making the substitution $f_x = \kappa t$, we can define

$$G(f_x) = \int |u(x)g(x)|^2 e^{i2\pi f_x x} dx = \mathcal{F}\{|u(x)g(x)|^2\} \quad (2.11)$$

which allows us to rewrite Equation 2.9 as

$$s_1(t) = |w(t)|^2 G(\kappa t). \quad (2.12)$$

Equation 2.12 clearly shows that the output signal of the single element detector has the spatial information from the sample: a truly remarkable result. However, it is possible to go one step further. By taking the Fourier transform of Equation 2.12 we see that the frequency

spectrum (upper sideband) can be written as

$$S(x = f\kappa^{-1}) = \mathcal{W}(\kappa x) * |u(x)g(x)|^2 \quad (2.13)$$

where f is the signal frequency, $*$ is the convolution operator, and $\mathcal{W}(x) = \mathcal{F}\{|w(t)|^2\}_{f=k\kappa}$. The resolution of the frequency spectrum, and therefore the spatial information, is limited by the temporal window. The effects of this window can be mitigated by making use of multiple window spectrum estimation approaches. However, due to the fact that all real measurements have finite time windows, the spectral leakage caused by the choice of window cannot be ignored. Equation 2.13 yields a powerful result: spatial information can be recovered by examining the frequency spectrum of the time varying signal generated by a single element detector. The power of the previous statement is remarkable: it allows images to be created with an inexpensive single element detector. By sweeping the excitation beam across the sample and examining the signal generated at each point along the sample, an image of the target is constructed by taking FFT's of the signal. The utility of this technique, though especially useful when imaging scattering media, is powerful as it allows one to avoid using a two dimensional detector such as a charge coupled device.

When implementing this method of SPIFI, the center of the spinning modulation mask is attached to a motor. Ideally, the mask will rotate perfectly about its own center, resulting in the behavior that we expect in the previous derivation. However, it is important to account for wobble in the spinning mask. This wobble causes distortions to the frequency spectrum of the signal, and thereby distorts the resulting image [17]. Fortunately in 2016, Jeffery Field and Randy Bartels developed a technique to measure the signal aberrations and then remove them from the signal, allowing a wobble corrected image to be constructed [17]. It is worth noting that the difficulty in centering the mask is a disadvantage of this particular SPIFI technique, as the aberration correction will never be perfect.

2.3 1-D Line SPIFI with a Static Mask

With the fundamentals of SPIFI investigated, it is appropriate to consider other techniques inspired by theory discussed in [16]. Another method for applying a spatial frequency chirp to an excitation beam is a static modulation mask. Such a mask is defined by

$$M(x, y) = \frac{1}{2} + \frac{1}{2} \cos[2\pi kxy] \quad (2.14)$$

where k is a parameter controlling the spatial frequency. In this mask, y-axis information is encoded into amplitude modulation of the excitation beam by sweeping the line cursor back and forth in the x-direction as shown in Figure 2.4. Generally, a cylindrical lens is used to focus the beam into a line cursor. A scan mirror and scan lens are used to sweep the beam line across the mask. The cursor is then imaged to the focal plane of the microscope objective. As before, the light is then collected and imaged onto a single element photodetector, such as a photodiode or a photomultiplier tube.

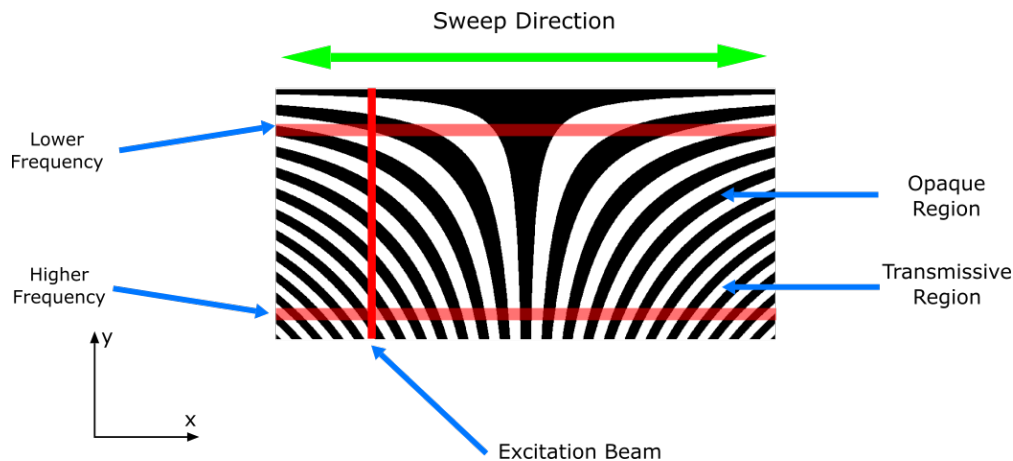


Figure 2.4: Static Mask and Excitation Beam

In the case of a static mask, there is a linear frequency chirp in the y-direction. As light is swept back and forth along the x-direction, different amplitude modulation frequencies are applied at different locations along the y-axis. In Figure 2.4, higher y-values are modulated at a higher frequency, and vice versa. A closer look at Equation 2.14 further illustrates that higher constant y values have higher spatial frequencies, which when sweeping a beam across

the mask, translates into higher temporal frequencies.

One advantage to using this approach is that the modulation mask need not be placed on a motor, thus eliminating the wobble issue. This does require that the laser sweep be aligned properly with the mask. In addition to fabricating a mask, it is possible to make use of a Spatial Light Modulator, often referred to as an SLM, as a transmissive mask. SLMs allow for custom mask geometry and the ability to modify the mask on the fly. The use of SLMs does have a key limitation. SLMs are expensive, specialized pieces of equipment. Typical prices range from \$15,000 - \$25000, which dramatically limits the number of users who can afford to purchase them.

This technique of using a static modulation mask is in its infancy, but has shown promise. An in depth discussion of the mathematical models used for this technique is not included here, as the specifics are not terribly relevant to the techniques developed in this thesis. However, the concept of using a static mask with a spatial frequency chirp as described is a principal utilized by two of the proposed cytometry techniques in this thesis.

2.4 2-Dimensional SPIFI

Both of the previous sections have discussed using SPIFI to image a 1-D line cursor. This necessitates sweeping the line cursor across the sample to create a complete image. This is not always desirable, especially if attempting to perform *in vivo* high speed image acquisition of living biological tissue (creating a video). David Winters and Randy Bartels designed and implemented a solution to this problem [18] [19] utilizing principals of spinning mask SPIFI.

The method designed by Winters and Bartels is to use a pair of spinning SPIFI masks that impart spatial frequency modulation in the x and the y direction [19]. As such, each point in the xy plane will have a different frequency modulation that can be identified in the detector output signal. The photodetector integrates the intensity in two dimensions, changing the form of Equation 2.7 to a double integral. The derivation of the signal for two dimensional SPIFI is rather similar to that of 1-D SPIFI [19], and will not be summarized here.

The general set up, shown in Figure 2.5, is fairly simple. A cylindrical lens is used to focus an excitation beam into a line onto the first spinning modulation mask. The beam was then collimated along its vertical axis and focused to a line at the focal plane of the second spinning SPIFI mask and modulated again. The modulated excitation beam is then imaged to the focal plane of the microscope objective. The signal light is subsequently collected by a single element photodetector. As in the case of 1-Dimensional SPIFI, by examining the frequency spectrum of the signal generated by the detector, it is possible to construct an image of the sample. However, in this case, there is no line cursor that must be swept across the sample. A two dimensional region of the sample (or even all of the sample depending on relative sizes of the excitation beam and the imaging objective) is imaged simultaneously. The increase in complexity of the system is not large, yet the benefits are substantial.

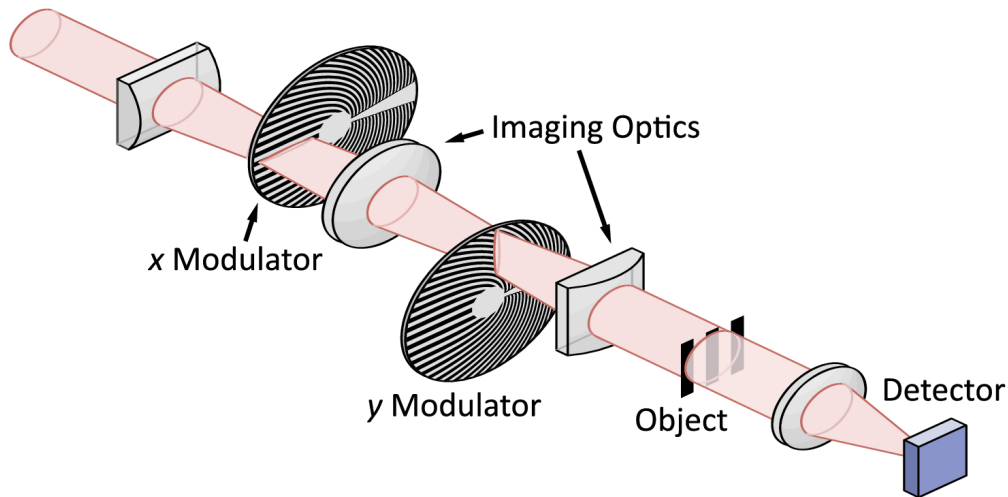


Figure 2.5: A cascaded orthogonal mask 2-D SPIFI microscope[18]

The technique of 2-Dimensional SPIFI is early in its development, but has been shown to be viable for a wide variety of applications. As stated previously, the derivation mathematical model for this technique is not included here, as the specifics are not utilized by our research. However, the concept of using a two dimensional excitation beam as opposed to a line cursor was borrowed from this technique. Its relevance will be seen in a later chapter.

2.5 The Bottom Line

While there are some differences in the various SPIFI techniques showcased in this chapter, they share a common principle: by assigning different amplitude modulation frequencies to different spatial locations on the sample, image recovery is possible by using a single element detector and examining the signal frequency spectra. The ability to image scattering media with a fairly simple and inexpensive system is powerful, and may help a wide variety of researchers to gather accurate images of biological samples, aiding in medical research. The concepts, principles, mathematics, and techniques discussed in this chapter were used to inspire the proposed techniques in this thesis. As such, we owe the scientists who developed these techniques a debt of gratitude.

CHAPTER 3

THE BEGINNING OF THE JOURNEY

Before delving into the techniques proposed in this thesis, it is appropriate to examine the initial parameters and goals given, so as to illustrate the steps and thought process behind each iteration for this research. The initial goal assigned was to design a static transmissive modulation mask that could be placed directly on a microfluidic channel that would allow image recovery of targets (specifically red blood cells) flowing in the channel. The desire was to design a SPIFI system that would more closely resemble a lab on a chip, as opposed to a lab surrounding a chip. Additionally motivating this direction of research was the hope of designing a new technique for measuring cell size for cell deformation cytometry. We discovered that such a system would not provide images without substantial modification. To explain, we first examine the standard SPIFI techniques.

A conventional SPIFI microscope possesses two degrees of freedom. The first is a result of the linear frequency sweep imparted onto the excitation beam by the modulation mask (be that a spinning mask or the beam being swept across a static mask). The second degree of freedom comes from the system's ability to scan the excitation beam across the sample. In a microfluidic channel, the cell is being transported and can flow across the excitation region. These two degrees of freedom allow a SPIFI microscope system to recover an image from the sample.

Consider for a moment the set up proposed initially: A two-dimensional static mask, perhaps like the mask described in Equation 2.14, placed directly above a transparent microfluidic channel with an illumination source under the channel shining light through, as shown in Figure 3.1. Red blood cells tagged with a fluorescent dye flow beneath the mask in the x direction. This results in the cell flowing transiting beneath transmissive and blocking regions of the mask. The number of transitions is dependent upon the spatial frequency of

the mask, which varies along the y axis. These transitions result in the cell transmitting fluorescent light under the transmissive regions and then having that fluorescence being blocked under the opaque regions of the mask.

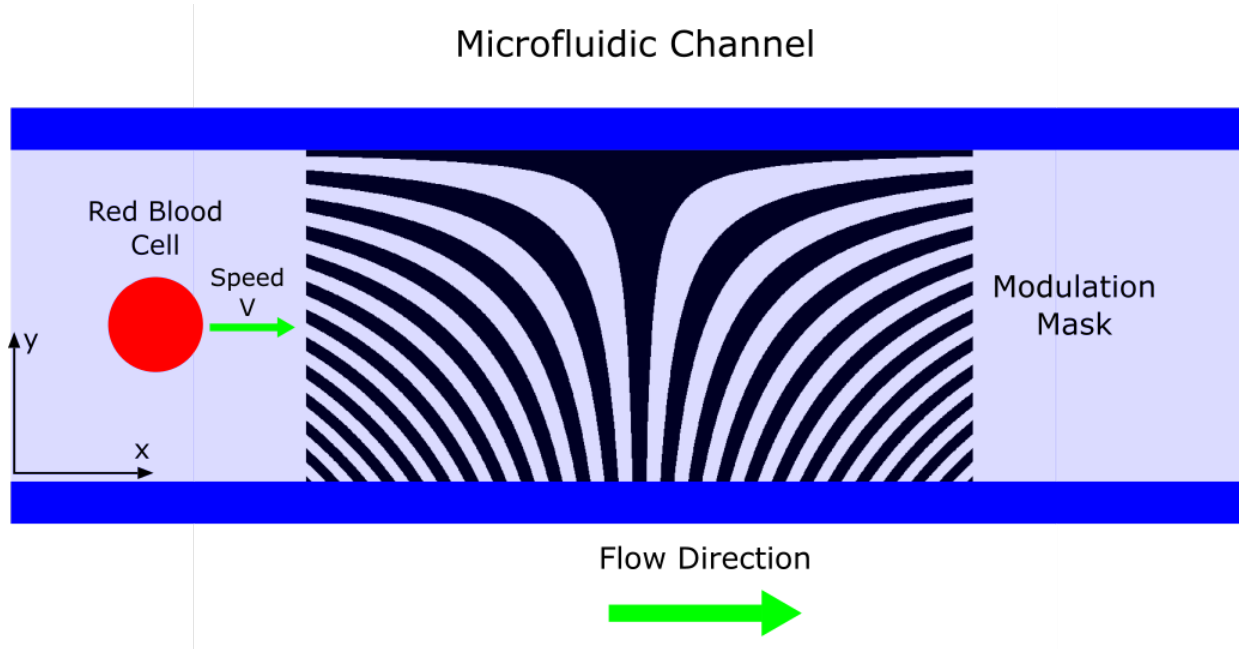


Figure 3.1: Static modulation mask placed directly above a microfluidic channel.

If one collects the light transmitted through the apparatus and measures it with a single element detector, it should be clear that the successive blocking and unblocking of fluorescence of the cell as it flows beneath the mask will result in a periodic variation of the voltage signal generated by the detector. Since the red blood cell shown in Figure 3.1 is large compared to the element size, there would be many frequency components present in the output signal. The frequency composition of the output clearly depends upon the y position of the red blood cell within the flow. This is one degree of freedom, which is a consequence of the mask itself, and the flow of red blood cells beneath the mask. However, in order for such a device to be used to recover a two dimensional image, there must be one additional degree of freedom. As such, gathering images with the system geometry, shown in Figure 3.1, will not yield the desired two dimensional measurement.

However, as stated previously, the theoretical system does possess one degree of freedom: the output signal of the detector would contain information about the y axis position and size of the target. Such information could indeed be useful. For instance, it can be related to tomographic reconstruction which produces a two dimensional image. Two dimensional image recovery from a one dimensional spinning SPIFI mask using lateral tomographic reconstruction has been demonstrated [20]. However, the system modifications required to realize tomographic reconstruction add a degree of complexity which reduces the advantages we seek by using simple systems. The question subsequently became: how much information can be recovered from a SPIFI inspired imaging system with only one degree of freedom? What would the capabilities and limitations of such systems? For what applications could these systems be used? Are the advantages compelling enough to warrant further investigation? These questions and more were motivated this thesis, and were the questions that we attempt to answer.

CHAPTER 4
MICROFLUIDIC CHANNEL FLOW POSITION AND SIZE CHARACTERIZATION
WITH STATIC MODULATION MASKS

The first realization of the initial investigation into using a static mask was that blocking of light and being hidden by the mask of the blood cell would generate a periodic signal whose frequency would be dependent on its y-position within the microfluidic channel flow. A logical starting point was to investigate the viability of using a static modulation mask to measure the flow position of an object moving in a microfluidic flow. Notably, such an integrated detection system has applications in cell sorting.

4.1 Fundamentals and a Primitive Modulation Mask

Before considering various possible modulation masks, it is necessary to consider the flow characteristics of a microfluidic channel. Many microfluidic channels operate at a length scale of approximately $100\ \mu\text{m}$ in channel width and flow velocities of order $1\ \text{cm s}^{-1}$ [21]. As such, the type of flow in microfluidic channels is nearly always laminar [21]. Laminar flow has a parabolic velocity profile, which can be modeled by

$$V(y) = 2V_{avg}\left(1 - \frac{y^2}{R^2}\right) = V_{max}\left(1 - \frac{y^2}{R^2}\right), \quad (4.1)$$

where y is position (with $y = 0$ at the center of the flow), R is $1/2$ of the width of the channel, V_{max} is the maximum flow velocity, and V_{avg} is the average flow velocity [22]. Therefore, the velocity of the red blood cell depends upon its position within the flow. This is a degree of freedom that is essentially there “for free”, potentially negating the need for a spatial frequency sweep in the mask. If we could measure the velocity of a blood cell, we could potentially identify the flow stream which it occupies. We cannot precisely measure the cell flow position by velocity alone as the flow velocity is degenerate: for any given flow speed, there is another point opposite the center of the flow with the same flow velocity. This is a

consequence of the parabolic form of the velocity profile in Equation 4.1. Ignoring for the moment this issue of degenerate measurements, it is possible for us to consider a “primitive” modulation mask without a spatial frequency sweep in any direction.

Such a primitive mask is shown in Figure 4.1. As before, the mask sits directly above the microfluidic channel, and an illumination source is placed beneath the channel, transmitting light through the transmissive regions of the mask. The spatial modulation frequency is the same for all y . No matter the flow position of a cell in the microfluidic channel, the cell would undergo the same number of transmissive region-blocking region transitions as it moved under the mask. However, the speed at which it traveled, and therefore the frequency of the periodic signal it generates, would be a function of the velocity of the cell.

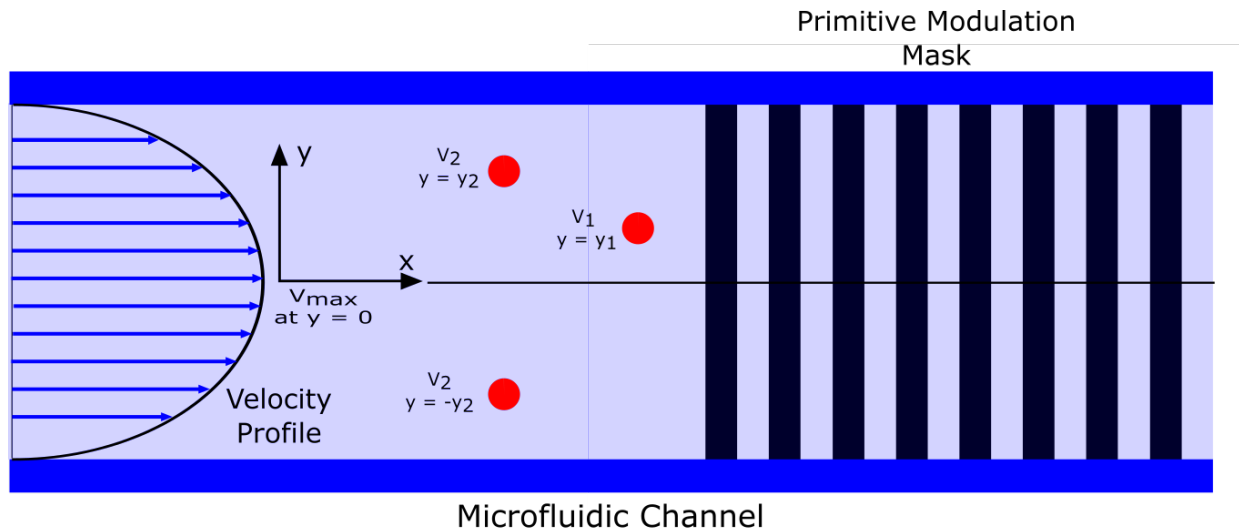


Figure 4.1: Primitive static modulation mask placed directly above a microfluidic channel.

We now take a brief moment to construct a general set of relationships between target velocity, mask spatial frequency (or period), and the dominant temporal frequency of the intensity signal generated. We start with a simple approach. First we ask ourselves how many total on/off cycles of the modulation pattern that the target will encounter as it flows beneath a mask. The answer, in cycles, is governed by the following equation

$$n = \frac{L}{P_s}, \quad (4.2)$$

where n is the number of cycles, L is the total flow length of the mask, and P_s is the spatial period of the mask (with units of length). We desire an answer to have units of inverse time (t^{-1}), so we need only divide n by the amount of time the target spends beneath the mask, which can be computed using the following equation

$$t = \frac{V_t}{L}, \quad (4.3)$$

where t is the total time spend under the mask and V_T is the target velocity. Thus, if we divide Equation 4.2 by Equation 4.3, we get an answer in units of cycles per second, or the dominant frequency component of our signal. Doing a bit of simplification, we derive

$$f_t = \frac{V_t}{P_s} = V_t f_s \quad (4.4)$$

where f_t is the frequency of the time varying intensity signal and f_s is defined to be the spatial frequency (with units of inverse length) of the mask. We now see that the frequency of the time varying intensity signal is directly proportional to the spatial frequency of the mask. While certainly not surprising, it is good to understand the relationship mathematically.

Let us now return to analysis of the system shown in Figure 4.1. Because the flow is laminar, there is a clear relationship between position and flow velocity, given by Equation 4.1. As such, by collecting the transmitted fluorescent light and measuring it with a single element detector, and then examining the frequency spectrum of the output signal, we can determine the target distance from the center of the flow with the help of Equation 4.4. Due to the velocity degeneracy, one could not determine the exact position with such a mask. One potential solution to this issue is to use one spatial frequency for the mask in the top half of the flow, and a different spatial frequency for the bottom half of the flow. The second spatial frequency needs to be carefully selected so that there was no possible overlap between periodic signal frequencies generated by each submask. In this way, the degeneracy issue could be avoided.

Let us take a moment and derive a relationship between the two spatial frequencies in each submask necessary to eliminate the degeneracy issue. Let us consider the one of the

submasks. Under the whole submask, the flow velocity will range from 0 to some V_{max} , as defined by Equation 4.1. Suppose that the spatial frequency of the top submask is f_{s1} . Using Equation 4.4, our possible temporal frequencies would range between

$$0 \leq f_t \leq V_{max}f_{s1}. \quad (4.5)$$

What about for the second submask with a spatial frequency f_{s2} ? The range would be defined by

$$0 \leq f_t \leq V_{max}f_{s2}. \quad (4.6)$$

The presence of a zero in the range given by both 4.5 and 4.6 prevents us from selecting any two frequencies without overlap, but we are not done yet. The velocity condition which yields a frequency of zero is a zero velocity. The problem condition would actually yield no data, making it not physically relevant. It does highlight that, strictly speaking, we must pick a velocity range which does not include zero. This condition translates into requiring a range of interest for flow position measurement which does not include the edges of the microfluidic channel. Such a requirement is easy to fulfill, as we really do not want the target to be stationary at the edge of the channel.

We therefore restrict ourselves to the velocity range

$$V_{min} \leq V \leq V_{max}, \quad (4.7)$$

where V_{min} is some minimum velocity corresponding to the flow speed at the edge of the range of interest. The minimum velocity (and therefore displacement from the center of the flow) must be identical for both the top and bottom submask. This velocity can, strictly speaking, be arbitrarily close to zero. However, we will see shortly why a smaller range is easier. To enforce our velocity range, we would simply make the modulation mask above the offending regions (above and below a cutoff position in the top and bottom submask, the positions of which can be found using 4.1) opaque. We will want to make the region small enough that no cells are likely to flow beneath it (or otherwise prevent cells from flowing beneath it), lest we lose flow position data.

With the minimum velocity cutoff (and therefore a top and bottom cutoff y position defined), we can go about deriving a requirement for the spatial frequencies of the two submask. For the top submask, the possible temporal frequency range is now

$$V_{min}f_{s1} \leq f_t \leq V_{max}f_{s1} \quad (4.8)$$

and the range for the bottom submask is

$$V_{min}f_{s2} \leq f_t \leq V_{max}f_{s2}. \quad (4.9)$$

Suppose we choose the bottom submask to have a higher spatial frequency. We would therefore require that the minimum possible signal frequency generated in the bottom submask to be higher than the maximum possible signal frequency produced by the top submask, giving us the following condition

$$V_{min}f_{s2} \geq V_{max}f_{s1}, \quad (4.10)$$

which we can rewrite as

$$f_{s2} \geq \frac{V_{max}}{V_{min}} f_{s1}, \quad (4.11)$$

which gives us a condition to impose on the spatial frequency on the second (either the top or bottom) submask based upon the spatial frequency of the first submask and the velocity range (again, which corresponds to a displacement range from the center of the flow). By enforcing this condition, we eliminate the degeneracy in flow stream position measurement caused by a symmetric flow profile. Note that as V_{min} approaches zero, f_{s2} increases rapidly. As such, care must be taken to select a velocity range that does not require a submask spatial frequency so high that it cannot be fabricated easily.

4.2 Mathematical Modeling of Masks

Before further consideration of masks and mask designs, it is necessary to develop a framework for predicting the detector voltage waveform for an arbitrary target and mask. It would be extremely expensive, time consuming, and inconvenient to fabricate masks in each

iteration of the design. Additionally, the modeling process can provide substantial insight into the technique making it possible to produce an optimized mask design. The process of a fluorescing red blood cell (or other target) successively moving beneath transmissive regions of the mask and blocking regions of the mask seemed to be reminiscent of the process of convolution of two functions. Based upon this similarity, we create a formalism for describing the amount of light being imaged to the detector as a function of the target position beneath the mask using the mathematical language of discrete convolution. We note that our model neglects the impact of the limited numerical aperture of the collection optics: we assume that all of the signal is collected.

Discrete convolution is well understood and computationally inexpensive, and is incredibly similar in concept to the idea of a fluorescent target moving under a modulation mask. A target can be represented as a matrix populated with 0's and 1's. 1's can be used to represent the actual body of the target, while 0's are used as noninteracting place holders in the target matrix. Similarly, the modulation mask can be modeled as a matrix of 0's and 1's. In the case of the mask, the 1's represent the transmitting regions (100 % transmission) of the mask, while the 0's represent the opaque portions (0% transmission). Each row of the target can then be convolved with the corresponding row of the mask. The value of the convolution at each entry can be taken to represent the amount of fluorescent light transmitted through the mask in that row when the cell is at the corresponding location. The convolution of all rows can then be summed element-wise. This total sum then represents the total transmitted fluorescent light that can ideally be collected at the detector as a function of the target position under the mask.

One issue with the signal produced by those convolutions is that there is still no direct relationship between the the computed signal and the time varying signal produced by the detector. In order to determine the relationship, we need only consider the design of the theoretical apparatus. The red blood cell (or other target) will flow beneath the mask at some speed V (that V will be dependent upon its position in the flow, but this is not important at

the moment). By knowing the length of the mask, it is simple to determine the time required for the cell to travel beneath the mask: $T = L/V$ where T is the total time of travel, L is the length of the mask, and V is the speed of the cell. In order to convert the computed signal to a time varying signal, we assign the first entry to time $t = 0$ and the final entry to time $t = T$. The intermediate entries are assigned time values between 0 and T with uniform time steps between them. In this manner, we compute the predicted time varying signal output by the detector for a given target at a specific flow position under an arbitrary mask. We notice that the flow velocity will impact the frequency of the signal when all else is held the same.

With the basic model established, we created a function in Octave to compute the necessary convolutions and sums to predict the output signal of the detector. Octave was selected as it is an open source software with code compatibility with MathWorks MATLAB, and for its straight forward handling of vector and matrix operations. The arguments of this function are the matrix representations of the target and modulation mask. This code, along with detailed comments, is contained in Appendix A.1.

Before using this code (and the underlying theory) to examine different modulation masks, it was appropriate to consider a couple of simple cases, reason what the result ought to be, and then compare the output of the function to our initial predictions. First, we considered a target that is a rectangle: three units long and one unit deep. Such a target can be represented in Octave as

```
Target = [1 1 1];
```

Next, we consider a mask that is one unit deep and thirty units long. The pattern on the mask is a simple series of transmissive and opaque regions, each three units long. Thus, the mask pattern elements are the same size as the target. The mask can be represented in Octave as

```
Mask = [0 0 0 1 1 1 0 0 0 1 1 1 0 0 0 1 1 1 0 0 0 1 1 1 0 0 0 1 1 1].
```

We consider such a modulation mask to have a spatial period of six units with a total of five periods on the mask.

When the target first moves below the mask, there is no effect, since the first three units of the mask are opaque, since it is the leading edge of the mask. When the target moves to the fourth unit, one unit of the fluorescent target is under the transmissive region of the mask. When the target moves to the fifth unit, two units of the target will be under the transmissive region, allowing more fluorescence to be visible. When the target moves to the sixth element, the fluorescing target will be entirely beneath a transmissive region of the mask. When it moves again, one unit of the target will be under an opaque portion of the mask, and only two units of the fluorescent target will be under a transmissive region. After the next step, only one element will be in a transmissive region. Finally, the entire target will be under an opaque region of the mask, so no fluorescent light will be transmitted. This process will be repeated until the target moves under the entire mask. Based on this thought experiment, our intuition indicated that the fluorescent light intensity measured at the detector would be modulated by a triangle wave. Using the function discussed in Appendix A.1 to compute the predicted waveform for the target passing under the mask previously defined. The waveform was then plotted in Figure 4.2, normalizing the time length of the signal to one second.

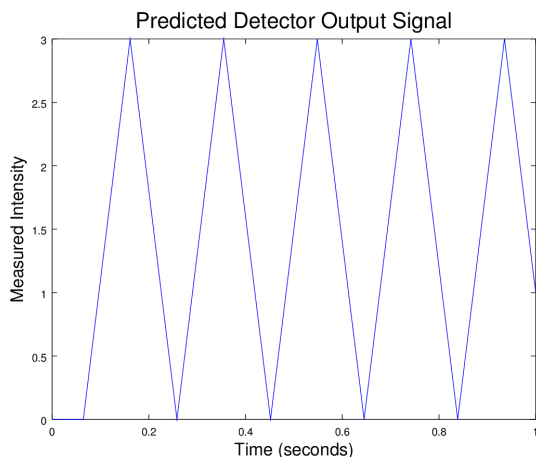


Figure 4.2: Predicted waveform for a 3 units long target with a modulation mask with a spatial period of 6 units.

The output of the detector predicted by the function is indeed a triangle wave, as we hypothesized. This result in Figure 4.2 was promising, but we required further verification of the accuracy of the model and the program used for computational predictions. We then considered another simple case, similar to the first. We consider the same target as before, but with a mask with a spatial period of ten units instead of six units, and a total of five periods. Such a mask can be modeled in Octave as

```
Mask = [0 0 0 0 0 1 1 1 1 1 0 0 0 0 0 1 1 1 1 1 0 0 0 0 0 1 1 1 1 1...].
```

Our intuition suggested that the total intensity signal would once again look similar to a triangle wave, but would have clipped peaks and troughs, due to the target being fully blocked by an opaque region of the mask for more than one unit of time, and due to the target fluorescing unobstructed for more than one unit of time. Using the function in Appendix A.1, the predicted waveform was computed, and is plotted in Figure 4.3. As before, the total length of the signal was normalized to be one second. As we expected, the functional form of the predicted detector output signal was that of a clipped triangle wave. It is worth noting that due to the signal length normalization convention that we have used, the fundamental frequency of both predicted signals is 5 cycles/second. After the results of both of these tests matched our expectations, we were comfortable attempting to use the convolution framework and program to begin analyzing masks and informing their design. Experimental verification was required before the framework could be fully trusted, but the results thus far had been reassuring.

Thus far, we have restricted ourselves to examining simple one dimensional cases of targets and masks. Given that our motivation came from measuring red blood cell positions, it is necessary to begin examining the predicted detector output waveforms for circular targets. To perform these computations, it is necessary to find a rapid way of creating a matrix representation for circular targets. To this end, we created an Octave function to create matrix representations of circular targets of arbitrary size. The code for this function

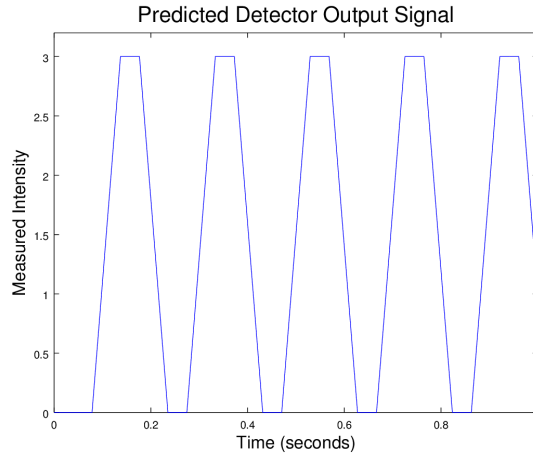


Figure 4.3: Predicted waveform for a 3 units long target with a modulation mask with a spatial period of 10 units.

is contained in Appendix A.2. Figure 4.4 shows image representations of circular target matrix approximations for various resolutions, or number of “pixels”.

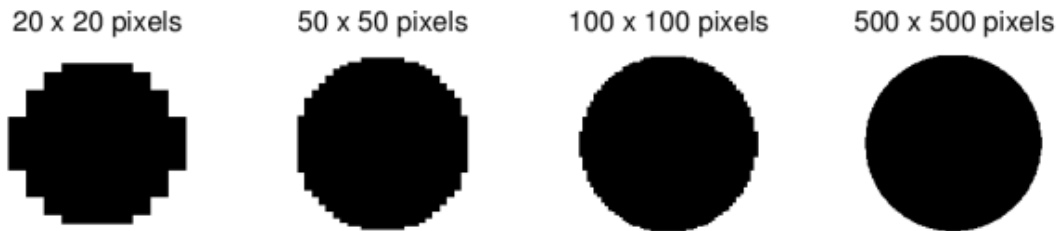


Figure 4.4: Images of Matrix Representations of Circular Targets with Various Resolutions.

As we expect, increasing the dimensionality of the matrix approximation improves the fidelity of target shape. The difference between using a 20×20 matrix to approximate a circular target versus using a 500×500 matrix is substantial, though the 100×100 matrix approximation seemed sufficient for most applications. With the ability to construct matrix representations of circular targets as well as model what the measured intensity at a single element detector would be for a given target and mask, we are ready to begin using the framework created and programs written to experiment computationally with different masks.

4.3 An In Depth Examination of the Primitive Modulation Mask

We now return to the “primitive” modulation mask discussed in Chapter 4.1: the mask with constant spatial modulation frequency, as shown in Figure 4.1. We begin by considering one of the simplest possible targets: a square target. In this case, we define the size of the square target to be one half of the spatial period of the primitive modulation mask, as shown in Figure 4.5. Note that these assumptions bear striking resemblance to the first one dimensional test case considered in the previous section.

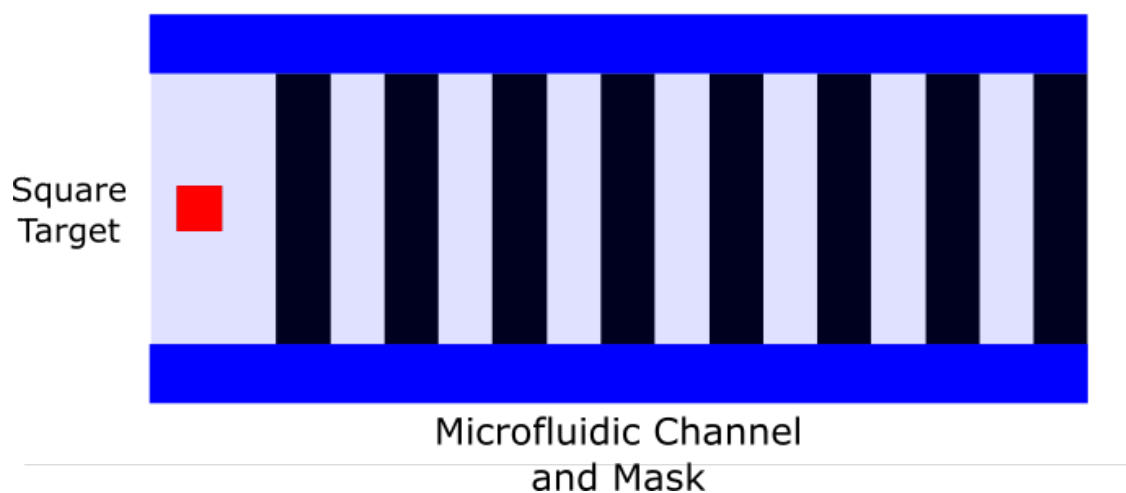


Figure 4.5: Square Target and Primitive Modulation Mask

Using the function previously created, we can compute a predicted intensity waveform for the situation described in Figure 4.5. We expect the waveform to have the functional form of a triangle wave, due to this situation’s similarity to the first test case discussed previously. Using the same time window normalization conventions established previously, the intensity versus time waveform was computed, and is plotted in Figure 4.6. As we had hoped, it is indeed a triangle wave.

The resulting predicted waveform of the detector for a square target is what we expected, but is not particularly exciting. All of this is a precursor to investigate red blood cells, which are approximately circular targets. As such, it is now appropriate to consider a circular

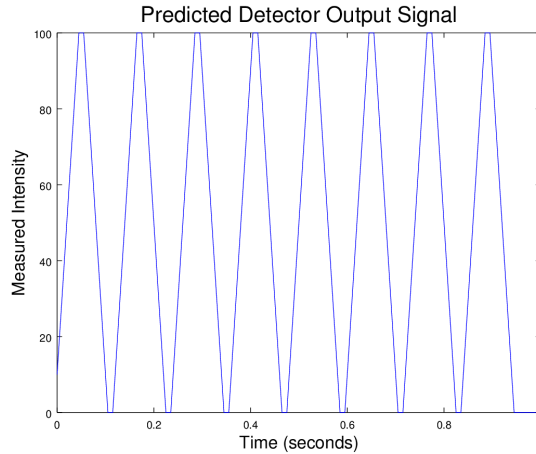


Figure 4.6: Predicted intensity waveform for a square target under a primitive mask

target, as in the case shown in Figure 4.7. The diameter of the target in question is set as one half of the spatial period of the modulation mask passing under the mask.

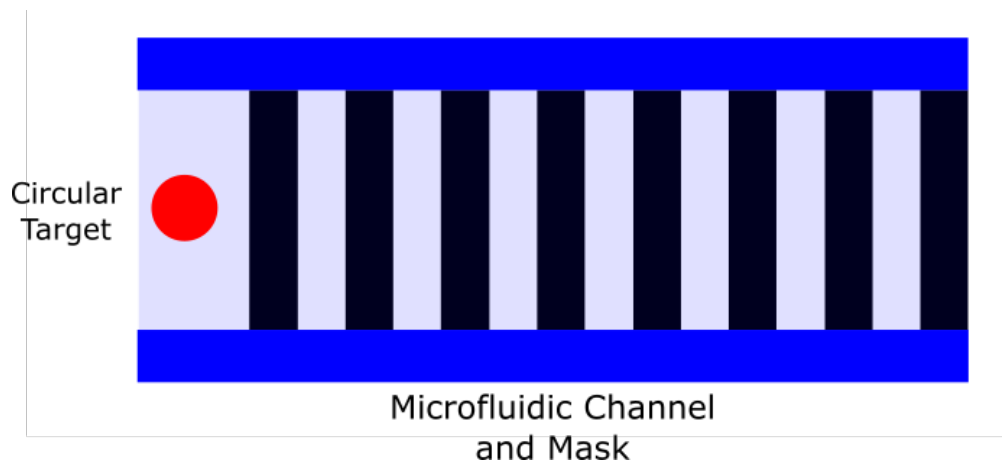


Figure 4.7: Circular target and primitive modulation mask

The question we now ask is: what form do we expect the predicted detector signal have? The non uniform profile of the circular target suggests that we would expect something more complicated than a triangle wave. Our intuition suggested that the output may look somewhat sinusoidal, but the exact characteristics were not immediately obvious in a thought experiment. As will continue to be the case, we must rely on the intensity waveform modeling through convolution framework and program to predict properties of modulation masks for

non-trivial two dimensional targets. Using the intensity modeling program, the predicted waveform was computed and is plotted in Figure 4.8

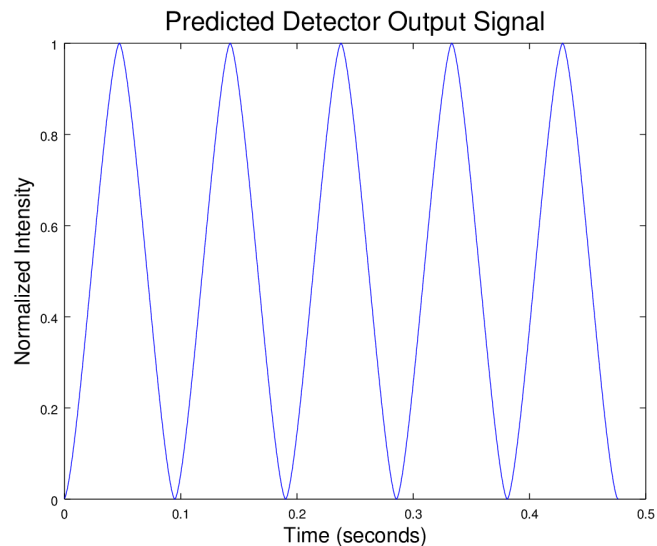


Figure 4.8: Predicted intensity waveform for a circular target under a primitive mask

Our intuition based guess turned out to be correct: the general form of the signal is indeed sinusoidal. It is worth examining the periodogram of the signal produced by a circular target passing under a primitive modulation mask. We examine the signal produced by the target passing under a total of 10 spatial periods of the primitive mask, choosing a simple rectangular window function. Note that although the signal shown in Figure 4.8 has a DC component, it is more convenient to remove it when examining its spectrum. A plot of the periodogram of the signal is shown in Figure 4.9.

Note that due to our convention of normalizing the total signal length to be one second, and given that the mask in question had a total of ten spatial periods, it is unsurprising that the peak in the periodogram be centered at 10 Hz. The location of the central peak with this primitive mask is directly dependent upon how long it takes for the target to pass under the entirety of the mask. Therefore, the frequency is dependent upon the velocity of the target. As discussed previously, since flow speed is dependent upon the location within the flow (described by the flow profile 4.1), we see once again that flow position (though the

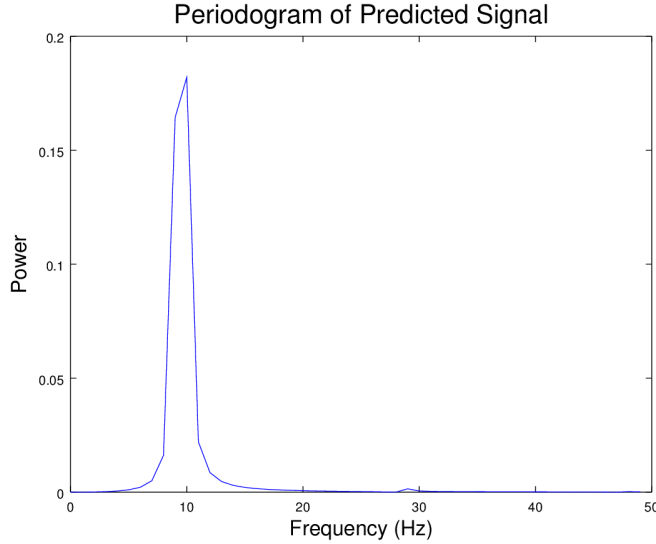


Figure 4.9: Periodogram of predicted signal for a circular target under a primitive mask

measurement result is degenerate unless using a different spatial frequency for the top and bottom halves of the flow profile) could be determined by analyzing the frequency spectrum of the signal generated by a target flowing under a primitive mask.

The shape of the peak in Figure 4.9, while roughly Gaussian, is not perfectly symmetrical. This may be the result of using a rectangular window function, which can have severe spectral leakage. Either a Hanning or a Blackman window can be used to remove any spectral leakage, as shown in Figure 4.10. Future frequency analysis in this thesis will utilize a variety of windows in order to minimize the effects of spectral leakage. As such, the choice of window will be specified for each situation.

We see now that this primitive mask could potentially be used to measure the flow position of a cell within a microfluidic channel. At this point in the development, we wondered how much more information could potentially be extracted from such a system. Would it be possible to recover any information about the target from the signal output by the detector?

To answer this question, we borrow from the theory of linear signals and systems. The output of the detector can be represented as a row vector. Conventionally (in the language of introductory signal processing), we would expect the detector output to be able to be

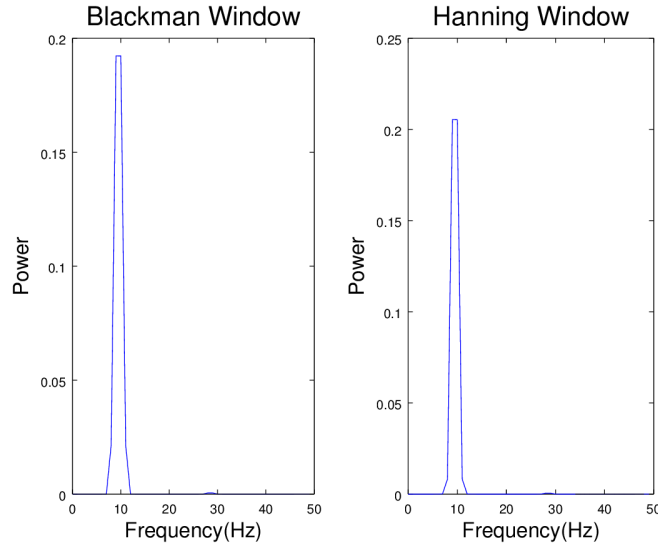


Figure 4.10: Periodogram with a Blackman and a Hanning window.

modeled as the convolution of an input (a row vector) with the impulse response of the modulation mask (another row vector). The goal then became to determine if it was possible to represent the modulation mask and the target as one dimensional vectors.

We first considered our primitive modulation mask. We need to determine the impulse response of the mask. In this case, the impulse would be a single pixel target, represented by $\mathbf{target} = [1]$. Because the target is a row vector, the predicted waveform will just be a convolution of the target and one row of the primitive mask. Basic discrete convolution theory tells us that the result of that convolution will in fact be the mask vector, since convolution of a vector with the unit impulse returns that original vector. Therefore, a row of the matrix representation of a modulation mask is in fact the impulse response for that row of the mask. Since the primitive mask does not vary in spatial frequency, any row can be used to represent its impulse response to a one dimensional target. It is worth classifying the modulation mask as a system with a Finite Impulse Response (FIR), as this fact will have consequences on how we extract information from the detector signal.

Next, we need to find a way to represent a two dimensional target as a one dimensional vector. The method here is far less straight forward, as for circular targets, there is variation

along the y axis. However, by reexamining the waveform prediction framework, we see a potential solution. Our predicted waveforms come from the sum of convolutions of rows of the target and rows of the modulation mask. In fact, for an m row target and mask, we can represent the predicted detector signal as

$$\text{signal}[n] = \text{TgtRow}_1 * h_1 + \text{TgtRow}_2 * h_2 + \dots + \text{TgtRow}_m * h_m \quad (4.12)$$

where TgtRow_i is the i'th row of the target, h_i is the impulse response of the i'th row of the modulation mask, and $*$ is the discrete convolution operator. For a primitive modulation mask, all rows have the same impulse response, h_{mask} . Because of the distributive property of convolution, Equation 4.12 can be rewritten as

$$\text{signal}[n] = \sum_{i=0}^m h_{\text{mask}} * \text{TgtRow}_i = h_{\text{mask}} * \sum_{i=0}^m \text{TgtRow}_i \quad (4.13)$$

with the variables defined as before. Equation 4.13 yields a powerful result: for a primitive modulation mask, we can collapse the information contained in a matrix representation of a target into a row vector which is defined as the sum of the rows of the matrix representation of the target. We now have a systematic way of collapsing a two dimensional representation of a target into a one dimensional row vector. For instance, a 3×3 pixel target could be collapsed into a single row vector as shown in Equation 4.14.

$$\begin{pmatrix} 1 & 1 & 1 \\ 1 & 1 & 1 \\ 1 & 1 & 1 \end{pmatrix} \Rightarrow (3 \quad 3 \quad 3) \quad (4.14)$$

A more complicated 5×5 pixel target can similarly be collapsed into a row vector, as shown in Equation 4.15.

$$\begin{pmatrix} 0 & 0 & 1 & 0 & 0 \\ 0 & 1 & 1 & 1 & 0 \\ 1 & 1 & 1 & 1 & 1 \\ 0 & 1 & 1 & 1 & 0 \\ 0 & 0 & 1 & 0 & 0 \end{pmatrix} \Rightarrow (1 \quad 3 \quad 5 \quad 3 \quad 1) \quad (4.15)$$

In order to confirm the effectiveness of this proposal, we can revisit the circular target that was discussed previously. We collapse the matrix representation of the circular target into

a row vector representation in the manner prescribed by Equation 4.13 and then convolve it with a row of the primitive modulation mask (equivalent to its impulse response). In Figure 4.11, we see the expected sinusoidal waveform, exactly as shown in Figure 4.8

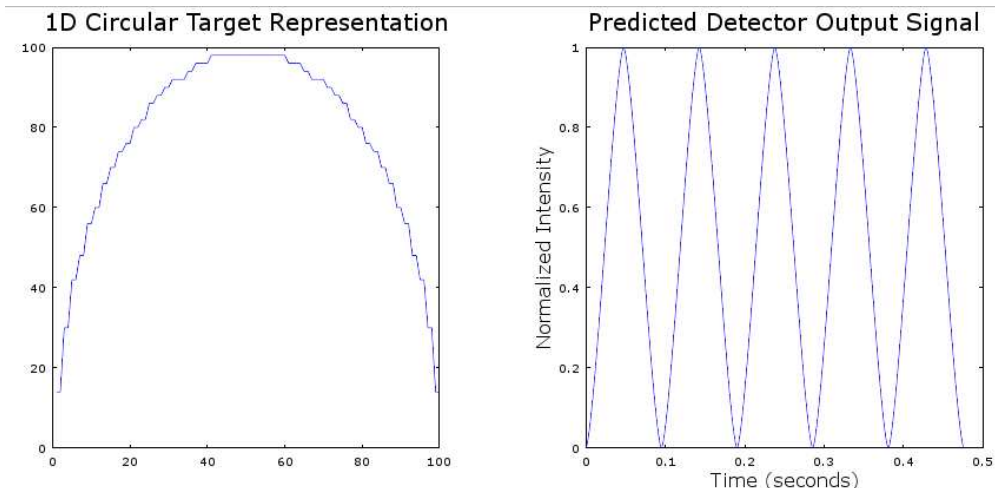


Figure 4.11: 1D Representation of a circular target, and predicted intensity signal.

It is worth noting that this approach only works because the modulation mask is uniform. Where there more than one spatial period present on the mask (as will be discussed shortly), we cannot represent the target as a single one dimensional vector, since the impulse response of the mask will vary across the y axis. However, we consider this for more than just simple curiosity: the ability to collapse two dimensional information into a one dimensional signal is an approach we will use again in another technique proposed in this thesis.

Now that we can represent the target and mask as a one dimensional linear system, we must ask how we can take time series information from the detector and retrieve information about the target. We must once again borrowing from the theory of linear signals and systems. Because we have already characterized the impulse response of the primitive modulation mask, we can take its Z-transform and determine the Z-Transform of the inverse system. Because the primitive modulation mask is a FIR system, we expect its inverse to be an Infinite Impulse Response (IIR) system. Using a filter function in MATLAB, Octave, or Python, it is possible to model even IIR systems, allowing us to recover the original 1D

representation of the target.

It is worth considering what the physical meaning of the one dimensional representation of a target is. We can consider the one dimensional representation as a sort of “area” function, where the amount of area in one pixel step on the x axis is represented by a single value. We are, in a sense, integrating over the target in the y direction as a function of x, which gives us the one dimensional representation of our target. This function will carry target shape and size information. Thus, by measuring the detector intensity, we can actually get rudimentary data about the target. Thus, from an extremely simple modulation mask, it is possible to recover flow position within a microfluidic channel and get information about the shape and size of the target flowing under the mask.

While this approach is interesting, it is not particularly practical. For flow position measurement, the y direction frequency sweep is a result of the parabolic flow profile. The derivative of the velocity flow profile shown in 4.1 is given by

$$\frac{d}{dy} V(y) = \frac{2V_{max}y}{R^2} \quad (4.16)$$

where R is 1/2 the width of the channel, V_{max} is the maximum flow velocity, and y is position (with $y = 0$ at the center of the flow.) For y values near the center of the flow, the velocity varies slowly. As such, the precision of a flow measurement profile is not necessarily uniform. Depending upon the specifics of the velocity profile, the differences in velocity over much of the channel might be small enough that differences in frequency would be difficult to measure reliably. As for the shape and size information, the key issue is the measurement noise threshold. The signal is produced by the cell fluorescing beneath the mask. If the signal is noisy, then the area function will be washed out (or at the very least made suspect) by random fluctuations in the signal.

While the practical applications of the primitive mask may be limited, it provided us a simple test case for analysis. We were able to further test the waveform modeling program (and got results that make sense), develop a way of collapsing a two dimensional target into a one dimensional signal and giving that signal physical meaning, and give a basic proof

of concept that position information within a flow could be recovered by examining the frequency spectrum of the detector signal. The primitive modulation mask is also a good representation of a situation where the target is smaller than the frequency steps in a less trivial modulation mask.

4.4 Modulation Masks for Flow Position Measurement

Now that we have examined in detail the properties and limitations of masks without any sort of frequency chirp in the y direction, it is appropriate to consider less trivial masks. We must now ask ourselves what such a flow position measurement mask should look like. Our desired goal of flow measurement will help define some of the necessary parameters. First, we naturally require there to be a frequency sweep in the y -direction, so that flow position directly affects the signal frequency. We must now decide our desired flow position resolution. For cell sorting, it is generally not necessary to have an exact position. We must now consider our desired resolution in the y direction.

While the mask shown in Figure 3.1 appears continuous, it is in fact discrete. The frequency sweep in the y direction is made up of rows of pixels in the mask with different spatial frequencies. The vertical size of these rows controls the y -position resolution of such a mask. The mask in Figure 3.1 has numerous frequencies present in the sweep, thus theoretically yielding a very high position resolution. However for mere flow position measurement, such resolution is entirely unnecessary.

4.4.1 A 3 Row Modulation Mask: Case I

We will first consider a rather simple scenario: a modulation mask with three rows modulation patterns of different spatial frequencies. Each row has a width W . For this scenario, we will consider a circular target of diameter W (same as the width of each modulation mask row element). The mask and target are shown in Figure 4.12 below. For this example, we define $W = 100$ pixels. Row 1 has a horizontal spatial period of 250 pixels (125 pixels are transparent, 125 opaque, etc.). Row 2 has a spatial period of 300 pixels, and row 3 has a

spatial period of 350 pixels.

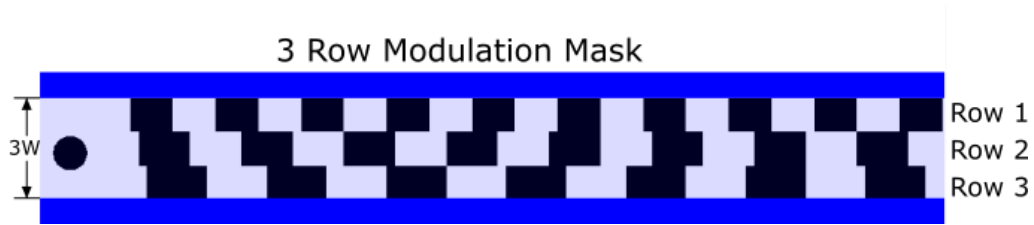


Figure 4.12: A 3 row modulation mask.

Before doing any computational analysis, it is appropriate to discuss a few features of this mask and some assumptions that we make in our examination of its properties. First, we make a simplifying assumption: that the speed of the target is independent of its position within the flow stream. While adjusting the “speed” of the target computationally only requires adjusting the sampling rate (since the convolution of the target and mask matrix has no implicit time information), it is unnecessary for this theoretical application given that we are attempting to highlight very simple properties. Additionally, such an assumption would not be unreasonable if we restricted ourselves to low velocity microfluidic flows or merely looked at targets near the center of the flow.

Next, because we are assuming that the target velocity is independent of the flow position, we can see that the rows with higher spatial periods will produce intensity signals with lower temporal frequencies (since for any arbitrary length of the mask, low spatial period rows will have more on-off cycles than rows with a higher spatial period rows). Were the velocity field not uniform in the flow (as is the case in microfluidic applications), each row of the mask would have a range of possible intensity signal frequencies produced.

Next, we see that because the width of each flow element is the same as the diameter of our target, anytime the target flows beneath only one of the rows, we see a single frequency (in terms of cycles per second, not from a Fourier perspective) of the detected intensity. In all other cases, we will see a combination of these signals, whose exact characteristics depend upon how much (and the shape of) the target is flowing beneath each row of the modulation

mask.

At this time it is worth noting that the mask under consideration is using mask row elements that have a spatial period at least twice the diameter of the target. Additionally, the duty cycle of our mask rows (fraction of transmitting amount to total period of the row) is 50%.

The last feature that we note is that each of the rows has a spatial frequency such that the target will spend some time either being under the transparent or opaque regions of the mask (as opposed to an instant). Thus we should expect a degree of “clipping” in the waveform especially when the target is under only one of the modulation mask rows. In other words, we anticipate clipping in the signal when the diameter of the target is less than one half of the spatial period of a given row.

With these features and assumptions discussed, it is now appropriate to examine the signal generated by a target flowing under this simple mask in various flow positions, as well as discuss the implications of our results. We start by examining the signals produced when the target is fully beneath each of the three rows. We expect oscillating intensity signals with clipping at the peaks and troughs due to the relative size of the target and the spatial period of the modulation mask row. Using the intensity modeling program, the predicted waveform was computed and is plotted in Figure 4.13.

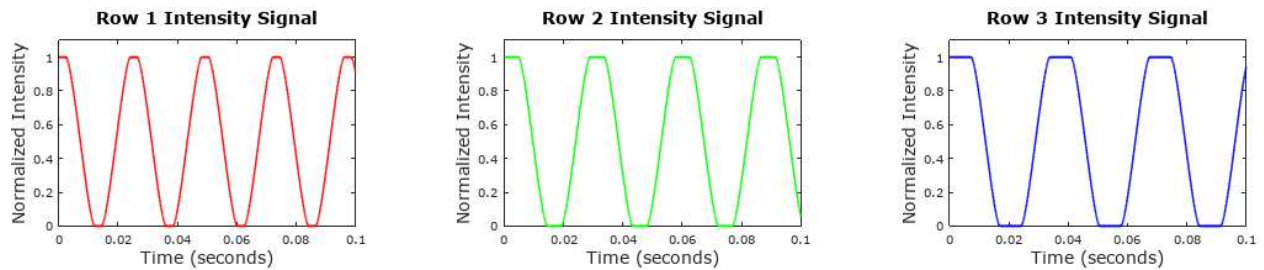


Figure 4.13: Intensity Signals From 3 Row Modulation Mask.

As we expected, we do in fact see “clipping” of the intensity signal at the peaks and troughs for the signals from row 2 and row 3, because the target diameter is less than one half of the spatial period of those rows. Additionally, we see that row 1 (with the lowest

spatial period) has the highest intensity signal frequency, and that row 3 (with the highest spatial period) has the lowest intensity signal frequency, as expected. This is trivially true only because we are assuming that the target velocity under each row is identical.

Now it is worth quickly examining the periodogram of each of the three signals shown in Figure 4.13. We construct the periodogram using a Blackman window to help deal with spectral leakage. Additionally, we set the mask to be 10500 units long for the computation of the time varying intensity signals. In this case, 10500 is the least common multiple of 250, 300, and 350. The periodograms for each of the three signals were computed, and are shown on the plot in Figure 4.14. Please note that while the plot shows all three periodograms on one plot, the signal FFT's were computed separately.

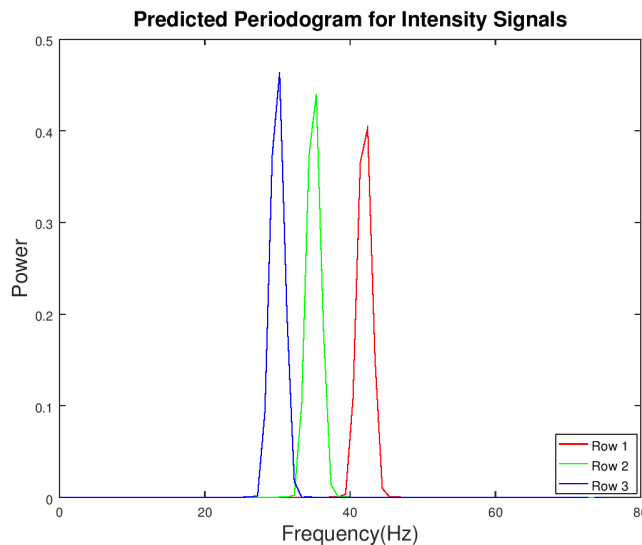


Figure 4.14: Periodogram of Intensity Signals From 3 Row Modulation Mask.

As we hoped, we do see three peaks at different locations in frequency space. As before, we define our FFT sampling time steps to be $1/N$ where N is the number of samples of the predicted intensity signal. Thus the length of the signal is normalized to 1 second. As such, our theoretical “velocity” is 10500 pixels per second. Plugging the velocity and the spatial periods into Equation 4.4 we expect frequency peaks located at 42 Hz, 35 Hz, and 30 Hz. Looking at Figure 4.14, we do indeed see frequency peaks where we expect them. We

do however see that in this case, lower spatial frequencies have more signal power than the signals from higher spatial frequencies. To verify that this is not some artifact of the DFT or FFT process, we can use Parseval’s Theorem, which states that

$$\mathcal{E} = \sum_{n=0}^{N-1} |x[n]|^2 = \frac{1}{N} \sum_{n=0}^{N-1} |X[k]|^2 \quad (4.17)$$

where \mathcal{E} is the signal energy, N is the number of samples of the signal, x is the discrete signal in question, and X is the Discrete Fourier Transform (DFT) of the signal[23, 24]. Equation 4.17 tells us that we can find the energy of a signal (or that of its DFT) by examining either the signal or its DFT. Comparing the power of each signal in the time domain did confirm that the lower spatial frequency signals do have more power than their higher spatial frequency counterparts. This sanity check indicated that this was not some sort of issue with how we computed the periodogram. After seeing inconsistent results with various other mask configurations, sampling windows, etc, we became concerned that our model was not behaving realistically: such behavior is not observed in a conventional static SPIFI system. After all, if our model cannot accurately predict general behavior trends observed in systems already well understood, it is worthless.

After much thought, analysis, and toying with target and mask parameters, we were able to determine the issue. Consider the mask we are examining in this section. Each row has the same duty cycle (50% transmitting and 50 % opaque). We also imposed a condition requiring the rows to come into phase with one another (picking a least common multiple for the length of the mask). We thought that these conditions would force a target flowing beneath each row to generate signals of equal power. What we failed to account for is how the “transition” phases effect signal power. We say that during periods of time that a target is transiting from a opaque region to a transmitting region (or vice versa), it is in a transition phase. A mask row with a higher spatial frequency (lower spatial period) will necessarily have a higher number of these transition phases as the target flows beneath its length.

If we examine the signal power of these transition phases, we will naturally find that the average power is lower than when the whole target is in a transmitting region. Rows with a greater number of transition periods will (as long as all rows come back into phase) therefore have a lower signal power due to these transition events. Now we have an explanation for the data that our model presents, but is it physical? Our searches indicated that such issues have not presented themselves in the body of work describing the current state of the art for static mask SPIFI. We must reconcile our model with real world behavior.

We find our solution by examining the length scales of our target and mask. In the case we consider, the target size is the same order of magnitude as the spatial periods of the rows in our mask. Such geometries lead to relatively long transition periods when compared to the the total time that the target is fully beneath a transmitting region as shown in Figure 4.13. While we remove the effect on signal power caused by these transition phases, we can mitigate their impact. If the size of the target is substantially smaller than the spatial periods of the modulation rows, the transition times are dramatically reduced, leading to much smaller signal power discrepancies for targets flowing beneath different rows.

Our solution is also exactly how state of the art SPIFI systems function. A laser line cursor is focused to make it as thin as possible, making the length scales conducive to minimizing the impact of the transition periods. Physical masks also have another thing going for them: granularity. Our models are both discrete and limited. Matrix representations of targets and masks are easy to create, but computing the waveforms of large (and more accurate) representations is computationally time consuming. Our frequency steps and target sizes are not as smooth as those that would normally present in a laboratory. Indeed, we would also expect to see less of an issue for rows with spatial frequencies that are close to one another (even if the phase condition was not strictly enforced) as the number of transitions would be rather similar to one another.

We therefore conclude that our model is accurate and that the conditions we considered are not terribly useful for imaging. However, the computational requirements for analyzing

targets and masks that will have more uniform signal energies across all rows are time consuming. Although the calculation time is not in itself prohibitive, we are not terribly interested in quantitative comparison of frequency peak amplitudes at this time. For the moment, we are interested in qualitative comparisons of amplitude and quantitative analysis of the location of frequency peaks. As such, we will continue our analysis with the present length scales, acknowledging that signal power can present with slightly different amplitudes for the same target when flowing beneath rows of different spatial frequency.

Once we move on to more granular masks, amplitude will become much more important. However, at that point, we will rely on the more conventional SPIFI equations that treat the masks as having a continuous frequency sweep.

4.4.2 A 3 Row Modulation Mask: Case II

With the simplest case of a target moving beneath one channel at a time considered, it is now time to examine more realistic cases: it is rather unlikely that the target would only flow beneath one mask row at a time. Realistically, the target will flow beneath two (or more depending upon the relative size of the target and the row depth) modulation mask rows.

Next, we examine the 3 row modulation mask where the target flows equally beneath two of its constituent rows: in this case, rows 1 and 2. To make the case a bit simpler, we first will have the target flow equally beneath both rows (half of the area flows beneath row 1, and the other half beneath row 2), as shown in Figure 4.15.

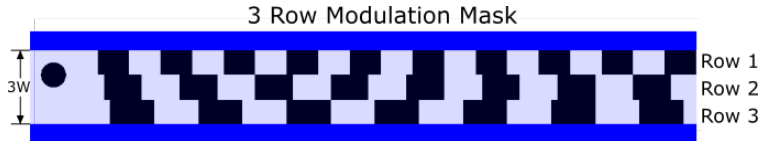


Figure 4.15: A 3 row modulation mask with with a circular target flowing beneath both row 1 and row 2.

With the target flow position decided, we utilize the intensity modeling program to examine the signal produced by the target/mask configuration in Figure 4.15. As before, we

normalize the total signal length to one second, and we normalize the signal amplitude to one. The predicted signal is plotted in Figure 4.16

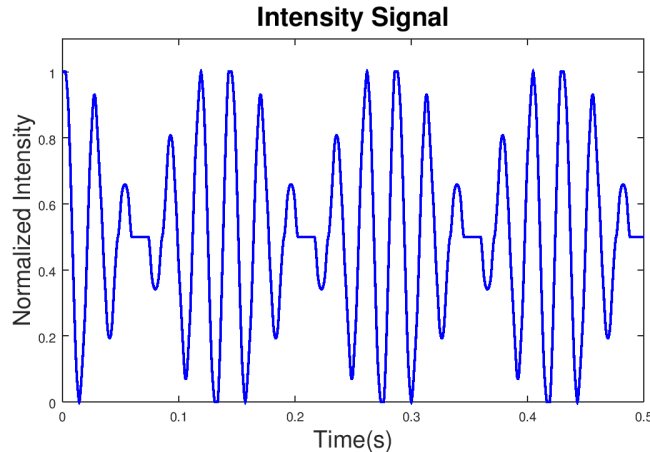


Figure 4.16: Intensity signal produced by target flowing beneath 2 rows equally

We see that this target/mask configuration produces a periodic signal with two major frequency components. This ought to make sense, at least in principle. The target is flowing beneath two rows, so the signal should have two frequencies. Thus, the resulting predicted intensity signal is encouraging. However, it is far more instructive to examine the signal periodogram. If the system behaves as we hope, there should be two peaks in the FFT located at or near 35 Hz and 42 Hz, as these are the frequencies corresponding to the rows that the target is flowing beneath. With these hopes in mind, we compute the FFT of the signal, which is plotted in Figure 4.17. We note that as before, a Blackman window was used to minimize spectral leakage.

As we both hoped and expected, we do indeed see two peaks in the periodogram centered at approximately 35 Hz and 42 Hz respectively: a rather comforting result. It is not unreasonable now to assert that had we first seen the FFT of the signal, we could conclude that the target flowed underneath row 1 and row two of the modulation mask. We see now the beginnings of a method for determining flow position by examining the FFT of the intensity

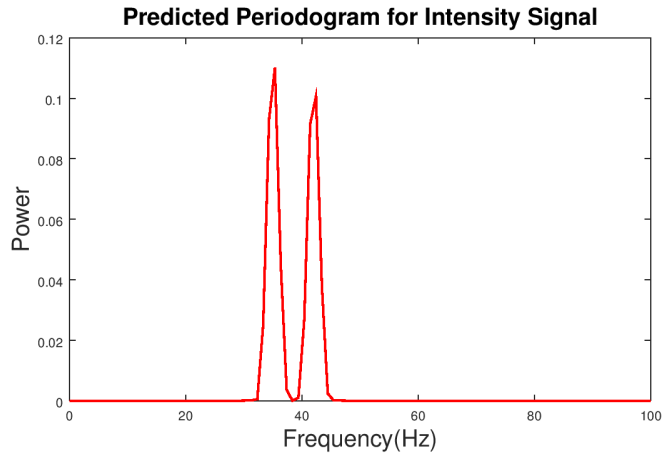


Figure 4.17: Periodogram of intensity signal produced by target flowing beneath 2 rows equally

signal produced by the target flowing beneath the modulation mask.

One thing that we notice is that the lower frequency component has slightly more power than the higher frequency component, even though an equal amount of the target flowed beneath each row. However, we recall that the same phenomenon was observed in the periodogram in Figure 4.14, even though the target was only flowing beneath one row at a time. As before, this can be attributed to amount of energy in the constituent signals. This behavior is not troublesome, but does add a degree of complexity. Suppose we had first examined the FFT without prior knowledge of the true target/mask configuration. Because there is a bit more power in the 35 Hz peak, we might falsely assume that the target was flowing with slightly more area under row 2 of the modulation mask. Because we are aware of the power distribution behavior, we can be sure to not put too much faith in the relative amplitude of the peaks in the FFT of the signal.

While Case II is nearly as contrived as the situation in Case I, it highlights that for our simple 3 row mask, altering the flow position of the target has predictable consequences to the periodogram of the signal produced. By knowing the layout of the modulation mask, we

can see how we might use the FFT to determine the flow position of a target in a microfluidic flow.

4.4.3 A 3 Row Modulation Mask: Case III

We will now examine a more complicated case, where the target is flowing unequally beneath row 2 and row 3 of the modulation mask. Specifically, the target has 65% of its diameter beneath row 2 and 35% of its diameter beneath row 3, as shown in Figure 4.18. Case III is a bit more realistic than the previous cases, as it tests a more general type of flow position.

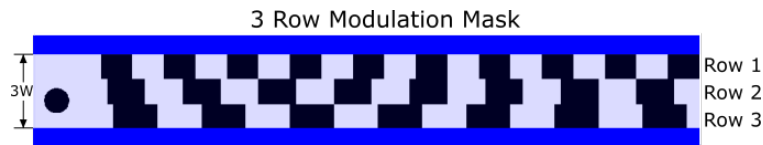


Figure 4.18: A 3 row modulation mask with with a circular target flowing beneath both row 2 and row 3.

Before using the intensity signal modeling program, we would do well to make an effort to make some qualitative predictions about its features in the time and frequency domain. First, we observe that the target is moving beneath more than one row. As such, we can reasonably expect a signal with two different core frequency components. In the time domain, we should observe a signal with a higher and a lower characteristic frequency. Given that the target is moving beneath row 2 and row 3 of the modulation mask, we expect to see peaks in the periodogram around 35 Hz and 30 Hz. Additionally, given that there is substantially more target area flowing beneath row 2, we expect there to be more signal power concentrated in the 35 Hz peak (the row signal-power phenomenon noted in Case II is fairly small). With these expectations in mind, we use the intensity modeling program to compute the predicted time varying signal, which is plotted in Figure 4.19.

As we had hoped, we see a signal with two characteristic frequencies. Its form is quite similar to the signal examined in Case II, which is another comforting sanity check. However,

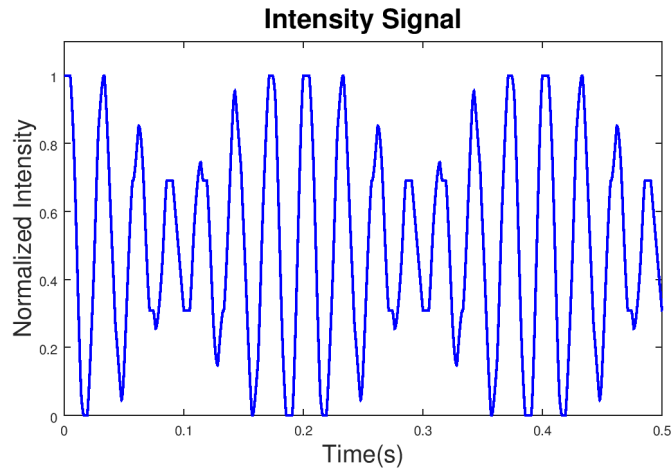


Figure 4.19: Intensity signal produced by target flowing beneath rows 2 and 3

the important features are best examined by considering the periodogram of the signal, which is plotted in Figure 4.20. As before, we used a Blackman window to minimize spectral leakage.

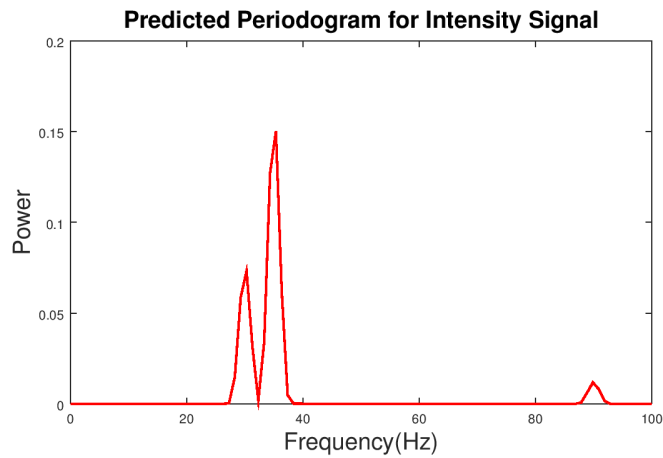


Figure 4.20: Periodogram of intensity signal produced by target flowing beneath 2 rows unequally

We do indeed see two peaks in the frequency domain at 30 and 35 Hz, as we had hoped. Additionally the peak centered at 35 Hz does have more power than the 30 Hz peak, confirming our educated guess. We also see a harmonic of the row 3 signal at 90 Hz. These harmonics are not a problem unless they overlap with frequencies that correspond to rows on a modulation mask. With the current 3 row modulation mask configuration, they pose no threat. But masks with more rows may need to consider the locations of these harmonics.

Case III illustrates once again that altering the flow position of the target as predictable consequences in the frequency domain of the signal produced. Additionally, we see that if we had only the periodogram, we could make some general statements about the flow position of the target. The frequencies present tell us that the target is flowing beneath rows 2 and 3 of this particular mask. The fact that there is more power in the frequency domain peak corresponding to row 2 tells us that the target is flowing more beneath the 2nd row of the mask. As it stands right now, the previous statement is qualitative, not quantitative. While these conclusions may seem obvious (given that they match the initial conditions that we defined), it does demonstrate that we can get information from the periodogram of the signal.

4.4.4 The 3 Row Modulation Mask: A Review

The three cases that we considered provide a good qualitative demonstration of the potential in the simplistic 3 channel mask. Based on the results of the cases that we examined, we can start to make a compelling case for the use of static modulation masks for fluid flow measurement of targets flowing in a microfluidic channel. By mapping physical flow positions to frequencies of intensity signals produced by the target/modulation mask interactions, we can get fluid flow information directly from the FFT of the intensity signal. However, the three row modulation mask does have some limitations, specifically in its resolution of flow position.

The limited resolution of the mask is a direct consequence of the relative depth of the rows compared to the size of the target. In our test cases, we set the target size to be equal

to the row depth. In the best case scenario, the target is flowing underneath one (and only one) row, producing a single peak (and its associated harmonics) in the periodogram. What if the target was smaller than depth of the row? We would see less power in the frequency peak of the periodogram (since the amplitude of the intensity signal will be smaller), but we would have no way of knowing where the target is flowing within that row. Therefore, in the best case scenario, our resolution is limited to the row depth of the mask.

More generally, we have scenarios where the target is flowing beneath more than one row, as we discussed in Case II and Case III. For a target that with a width that is less than $2W$, we see two peaks in the signal periodogram, telling us which two rows the target is flowing beneath. This gives a bound for where the target is flowing with a width that is equal to two times the standard row depth. While this is helpful, given that the depth is still on the same order of size as the target, we have considerable uncertainty in flow position.

By examining the relative power in each frequency peak in the periodogram, it appears that we can get a qualitative sense of whether the target is flowing more under one row than the other. But what about quantitatively examining the amount of power in each frequency peak? It is possible that one could precisely determine the size of the target (since larger targets will have a higher signal power) as well as determine what percentage of the total target area is flowing beneath a given row. In fact, it should (in principle) be possible to determine the area of the target based upon the the total power of the signal.

4.4.5 A 5 Row Modulation Mask: Case I

We will now consider a modulation mask with 5 rows in order to achieve greater flow position measurement resolution. Each row has width W . For this scenario, we will consider a circular target of diameter $d = 5W/3$. Because we have more possible frequencies and they are closer together, we choose to increase the sampling window to 50000 samples to help avoid spectral leakage. This is accomplished (from a computational perspective) by making the matrix representation of the modulation mask have 50000 columns. As before, we choose to define the sampling rate such that the total signal length is one second. For the purposes

of our computations, we set $W = 60$ pixels (consequently, $d = 100$ pixels). In Table 4.1, we list the row number and corresponding spatial period and temporal frequency computed using Equation 4.4.

Table 4.1: 5 channel modulation mask row spatial periods and temporal frequencies.

Row #	Spatial Period (px)	Temporal Frequency (Hz)
Row 1	200	250.0
Row 2	225	222.2
Row 3	250	200.0
Row 4	275	181.8
Row 5	300	166.7

We will first consider a case where the target flows down the center of the modulation mask. Due to the target symmetry and size, it will flow with most of its area beneath row 3, with smaller (but equal) amounts of area flowing beneath rows 2 and 4, as shown in Figure 4.21.

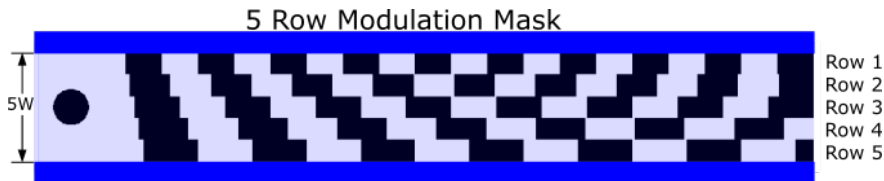


Figure 4.21: A 5 channel modulation mask with the target flowing in the center

Next, we compute the intensity signal using the modeling program. A plot of the signal is shown below in Figure 4.22. Given the fact that it has three different major frequency components, the relative complexity of the signal compared to those shown in previous sections is not surprising. As the signals get more complex, it becomes less didactic to examine plots of the time series. Periodicities are less clear, temporal beats are messy, and no real qualitative information can be gained any longer by examining the time domain plots. For these reasons, future cases examined will no longer have intensity signal plots included. After all, the interesting information, carried in the power distribution of its constituent

frequency components, is best examined in the frequency domain.

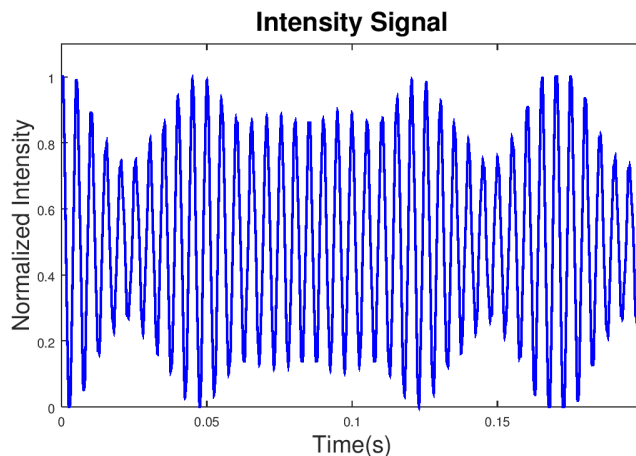


Figure 4.22: Intensity signal produced by target flowing beneath rows 2, 3, and 4.

We now move on into the frequency domain analysis of the signal. Given that the target is flowing beneath three different rows of the mask, we expect there to be three power peaks in the periodogram. Based on the flow position of the target (flowing beneath rows 2, 3, and 4) and the frequency information contained in Table 4.1, we also expect to see these peaks at 222.2 Hz, 200.0 Hz, and 181.8 Hz, respectively. Additionally, it also seems likely that given how much more area is flowing underneath row 3 of the mask versus rows 2 and 4, there will be more power at the peak at 200 Hz in the FFT. Even though qualitative analysis of power in the frequency domain has its limitations, such large differences should be noticeable. With some educated guesses made, the stage is set, and a plot of the periodogram of the signal is shown below in Figure 4.23.

As we expect, we do see power peaks in the periodogram where we expect them. Moreover, the frequency corresponding to row 3 does indeed have substantially more power than its sister peaks. We will not use this qualitatively, but it does provide a useful indicator that the target area flows predominantly under row 3. Additionally, the power distribution is roughly symmetrical.

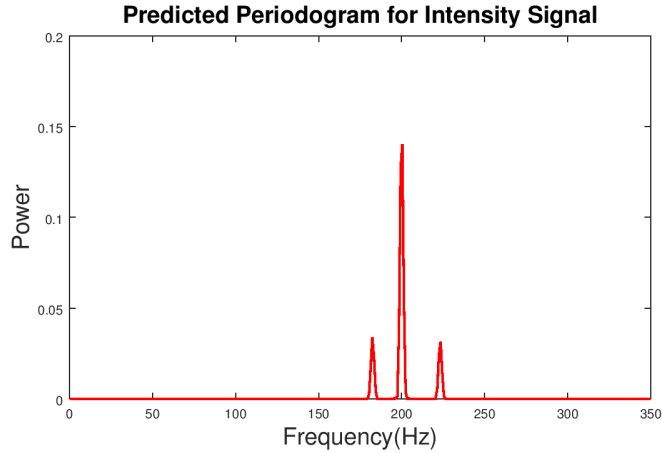


Figure 4.23: Periodogram of intensity signal produced by target flowing beneath rows 2, 3, and 4.

As before, we can see that were we equipped with only our intrepid model and the periodogram shown in Figure 4.23, we could make some general statements about the flow position of the target. For the case examined here, we have a bounded range where the target is (somewhere beneath rows 2, 3, and 4). Additionally, we could fairly comfortably say that the majority of the area of the target flows beneath row 3. Since we assume our targets are circular, it follows that the centroid of the target is flowing beneath row 3. Much like Case II of the 3 row modulation mask, having a target flow position be centered in the manner described is not a very general case, making it necessary to examine a more likely class of situations.

4.4.6 A 5 Row Modulation Mask: Case II

We now consider a situation where the target flows beneath three rows of the modulation mask (in this case, rows 3, 4, and 5), but whose flow position is not centered on any mask row. This case is analogous to Case III of the 3 row modulation mask analysis. For the case that we consider here, we have 30% of the circular target's diameter flowing beneath row 3, 60% beneath row 4, and a mere 10% of its diameter flowing beneath row 5. The situation is

shown in Figure 4.24.

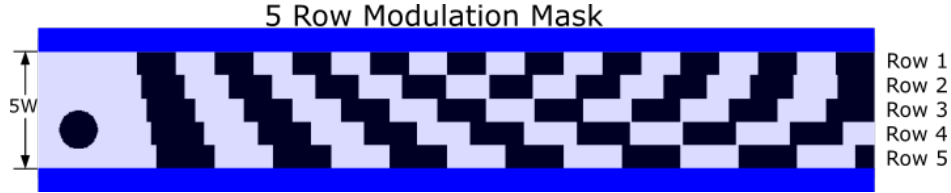


Figure 4.24: A 5 channel modulation mask with the target flowing off center beneath rows 3, 4, and 5

Next, we compute the predicted intensity signal and its FFT. Before plotting the periodogram, it is instructive to discuss what we expect. Given that it is flowing beneath rows 3, 4, and 5, we expect (by examining Table 4.1) peaks in the periodogram at 200 Hz, 181.8 Hz, and 166.7 Hz respectively. Given that most of the area of the target flows beneath row 4, we anticipate that the peak with the most power will be located at 181.8 Hz. We also expect that the peak at 200.0 Hz will be higher than the peak at 166.7 Hz, as more area is flowing beneath row 3 than row 5. With some educated guesses made, we now examine the periodogram, shown in Figure 4.25.

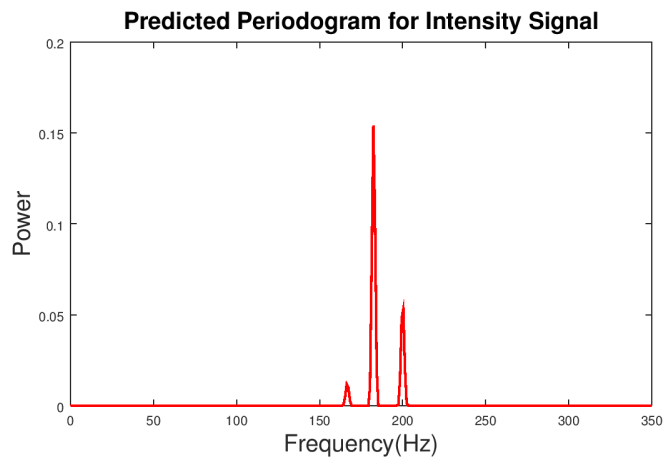


Figure 4.25: Periodogram of intensity signal produced by target flowing beneath rows 3, 4, and 5.

As we expected, there are three peaks in the periodogram at locations that we expect. Moreover, their relative magnitudes match up with our arguments based upon relative area of the target flowing beneath each row. Were we just looking at the FFT without any other information, we could determine a bounded range where the target must be within the flow, state that the centroid of the target flows beneath row 4, and that the target centroid is closer to row 3 than row 5.

4.4.7 The 5 Row Modulation Mask: A Review and Closer Examination

With a couple of cases considered for the 5 row modulation mask, it is prudent to take a moment to see what was gained by adding additional rows. The three row modulation mask had (barring the extremely unlikely scenario of the target flowing under only one row) a best case flow position bound of $2d = 200$ pixels, meaning that generally we can say that a target is flowing somewhere between the two rows indicated in the periodogram. Relative power in the peaks, provided the differences were large enough, could give a rough indicator of which row the target was flowing under more. However with only two rows activated at any one time, information was limited.

With the 5 row modulation mask, at worst we have a flow position bound of $9d/5 = 180$ pixels: a 10% reduction. Even better, our best case scenario, when the target flows beneath only two rows, gives us a flow position upper bound of $6d/5 = 120$ pixels: a substantial improvement from the 3 row modulation mask. Increasing the number of rows is not without its trade-offs: in order to prevent spectral leakage, we had to increase the length of the temporal window by increasing the length of the modulation mask in our simulation. We will discuss the Fourier-induced trade-off in more detail later. However, we do see that increasing the number of rows does indeed allow us to decrease the size of the region where we can say the target flows, giving us increased flow resolution.

Increasing flow position resolution also has an interesting side effect. As we reduce the depth of the rows and add more frequencies, we are able to place an upper bound on the number of rows beneath which the target flows. Knowing the location of these rows gives

us the flow position. But by knowing the number of rows being activated (and the depth of the rows in the modulation mask), we can actually place a lower and upper bound on the *size* of the target. To illustrate this, we can consider the 5 row modulation mask once more. Examining the periodogram in Figure 4.25, we already concluded (based upon the frequencies observed) a range for the flow position of the target. But we can actually say more. The target is activating three mask rows. Clearly, the diameter of the target must be greater than the depth of a single row. This gives us a lower bound for the size of the target: $d > W$. We also know that the target is activating only three rows, meaning that, at most, the size of the target has an upper bound of $d \leq 3W$. Therefore, using a 5 row mask with the size parameters of the target and mask previously used, we can safely say that the size of the target is bounded by

$$W < d \leq 3W, \tag{4.18}$$

where w and d are the mask depth and target diameter respectively. While the resolution leaves something to be desired, we can see that flow position measurement and size measurement are different ways of looking at the exact same problem. When we know where a target is within the flow, and where the target is not, we achieve flow location and size characterization simultaneously. It is worth noting that when we talk about size measurement, we really mean the target extent perpendicular to target flow. For circular targets, that size is exactly the same as the diameter. For less trivial targets, we will have to be more careful in our language. But for the moment, we still restrict ourselves to plain vanilla circular targets.

The size range given by Equation 4.18 is not all that great. We previously defined $W = 60$ pixels and $d = 100$ pixels. Therefore, our diameter measurement of a 100 pixel target is bounded by the range $60 < d \leq 120$ pixels. Our diameter measurement resolution is rather low, but it is achieved with a simple 5 row modulation mask. By adding more rows and reducing their depth, we can achieve increasingly good resolution for both flow position and size measurement. Again, adding more rows has its tradeoffs, which will be discussed

at the end of this chapter.

4.5 Laser Micromachined Masks: A brief aside

Now that we have used our theoretical and computational framework to model masks, it is appropriate to consider how we will actually test them in the lab. As we have discussed previously, SLM's can be used to create 2D static masks. The SLM's key advantage lies in its flexibility. SLM's are computer controlled, and are capable of generating a wide variety of different mask configurations without swapping out anything: it's all electronic. That flexibility is fantastic for prototyping masks, provided that the SLM can achieve the necessary resolution to generate the desired row elements. However, such flexibility comes at a steep fiscal price. SLM's are highly specialized pieces of equipment and can easily cost many thousands of dollars. While a research laboratory can often afford one, the goal of this thesis is to lower the cost of cell cytometry, and requiring an SLM to create the mask is not ideal.

We find our salvation in a technique called femtosecond-laser micromachining. Nathan Worts, a PhD candidate at Colorado School of Mines, developed such a system, and has provided substantial support to the research done in this thesis. Femtosecond-laser micromachining uses 200 fs laser pulses to machine or ablate targets with remarkable precision and speed. This technique can be used to create a variety of useful devices, including microfluidic channels and lab-on-a-chip systems. Specifically, we hope to use Worts' system to machine modulation mask patterns onto inexpensive glass substrates. With this technique, we are capable of a few key advantages.

The first advantage is expense. While the femtosecond-laser micromachining system is expensive, only one is required to produce many masks. The glass substrate can be rather inexpensive. Indeed, we used glass microscope slides for testing, which will be addressed in the next section. The low cost of masks is useful for research purposes, but will also drive down costs of user-ready systems as well. The second advantage is flexibility in configuration. SLM's can change their pattern, but have sharp resolution limits, and can only be used for static modulation masks. Femtosecond-laser micromachining can be used to generate masks

of virtually any shape or size, including the circular spinning modulation mask. Finally, Worts' system is fast: small masks can be completed in a matter of minutes. Large masks may take several hours, but are more than capable of allowing for rapid prototyping, iterative design, and testing. While it is useful to do as much of the design computationally or theoretically as possible, hard data collected in the laboratory must eventually be used to confirm the veracity of any claims we make.

Due to the many advantages afforded by utilizing femtosecond-laser micromachining, we opt to use it for the manufacturing of experimental modulation masks. At the time of testing, the effectiveness of masks created this way was unknown. One question was whether or not the etchings would provide enough modulation depth to the laser beam (i.e. would the opaque regions actually attenuate the incident light). Another question was over what range of frequencies of light would the masks be effective. While in depth characterization of these masks is outside the scope of this research, it did provide a good opportunity to test the viability of laser micromachined masks for applications for our research and for use in SPIFI.

4.6 Experimental Verification of Proof of Concept

We have now spent a good deal of time creating a framework for predicting the signals produced by targets flowing beneath a modulation mask. We have achieved a great deal: our model qualitatively matches our intuitive expectations. However, before money and time are invested in constructing our proposed system, it is necessary to test its viability in more rudimentary ways. Should the results match our model, more complicated tests can then be suggested.

4.6.1 Simple Testing: Advantages and Reasoning

A fair question to ask would be the reasons behind our decision to start with tests that we ourselves describe as “rudimentary”. Such an approach has three major advantages. First, just as we developed our model and theory from fundamental (and hopefully simple)

principles, it is beneficial to allow our experimental set-ups to progress similarly. Such an approach allows us to test our most fundamental assumptions and build off of them. It also prevents us from wasting resources should our model rely on fallacious arguments. The second reason for the iterative approach is that it allows us to progressively add degrees of complexity to our lab apparatus. When assembling complicated systems, wise scientists and engineers take time to test and verify that each phase, subsystem, and component of the system works as expected before continuing to the next step. Testing the rudimentary principles on which our model is based allows for the use of fairly rudimentary systems, which can then be incrementally made more complicated and robust. The third and final reason is a matter of limited time. Time constraints imposed on this research require that we attempt to demonstrate that our ideas are sound, as opposed to delivering a working system, with its capabilities and limitations outlined.

Our goal is to present solutions, demonstrate their viability, and make a case for the investment of financial resources and talented researchers into further investigation of our solutions. Demonstrating that our model is sound, even in a more rudimentary situation, provides a stronger footing for asking for research grants than the model alone. For these reasons, most of our experiments contained in this thesis and performed in the lab will be fairly simple. However, we do believe that the data presented in this thesis will provide solid ground for further research.

4.6.2 Rudimentary Testing with a Light Based Target

In order to test the viability of using static modulation masks for flow position measurement of a target in a microfluidic channel, we will relax the requirements and make them as simple as possible while still being similar to the original question. First we choose to, for the moment, focus on targets who are macroscopic as opposed to microscopic. This relaxes the sensitivity and noise threshold requirements for our system right off the bat. It also allows us to use something other than a microfluidic channel to move the target, eliminating things like pumps, machining a channel, etc.

The key concept that we test here is whether or not a 2D static modulation mask can be used to differentiate between targets flowing at different positions. Our model has been focused on fluorescing targets (though it works for opaque targets blocking light as well), but what if instead of a physical target, we used a laser beam? By sweeping a laser beam of appropriate scale across a modulation mask, we are in effect, simulating a fluorescent target with a far simpler apparatus. While the laser beam is far brighter than what could reasonably be produced by fluorescent tagging agents, the principle of examining a target emitting light is preserved. Using a scan mirror, we can sweep the laser beam across the modulation mask at a controlled and constant speed, as well as have a relatively continuous sweep (as opposed to recording data for one sweep across the mask at a time).

With some basic requirements created, and with the aid of Dr. Jeff Squier, (the thesis advisor), a simple system for testing flow position was created. The apparatus served an additional purpose: testing the viability of using the laser micromachined masks created by Nathan Worts for use in SPIFI systems. A system schematic is shown in Figure 4.26. To make things simple, our initial test used a diode laser in the visible spectrum ($\lambda = 635 \text{ nm}$). Using visible light made construction for a novice system builder easier, as well as allowed us to test the laser micromachined mask in the visible spectrum. Two mirrors, each adjustable on two axes, provided the requisite degrees of freedom for optical alignment through the two irises. In order to focus the light to a small point using the scan lens, we needed to fill the lens as much as possible. Therefore, a beam expander was included. In order to sweep the beam across the mask, a scan mirror was installed. The scan mirror is controlled by a function generator. Specifically, we used a triangle wave with a frequency of 5-10 Hz. A triangle wave is used in order to drive the mirror at a constant velocity. As the mirror scans, it causes the laser beam to travel at an angle deviated from the aligned beam. To correct the angle change, a scan lens was installed one focal length from the scan mirror. A scan lens collects light coming in at different angles and forces them to be parallel to the aligned system. Functionally, this means that the beam will be sweeping across an axis parallel to

the aligned beam, as opposed to an angular sweep.

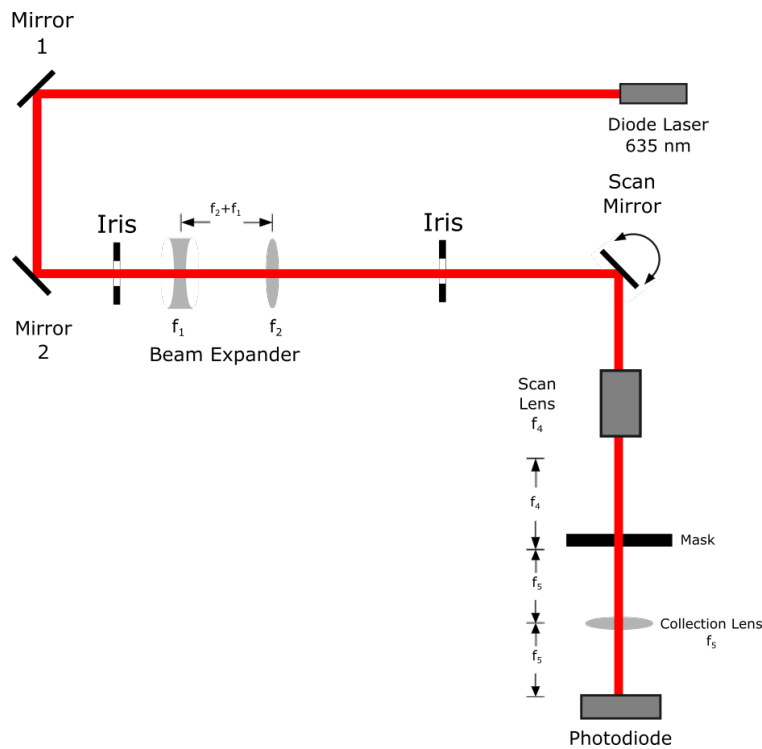


Figure 4.26: System Schematic to determine flow position measurement viability using a static modulation mask.

Next, the mask is placed one focal length away from the scan lens. The mask used in this experiment was a glass microscope slide with a cartesian coordinate based mask pattern etched onto its surface. A portion of the slide is shown in Figure 4.27. Each mask is approximately 1 cm across. We note that the black portion is the translucent slide (against a black background) and that the white structure is the micromachined part of the slide. These regions scatter light strongly, acting opaque.

The astute reader will note that the modulation masks in Figure 4.27 are far more similar to the mask shown in Figure 2.5 than the three or five channel modulation masks that we have considered. Be not alarmed, fearless reader: the three and give row modulation masks are simply the conventional mask with discretized (instead of continuous) frequencies. In fact, though seemingly continuous, the mask in Figure 4.27 is in fact discrete. The element depth is just too small to see. Were we to consider a mask with a large number of rows,

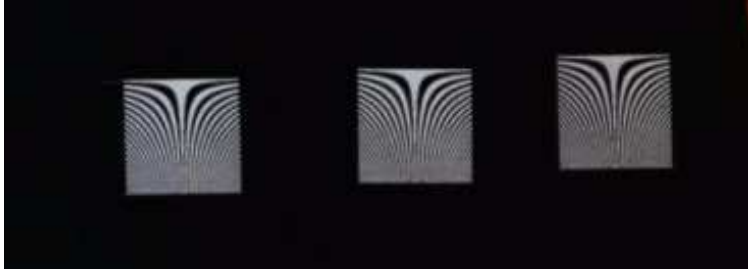


Figure 4.27: 2D Cartesian Masks Laser Micromachined onto a glass microscope slide. Image courtesy of Nathan Worts.

it would look like a “blocky” version of the mask shown in Figure 2.5. This is not to say that using the the masks on the slide will yield the exact results we predict for more discrete masks. The beam width of the laser is much larger than the individual element depths, so it will activate numerous rows. Therefore, we expect the FFT to have a wider bandwidth. Additionally, given the large number of rows and the small depth of each row when compared to the size of the overall mask, we expect the potential for high flow position (and therefore size) resolution. We also expect the periodogram to have one smooth peak with large bandwidth, instead of numerous small peaks with narrow bandwidth (as was the case with the size scales considered with the 3 and 5 row modulation mask)

Finally, we use a collection lens in order to gather the light transmitted through the mask and focus it onto a photodiode. The voltage signal produced by the photodiode is then sent to an oscilloscope for plotting and data recording. Once the system was built, it was time to begin testing.

The modulation mask was set such that the laser beam scanned horizontally across the modulation mask on the far right of Figure 4.27. We note that the top of the modulation pattern has a lower spatial frequency than the bottom of the mask. Examining Equation 4.4, we recall that the frequency of our time varying intensity signal is directly proportional to the spatial frequency (of a given row being “used”) of the mask. Based on that equation, as well as experience gained in the 3 and 5 row modulation mask case studies, tells us that we should expect the frequency of the intensity signal to increase as we sweep across lower

regions of the mask.

We began by scanning across the lower spatial frequency region of the mask using the diode laser. Using an oscilloscope, we collected a trace of the voltage signal produced by the photodiode, which is shown in Figure 4.28.

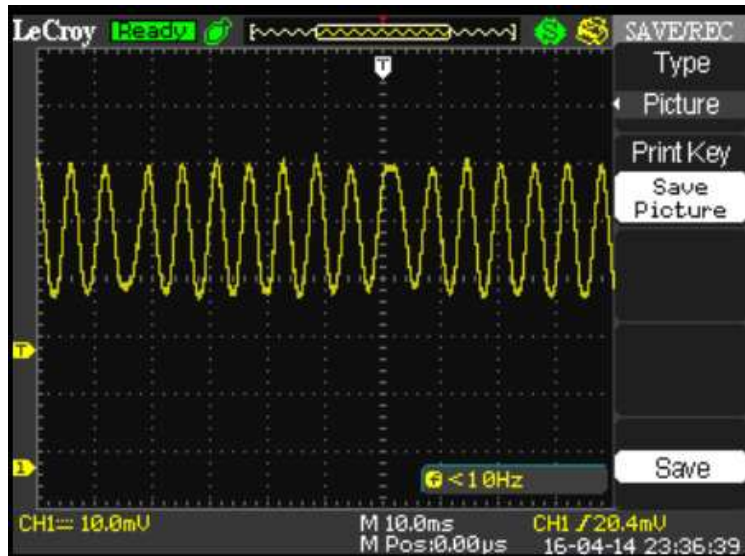


Figure 4.28: Trace of low spatial frequency sweep with a red diode laser

As we hoped, we see that the voltage signal is roughly sinusoidal. The result in Figure 4.28 is incredibly important for two reasons. First, it supports (in a small way) our previous work modeling the interactions of a circular target with a mask. Second, it demonstrates that a femtosecond laser micromachined glass mask can modulate a red diode laser. Even though most SPIFI takes place using light in the near IR band, it is promising. Moreover, it means that we can create masks using Nathan Worts' system inexpensively for the purposes of this thesis, saving time and money.

In addition to recording the plot, we also recorded a csv file containing time and voltage series values for further analysis. The periodogram (with a Blackman window for spectral tapering and with the DC component removed) of the signal was computed and is plotted in Figure 4.29.

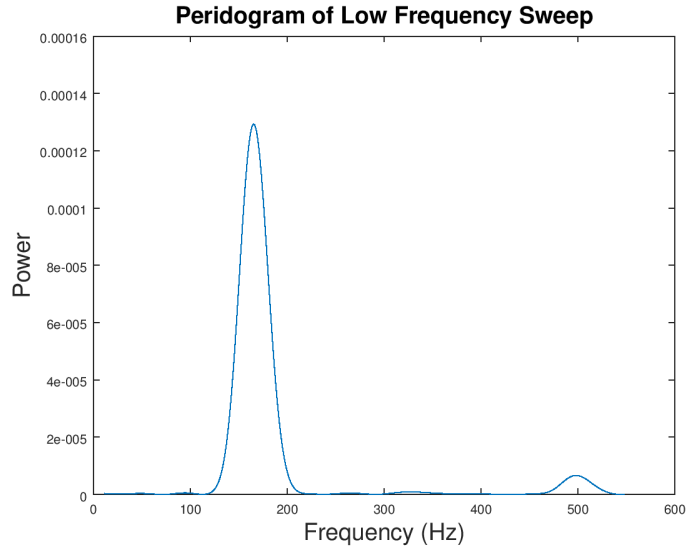


Figure 4.29: Periodogram of Low Frequency Signal

In Figure 4.29, we see that the primary peak is centered about 165 Hz, with a harmonic near 495 Hz. We notice that the shapes are ever so roughly Gaussian. Given that the laser beam (acting as the target) is also roughly Gaussian in nature. This makes some sense, as the intensity of the laser along the direction parallel to the frequency sweep is also roughly Gaussian. Were this a more conventional SPIFI, the shape of the periodogram would actually correspond to a line element (being scanned by a line cursor) of the target. But since we sacrifice a degree of freedom in our system (we are not sweeping a line cursor across the target as in a SPIFI system), we must find some other meaning to ascribe to the shape of the frequency space peak. We will set this question aside for the moment, but rest assured my dear reader: we shall return to this conundrum.

It is worth noting that when we first examined the periodogram of this signal, we computed it using a large number of samples, which lead to spectral self interference due to computing the FFT over multiple periods of the beam changing directions (adding an unwanted modulation). By looking at a shorter period of time, the interference was eliminated, resulting in a clean signal.

We now ask ourselves what sort of information we can quickly gain from the periodogram without too much analysis of the shape of the peak. Given the Gaussian nature of the beam, we know that the brightest part of the laser beam is at the center. Therefore, we expect the periodogram will have a maximum at the frequency corresponding to the mask row over which the beam is centered. By doing a bit of math using Equation 4.4, we can determine the spatial frequency of the row being “activated” by the center of the laser beam. From there, we need only examine the mask parameters to determine the location of the center of the beam, giving us a crude measurement of flow position. Additionally by examining where the peak gets sufficiently close to zero, we can even determine the extent (in the direction perpendicular to the sweep) of the target. However, care must be taken to account for spectral leakage: an unavoidable consequence of finite temporal windows which will blur the edges of the peak. The longer the temporal window, the less spectral leakage that will take place. Therefore, in a real system, we would want the 2D mask to be as long in the flow direction as practical. In any case, we can get flow position and size information based upon the periodogram. Moreover, since the row size is rather small, we can achieve a much finer flow position and size resolution (provided that spectral leakage is minimized) than with the 3 and 5 row modulation masks we considered previously.

On the surface, the technique we used here may seem rather different than the analysis used for the 3 and 5 row modulation mask models. However, the physical mask is the same sort of idea, it just has a great deal more frequencies with small row depths. In fact, the spatial frequency step size from row to row is sufficiently small that it appears continuous at the macro scale (and the scale of our laser beam), giving a far more precise location of the center of the target. This experimental result confirms what we already believed: more rows in the mask gives more information. However it does come at a cost: the individual peaks get washed out in the periodogram, making it harder to place a precise bound on the target due to the effects of spectral leakage. Fortunately, this is likely not insurmountable. We strongly suggest further research by someone more familiar with advanced signal processing

techniques to determine how accurately the edges of the target can be located in the frequency domain.

With the low spatial frequency region of the mask tested, we naturally opted to test out a region with a higher spatial frequency. As before, we recorded the voltage signal from the photodiode using an oscilloscope, and the trace is shown in Figure 4.30.

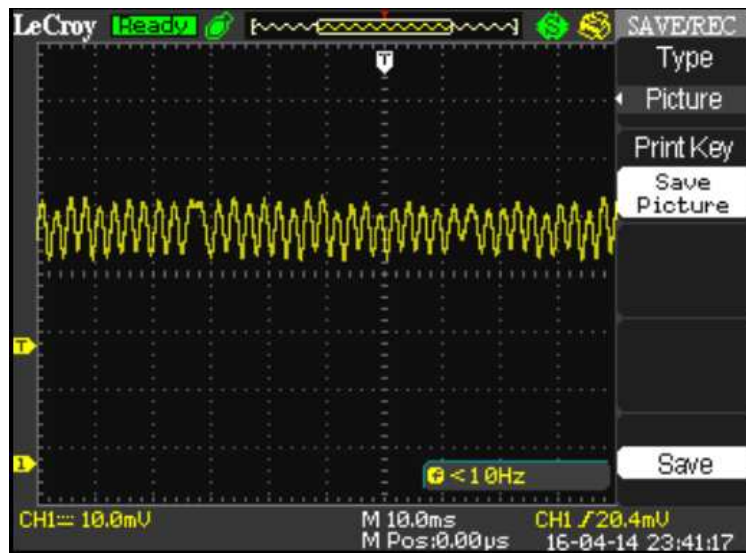


Figure 4.30: Trace of high spatial frequency sweep with a red diode laser

Once again, we have a signal that could be described as a “sinusoid with character”. A quick glance Figure 4.28 confirms that the signal in Figure 4.30 does indeed have a higher temporal frequency: a conformation of trends predicted by 4.4. Once again, precious little useful information can be gained by merely looking at the signal in the time domain. Therefore, we computed the periodogram of the signal (again using a Blackman window), which is shown in Figure 4.31.

Once again, we see a roughly Gaussian peak. The peak is centered about 333 Hz, which is indeed a higher frequency than that of the previous signal: a comforting result. We have now demonstrated two things. First, these laser micromachined masks are effective for red light. The second is that even though the mask contains a lot more frequencies than we had present in our test masks that we modeled, the results matched our intuition.

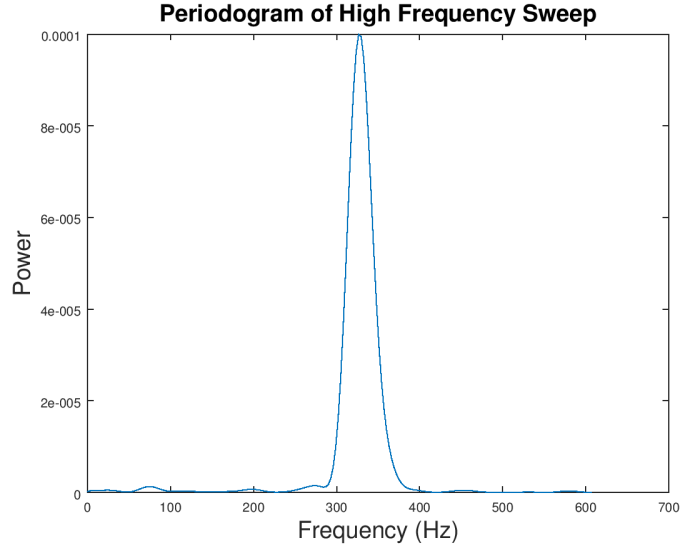


Figure 4.31: Periodogram of High Frequency Signal

While certainly not a primary focus of this research, the system that we constructed provides us a unique opportunity to see how well the femtosecond laser micromachined glass masks modulate a more useful frequency of light. Specifically, we will examine light in the near infrared band, using a Titanium-doped Sapphire laser as the source.

Titanium-doped sapphire, also referred to as Ti:Sapphire, has found itself as the workhorse in femtosecond optics. Its broad absorption band allows for a wide variety of optical pumping solutions. Additionally, it has a broad fluorescence band, allowing its output to be tunable between 670 nm and 1070 nm [25], which directly lends itself to ultrashort laser pulses [25]. Due to these capabilities, Ti:Sapphire lasers are a popular choice for SPIFI systems examining biological media. As such, it is logical to test how well the femtosecond laser micromachined glass masks modulate a Ti:Sapphire produced laser beam.

In order to test the mask, we slightly modified the testing apparatus shown in Figure 4.26 by removing the red diode laser and replacing it with a Ti:Sapphire laser beam of wavelength $\lambda = 800$ nm. Due to the beam being outside of the visible spectrum, alignment of the new beam required the use of near IR beam cards, which fluoresce in the presence of IR light. Using our apparatus, we swept the beam across a row with an intermediate spatial

frequency and a row with a high spatial frequency. Using an oscilloscope, the medium and high frequency traces were recorded, and are shown in Figure 4.32 and Figure 4.33 respectively.

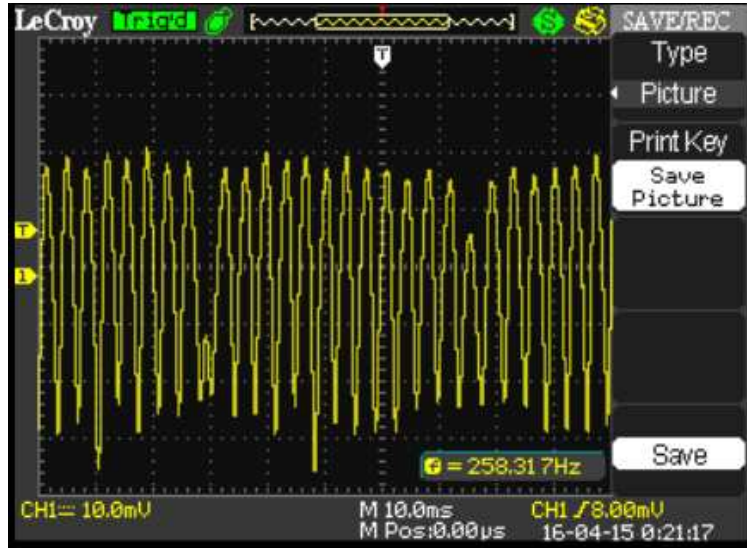


Figure 4.32: Trace of intermediate frequency sweep with a Ti:Sapphire laser

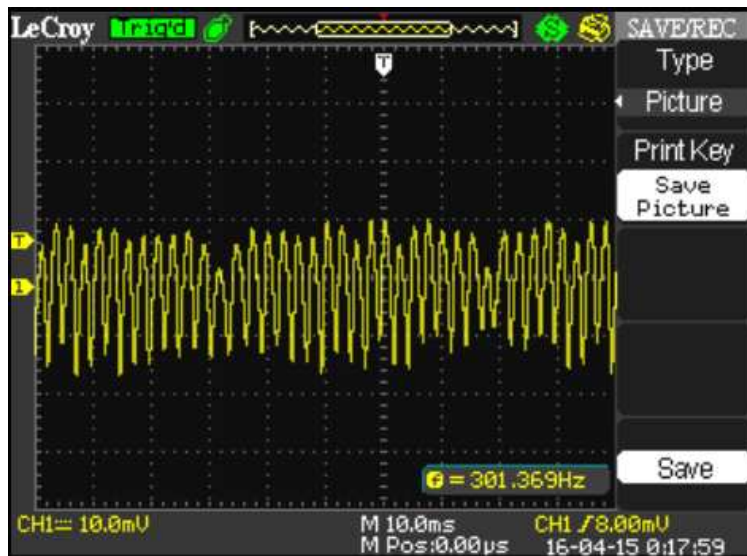


Figure 4.33: Trace of high sweep with a Ti:Sapphire laser

We once again see sinusoidal signals whose frequency is directly proportional to the spatial frequency of the row across which the laser beam is being swept: a useful result, but

not surprising based on the test done with the diode laser. What is truly interesting about the test with the Ti:Sapphire light is the first conclusive demonstration that femtosecond laser micromachined glass masks can modulate light in the near IR band. This means that inexpensive, rapidly manufactured, and geometry flexible masks can be used in the well developed field SPIFI microscopy. While the masks are rarely the most expensive part of a SPIFI system, the benefits of laser micromachined masks are remarkable. While the rest of the experiments conducted in this thesis utilize the red diode laser, this result has the most immediate use. After modulation of near IR with the micromachined masks was achieved, the masks were demonstrated to be able to be used in conventional SPIFI imaging [26].

4.7 Assigning Meaning to the Shape of the Periodogram

As we promised, the reader’s patience will be rewarded as we examine what sort of meaning we can get assign the shape of the periodogram. We will briefly recall how the 1-D line SPIFI with a static mask functions. A line cursor sweeps back and forth across a mask. The mask modulates the line cursor. Using a scan lens, the modulated light is imaged to the microscope objective. When the line cursor stays still, it images a line element on the microscope objective. This line element image is recovered by examining the FFT of the intensity signal. Specifically, the shape of the target (with the beam profile removed) is given by the peak in frequency space. In order to construct a 2D image, the line cursor must also be swept across the target. One way this can be accomplished by moving the target across the line cursor.

We now can compare and contrast to our current set up. A fluorescent target flows beneath the modulation mask perpendicular to the direction of its frequency sweep. Unlike the conventional static mask SPIFI, we have but one source of “sweeping”. We still have a modulated “cursor” in the form of a moving, fluorescing target. But instead of imaging one line element at a time, we are instead looking at the entire target at all times. As such, all 2D information is being “collapsed” into a single line element of information.

We briefly consider a helper thought experiment. In the case of 2D static mask SPIFI, the first thing we do is modulate a line cursor by sweeping it back and forth across the modulation mask. Suppose that instead of mapping the line cursor to the target, we instead expand it into a rectangular beam. This could be accomplished by using a cylindrical lens whose focal axis is perpendicular to the line cursor (just like the technique used in 2D cascade SPIFI). The rectangular beam would have a frequency sweep along its vertical axis, but no frequency variation along the x axis. The modulated line and rectangular cursor are shown in Figure 4.34.

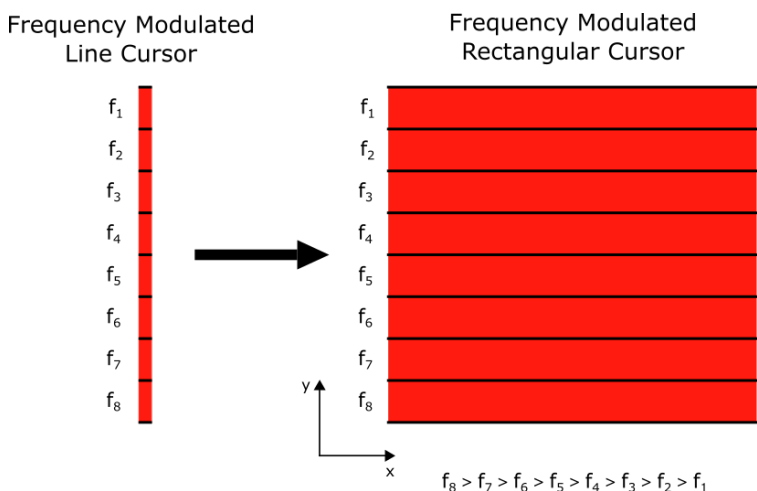


Figure 4.34: Frequency Modulated Line and Rectangular Cursor

The frequencies listed (f_1, f_2 etc) are the temporal frequencies corresponding to the channels shown. Note that the black lines in the cursors serve as demarcations between the carrier frequencies induced by each row of the mask, and do not exist in the lab. Our thought experiment does not, on the surface, bear much resemblance to our situation, but we make the following observation that should alleviate any trepidation on the reader's part. Exactly like our mask/microfluidic channel apparatus, we have a temporal carrier frequency sweep in the y direction with no variation in the flow direction.

We can think of the situation another way. Consider the reference frame of the target in a microfluidic channel. As the mask moves over the target, it modulates the light hitting

the target (or fluorescing from the target) in precisely the same way as the rectangular cursor in Figure 4.34. Should that not convince the reader, consider one more explanation. Suppose we imaged our 2D mask onto a cylinder and enforced periodicity. We then transmit a rectangular beam of light, originating at the center of the cylinder, through the mask while spinning the cylinder while imaging a static target. Once again, we get the same result as the rectangular cursor in Figure 4.34. These situations are all equivalent.

Having (hopefully) convinced ourselves of the equivalence of our thought experiment, we now consider a circular target under the a SPIFI generated rectangular cursor, which we show in Figure 4.35.

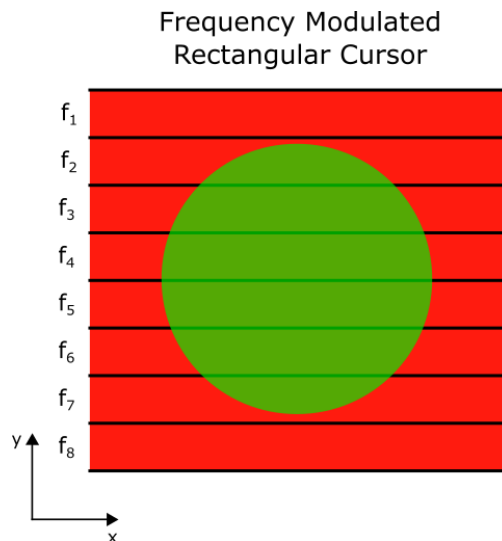


Figure 4.35: Frequency Modulated Line and Rectangular Cursor

Suppose we collect all light from the target for sufficient time window and examine its periodogram. Assuming that these temporal frequencies are sufficiently far apart so as to appear as separate and distinct peaks in the periodogram, we expect to see 6 different frequency peaks corresponding to the rows with which the target is interacting. But the mere presence of these peaks is not terribly interesting: we already developed a framework for understanding that phenomenon with the 3 and 5 row modulation mask. What we are really interested in is how much power is in each peak. Because the frequencies of each row

are distinct, we can consider them separately.

So long as the target fluoresces with equal amplitude across its area, the amount of power in a given frequency component in the periodogram of our thought experiment should be proportional to the amount of area of the target being activated by the row corresponding to the frequency in question. We believe this line is significant enough that it bears restating: the power of a given frequency component will be proportional to the square (as the photodiode measures intensity) of the amount of target area activated by the corresponding mask row. Because of the lack of frequency variation along the x axis (direction of flow), we are in effect integrating across target area interacting with each different modulation frequency row. When we integrate the amount of light (which is proportional to area) in a row, we are collapsing the information about area into a single quantity which we recover by measuring the amount of power in the corresponding frequency peak.

We quickly note that in the situation shown in Figure 4.35, the row depths are about one less order of magnitude than the size of the target. In a very real sense, we are integrating the area information in each region of constant frequency (or row). The deeper the rows, the less resolution that we have as we are integrating over a curved surface. In fact, we can directly compare this to approximating integrals using rectangles. Our system gathers amplitude information about these rectangular row regions based on the area. When we reconstruct the 1D line element, we can reconstruct the target (provided we have uniform fluorescence) using these rectangles. Just like in those primitive integration techniques, we achieve much finer results when we shrink the depth of those rectangles.

Now, suppose we reduced the row depth such that it was two orders of magnitude smaller than the target (adding additional frequencies as well). We are now getting amplitude information averaged over a much smaller “step size”. In fact, if we reduce that row depth (or step size) sufficiently, we can actually get a reliable characterization of the shape of the target! We can therefore collapse some information about the shape of the target into a one dimensional signal. We do still lose a lot of shape information when we collapse it into one

dimension: we cannot cheat the consequences of losing a degree of freedom. However, when certain information about our targets are known (as is the case in red blood cell cytometry), we can make rather informed approximations.

A fair question to ask now is what are the limitations? We mentioned that there is a loss information, so what goes missing? First, we remind ourselves that we are reducing all fluorescence information in a particular frequency row to a single number (amplitude) by way of an average. If we restrict ourselves to a target that is both continuous (no holes or gaps) and has a uniform fluorescence, then the only information that we lose is curvature in each row. That sort of a target is highly idealized, but not necessarily completely unrealistic. For a red blood cell, we can safely assume that there are no gaps or holes in the target. As for uniform fluorescence, the validity of the assumption becomes less clear. However, we can (and will) assume a “first order approximation”: that the fluorescence is approximately uniform. When we relax these assumptions, we run into trouble, since the mapping of target area to amplitude is no longer one to one. We run into this ambiguity because a a region with gaps and a region with no gaps with the same area and uniform fluorescence would result in the same amount of signal amplitude at the corresponding frequency. In the general case, we have a more difficult time getting a lot of useful information when we collapse target information into a one dimensional array. We make sacrifices for simplicity. When more specific information is required, we must rely on traditional SPIFI microscopy systems. But for red blood cell cytometry for size measurement, we can get away with the information loss.

A reasonable question for the reader to ask now is “well that sure sounds nice in concept, but being the enterprising scientist or engineer that I am, I need a mathematical model. So where is the math?”. We postpone (only for the moment, we promise) an in depth derivation of a mathematical model of this information collapse and its applications for reasons that will be explained shortly. However, we have hopefully convinced the reader that there is indeed shape information hiding in a one dimensional signal when we impose sufficiently

strict conditions on the nature of our target. Moreover, we contend that red blood cells in a microfluidic channel will obey our conditions, or at the very least, be close enough for horseshoes and a profession that considers spherical cows in a vacuum to be useful models.

4.8 Of Advantages, Disadvantages, and Our Next Steps

In this chapter, we outline, propose, and analyze a fundamentally new method for measuring the flow stream position and size of a fluorescing target flowing in a microfluidic channel. As a quick reminder, the basic set up is to tag red blood cells with a fluorescing dye and have them flow through a microfluidic channel that is beneath a 2D Cartesian modulation mask. By collecting the light using a single element detector and computing the FFT of the time varying signal, we can actually determine the flow position and size of a target. We also touched on (qualitatively) how it is possible to get shape information about certain classes of targets from the one dimensional signal. We even showed that an area function could quantitatively be recovered using the primitive modulation mask.

The key advantage of our system is simplicity and relative lack of expense. We can achieve these measurements without an expensive CCD camera and without computationally expensive edge finding software. But lets take a moment and recall our ultimate goal: we desire to measure the size of a target *whose size is varying* for the purposes of measuring the mechanical properties of red blood cells. We have, for the entirety of this chapter, been looking at targets with constant size.

When the target is changing size as a function of time, we note that the frequency content (both range and amplitude) of our signal will now also be a function of time. In order to estimate the Young's Modulus of Elasticity of a red blood cell, we want as many data points (size vs time) as possible. This leads us to the wonderful world of Short Time Fourier Transforms (STFT), the Gabor Transform, and even Wigner transforms. These, and other techniques, allow us to examine how the spectral content of a signal changes with time. All have their various advantages and disadvantages, which is a discussion for another time. For simplicity, we will focus on the STFT, due to its relative simplicity. In any case, there are a

plethora of techniques at our disposal to examine how the frequency components of a signal changes with time.

Let us allow ourselves to be naive for a moment. In order to accommodate targets whose size is no longer constant, we should not need to change a thing! We need only use a STFT to examine the periodogram at different points in time, giving us size (and maybe even shape) information for the target as it relaxes from its stretched state. Easy as π , right? Well, maybe. But it is rather unlikely. The principle of time-frequency complementarity rears its ugly head. When we chop up a signal using a STFT (or any other method) to see how the frequency changes with time, we must make a tradeoff between responsiveness (i.e. size of our time steps) and spectral leakage. Its one of those unpleasant facts of physics and signal processing. In order to get as accurate information as possible, we want as many cycles of our modulated signal as possible, so that we have plenty of signal to examine as its frequency content changes. But this also must be accomplished in a tenth of a second. From a design perspective, this means that the target must flow as quickly as possible beneath a long mask (a mask with lots of modulation cycles). Well that is fine and dandy right? Probably not. In this chapter, we have considered masks with rows whose spatial periods are greater than or equal to the diameter of our target. Other geometries are available, but have other trade-offs. Physically, this requires us to drive the blood cells distances much greater than its diameter in short amounts of time. The ability to make the fluid move fast enough is not going to be the limiting factor. Unfortunately, red blood cells will likely deform at high speeds due to fluid shear stress [27], which complicates the measurements considerably. At flow rates of approximately $50 \mu\text{m/s}$ in a $150 \mu\text{m}$ wide microfluidic channel, flow induced shear stress is negligible [1]. Given that an $8 \mu\text{m}$ blood cell will flow less than 10% in 0.1 seconds (the characteristic relaxation time), it seems rather unlikely that we will be able to get enough data to determine the size of the cell as it relaxes to an unstretched state.

While flow induced shear deformation is a bug for our proposed architecture, but is in fact a feature for another method of elasticity measurements. Indeed, a different technique

for measurement of cell elasticity relies upon deformation induced under shear stress [27]. However, these techniques are generally incapable of recovering information about individual cells, which is where optical stretching as a technique shines [1]. We note that a static modulation mask architecture can be used in concert with flow induced deformation by having a low shear stress measurement stage with a single modulation mask and a high flow shear stress stage with a second modulation mask. The static mask architecture has a key advantage in such a set up: lower expense, due to avoiding using high speed cameras for measurements. We propose that a multistage system be investigated as a part of further research into the performance characteristics of the static mask architecture.

Another issue comes from a different case of spectral leakage. Our size measurement method relies on examining where the primary peak in the signal periodogram goes to (or sufficiently close to) zero. If our sampling window is not wide enough, we will have spectral leakage making it difficult to ascertain the edge location, due to the property of time-frequency complementarity. We recall that our time window is a function of target speed and the mask length. In order to achieve measurement fidelity, we want to have a long mask in order to have a wide enough temporal window. Having a long enough mask for may pose design challenges, though they are likely possible to overcome. In any case, system designers using the architecture presented in this chapter must account for spectral leakage even when measuring targets whose size does not change.

The issue of examining the change of frequency components over time poses a substantial challenge to our ultimate goal of measuring red blood cell plasticity using optical stretching. But let us not overlook how far we have come. Remember: flow position measurement, size measurement, and shape characterization of targets whose geometry does not time evolve can be accomplished with our proposed system. As we mentioned before, we hold off on developing the mathematical theory fully, but rest assured, the model we develop shortly will apply to a static mask system.

A final possible issue is that the cell will undergo some nonzero amount of Brownian motion while flowing in the channel. Such drift would present as a drift in the central frequency of the output signal, which would be visible upon examination of a spectrogram. Additionally, the cell may tumble while in the flow due to the velocity gradient inherent to laminar flow. A tumbling cell would have the frequencies present also change dramatically, which would be visible in the spectrogram. Fortunately, as we searched literature on cell elasticity cytometry, we found no references to such behavior, so we consider the probability of these noise factors effecting the measurement to be low. However, it is a noise source worth monitoring when developing this system.

CHAPTER 5

CELL SIZE MEASUREMENT AND SHAPE CHARACTERIZATION WITH SPINNING MODULATION MASKS

When initially trying to overcome the issues we presented that effect the 2D modulation mask architecture, we attempted to simply avoid them to begin with. Unfortunately, our efforts were really just patches, and would not be very effective for measuring a red blood cell as it relaxes from a stretched state. No matter what tweaks that we made to the mask or clever signal processing tricks we thought about, the issue of dealing with changing frequency components to measure time varying target size proved insurmountable with our efforts. Initially, we lowered our sights, allowing ourselves to be content with flow position measurement, size measurement, and shape characterization of targets of constant size with a static modulation mask.

However, when we were just about to settle, we took a second look at spinning mask SPIFI architecture. After that closer look, we found our salvation. While our proposal does have its limitations and disadvantages, we believe that, properly implemented, it may lead to the achievement of our ultimate goal: an inexpensive, simple, high throughput, and widely deployable system for the measurement of red blood cell plasticity. In this chapter, we outline our motivations and proposed system design,

5.1 A Spinning Mask Thought Experiment

After setting aside the static modulation mask architecture for measuring blood cells relaxing from a stretched state, we initially considered a primitive spinning mask SPIFI system. Consider then ordinary spinning mask SPIFI system, like the one outlined in Chapter 2.2. As a reminder, a beam line cursor is modulated by passing it through a spinning mask (along a radial vector) which has a spatial frequency that linearly varies with its radius. Suppose that instead of having the modulated beam cursor sweep across the target, as in

the case of conventional microscopy, we allow the beam to remain static. Using a microfluidic channel, we can place a red blood cell beneath the cursor, such that the cursor runs down the center (or nearly the center) of the target. Using optical tweezers (operating at a wavelength that does not activate the fluorescent dye tagging the cell), we can stretch the target and then allow it to relax, just as is done in the current state of the art.

Using very much the same methods for analysis as proposed in the previous chapter, we can recover flow position and size information. After all, the fundamental idea is the same. The modulated line cursor will cause the target to fluoresce. By examining the frequency content of the time varying intensity signal at our single pixel detector, we will see that frequencies corresponding to the location and size of the target are activated. If we know the basic parameters of the system (mask element size, rotation speed, etc) we can determine the size of the target by looking at where the periodogram peak goes to zero. By noting which frequencies activated, we can determine where in the flow the target is.

But what problems does this shift in architecture solve? The key thing we accomplish here is the removal of the relationship between rate of temporal modulation and the speed of the target. Previously, the modulation frequency of a given row was directly proportional to the speed of the target within the flow. As a direct consequence, the number of modulation cycles that we see in the signal was limited by target speed as well. This got us into trouble, since we need as many signal periods as possible in order to avoid the nasty consequences of spectral leakage. With this thought experiment, the modulation frequencies and relative size of the temporal window to signal component periods is controlled entirely by the parameters of the modulation mask and the rate at which the *mask* spins. We can control the mask element parameters during manufacturing, being limited only by the limitations of our fabrication process.

Another key feature of this thought experiment is the fact that we have a built in time scale for the natural application of STFT analysis. Each time the mask completes a full rotation, a transparent wedge region of the mask brings all parts of the mask back into

phase with one another. This results in a brief period where no modulation takes place, and introduces a periodicity of frequency far lower than the modulation mask otherwise provides. As we will see later in this chapter, this creates a time varying signal that comes in separate and distinguishable packets. Inside the packet, we see a time varying signal. Between each packet, we see a steady DC component (the whole DC component of the signal is easily removed in post acquisition processing). This low frequency repetition of the signal encourages us to analyze the signal one packet at a time. If our temporal window when looking at the periodogram includes more than one packet, we see modulation of the peak in the periodogram due to spectral self interference.

While these effects can be removed (and even utilized), these packets provide natural built in intervals for STFT analysis, as we can compute the periodogram for each packet easily. For a target whose size is changing in time, we can simply compute the periodograms for a the sequentially collected signal packets. By comparing the size and shape information encoded in the frequency domain of each packet, we should be able to make observations about how the target size and shape changed with time. In order to make such measurements of red blood cells relaxing from a stretched state, we would need to collect as many packets as possible (around one hundred measurements per second is the current state of the art). The number of packets per second is directly related to the angular velocity of the mask, which is limited only by the motor spinning the mask and the physical properties of the mask itself. Spinning the mask that fast may be a challenge, though it is hardly insurmountable. We can also increase the spatial frequency of the mask and apply STFTs to pieces of each packet. In any case, the fact that we no longer have to modify the flow speed of the target in order to effect time window size and temporal frequencies allows us to achieve high frequencies without risking target deformation due to high flow rates.

A quick examination of our thought experiment reveals a lot of advantages of the spinning mask architecture when compared to that of the static mask. However, the set up proposed in our thought experiment fails to meet a key criteria. In order for any system that we

design to be useful in our desired application, it must be capable of high throughput. The system in our thought experiment requires that we hold the target still by pausing flow in the microfluidic channel, meaning that we introduce a delay between measurement of targets. This substantially limits how quickly we can analyze the large numbers of red blood cells necessary for statistically useful measurements. Another difficulty imposed is the need for the cell to be centered on the line cursor so as to measure its full extent. While this is not exactly required, it will be easier to see the small changes in target size when the line cursor runs through the center of the target parallel to the direction of stretch. Such positioning requires a great degree of precision, which both adds expense and once again slows down the throughput of our system.

5.2 A Proposed Spinning Mask System

In order to make use of the advantages provided by a spinning mask architecture, we had to solve the issue of throughput. After some consideration, we initially decided that the issue was too great, and returned to finding ways to mitigate the issues we encountered with our static mask architecture. After all, we believe that our novel static mask architecture does have useful applications. However, we were struck with a moment of insight. We recalled the design of the 2-Dimensional SPIFI system using two cascaded spinning mask. We recall that system designed by David Winters and Randy Bartels used a 2 dimensional cursor instead of a line cursor. As a quick reminder, the 2D excitation beam is created by first sending a standard laser beam through a cylindrical lens, creating a line cursor. This line cursor is then modulated using a spinning modulation mask. Next, the beam is rotated 90 degrees (so as to be orthogonal to the first modulation direction) and modulated with a second spinning modulation mask. The light is then imaged to the microscope objective. The final result of such cascading is a two dimensional cursor whose modulation frequency varies in both x and y, allowing for any point within the excitation beam to be mapped to a temporal frequency.

Our key insight came from realizing that a 2 dimensional cursor need not be modulated in both x and y. We asked ourselves what would happen to the modulation beam if we

removed the second modulation mask, and the answer surprised us both with its simplicity and utility.

Without a second modulation mask (and adjusting the positions of the other lens' in the system to compensate), we achieve a 2D modulation cursor (which for convenience, we will pretend is rectangular) that has modulation in but one direction. In effect, we are taking a modulated line cursor and stretching it out in the direction orthogonal to its frequency modulation by using properties of cylindrical masks. The astute reader may have a mild tingling sensation at this point: we have seen this sort of cursor before. It is to our benefit to examine the line cursor produced by such a set up in Figure 5.1.

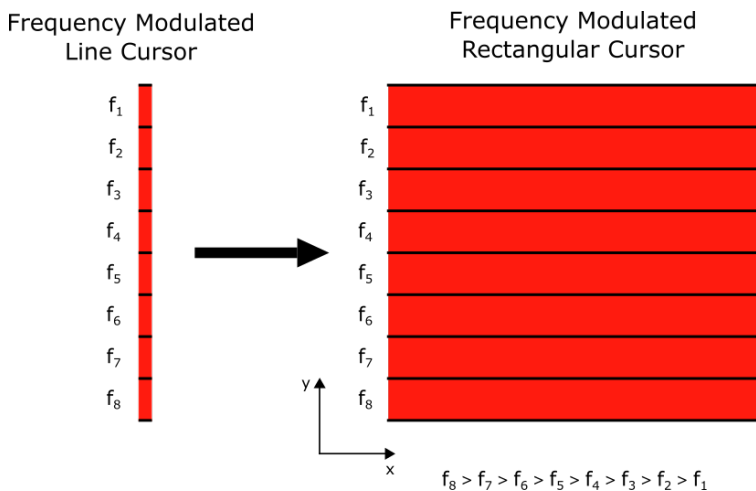


Figure 5.1: Frequency Modulated Line and Rectangular Cursor

On the left, we have a vanilla modulated line cursor created by sending a beam line through a spinning modulation mask. After transmitting the modulated line cursor through a cylindrical lens with a focal line orthogonal to the modulation direction, we expect to see a 2D excitation beam shown on the right of Figure 5.1. The end result is a rectangular cursor with frequency modulation along the y axis, but with no such variation along the x axis. This means that, when holding y constant, frequency is constant along the x direction within the excitation beam.

We note, with more than a mere hint of excitement, that the excitation beam described above is the *exact* same cursor that we discussed in our thought experiment in the last chapter with one key difference: the modulation parameters are not dependent upon flow speed of the microfluidic channel. Instead, the properties of the cursor are controlled entirely by the mask design and the rate at which it spins. We note that this was one of the key advantages delivered by the use of a spinning mask architecture for cell measurement. But does this proposal solve the key challenge of throughput? To our elation, it does! By stretching out the line cursor in the x direction, (so long as the extent in the x direction is substantially longer than the diameter), we eliminate the requirement that we hold the cell still as it stretches and relaxes. We can now stretch the cell and allow it to relax as it flows (in the x direction) underneath the excitation beam. Since we no longer must pause the microfluidic flow for each measurement, we believe it will be possible to achieve a high throughput cell cytometry system based a novel spinning modulation mask system architecture.

Up until now, we have touched on how such a system would be constructed by using the 2D SPIFI cascaded mask system as a baseline, but it is now necessary to specifically lay out our own proposed architecture, which we do in Figure 5.2, and discuss below.

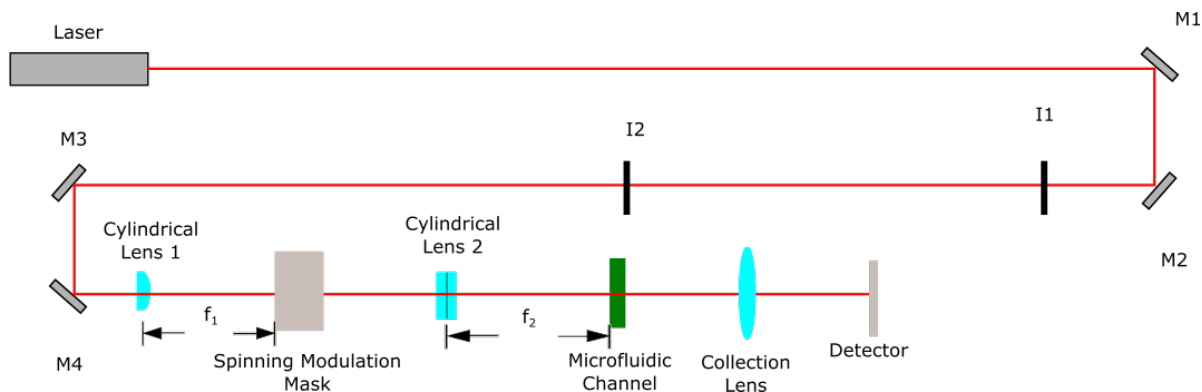


Figure 5.2: Frequency Modulated Line and Rectangular Cursor

As with all of our systems, we start out with a laser as the source of our excitation beam. Laser alignment is accomplished using a series of two mirrors, designated M1 and M2, (each with two degrees of freedom) and two irises at equal height, designated I1 and I2. The

next two mirrors, M3 and M4, are used to redirect the beam due to known physical space limitations in our lab, but are not required. Next, a cylindrical lens to focus the beam into a line, which is mapped to a spinning modulation mask, such that the line is on a radial vector. The modulated beam is then transmitted through a second cylindrical lens whose line focus is orthogonal to that of the first cylindrical lens. The excitation beam, now a 2D (ideally rectangular) cursor, is imaged to the target in the microfluidic channel. Using whatever collection optics are deemed appropriate, the light is then gathered and imaged onto a single element detector.

We wish now to highlight the simplicity of our proposed architecture. The most expensive single component will generally be the laser. A microfluidic system may take some work, but should not be a major obstacle. The rest of the system can be aligned by appropriately experienced undergraduate students in a few hours. It is here that the key advantages of our proposed technique for cytometry are highlighted. These components are reasonably inexpensive. Furthermore, the fact that our measurements require only the use of a FFT of the signal, computations can be conducted in near real time with incredibly inexpensive computers.

It is worth noting that the system shown in Figure 5.2 is simplified. We are ignoring the specifics of the microfluidic channel, avoiding commitment on exact mask parameters, and so forth. However, it provides a framework for our questions and preliminary laboratory investigations of its efficacy. Additionally, it would be difficult to model mathematically something more nebulous than what we have outlined so far. As we discuss later, a specific and well optimized system design was outside the scope of this thesis, primarily due to time constraints. Specific system design, is therefore, left as an exercise to the reader.

5.3 Model and Mathematical Framework

With the general framework established, we must determine a relationship between the time varying intensity signal and the shape of the target in a microfluidic channel. We will do our best to limit our assumptions as much as possible for the moment. Please note that

we use the derivation shown by Winters et al as a starting point, but have modified the approach as necessary.

We begin by examining the excitation beam that has been focused to a line cursor by a cylindrical lens in the modulation dimension (we define y as our modulation axis). The electric field can be modeled by

$$E(y, t) = E_0 u(y) e^{i\omega_0 t} \quad (5.1)$$

where $u(y)$ is a normalized spatial profile field along the line and ω_0 is the optical carrier frequency. The excitation beam is then modulated in both the spatial and temporal domains by the spinning mask, represented as a time and spatially dependent function $m(y, t)$. The beam is then expanded using a second cylindrical lens along the x direction. This preserves the frequency sweep in the y direction, and the electric field can now be written as

$$E(x, y, t) = E_0 u(x, y) m(y, t) e^{i\omega_0 t} \quad (5.2)$$

where $u(x, y)$ is a normalized spatial profile in two dimensions to reflect the two dimensional nature of our field. As a quick sanity check, we see that our equation describes a field with a spatially dependent intensity field that is subsequently modulated in one direction, as we desired. Just as in a conventional SPIFI system, the spinning mask modulation properties can be modeled as

$$m(y, t) = \frac{w(t)}{2} [1 + \cos(2\pi\kappa yt)] \quad (5.3)$$

where $w(t) = \text{rect}\frac{t}{T_m}$ (T_m is the rotational period of the mask) and $\frac{\Delta k}{T_m}$.

Next, the modulated cursor encounters the target. For simplicity, we will only consider periods of time when the target is fully beneath the modulation field, thus ignoring signals when the target is only partially beneath the excitation field. We can model the interaction of the light and the target by multiplying the field by a spatially varying function, $g(x, y)$, which represents the distribution of fluorophores on the sample. We note that if the distribution is roughly uniform, $g(x, y)$ represents the size and shape of the target. Thus, the final electric

field will be given as

$$E(x, y, t) = E_0 u(x, y) m(y, t) g(x, y) e^{i\omega_0 t} \quad (5.4)$$

Next, we collect this light using a lens and image the light to a single element detector, which measures the intensity of the electric field. This intensity is given by

$$I(x, y, t) = I_0 \frac{1}{4} |u(x, y) w(t) g(x, y)|^2 \left[\frac{3}{2} + 2 \cos(2\pi \kappa y t) + \frac{1}{2} \cos(4\pi \kappa y t) \right] \quad (5.5)$$

with all parameters defined as before. When the light is imaged to our photodiode (or other single element detector), it will measure the signal intensity. It will then generate a time varying signal that can be modeled by

$$s(t) = \gamma \iint_S I(x, y, t) dx dy \quad (5.6)$$

where γ is a catch-all constant factor used to account for things such as detector efficiency. The integral is computed over the entire extent of the detector, but functionally should collect the light from the entire area (A) of the 2D cursor.

Just like a conventional SPIFI system, we have three frequency components. One DC component and 2 frequency side bands. We will generally remove the DC component in signal processing, and most SPIFI analysis focuses on the first sideband due to there being more power associated with it. The linearity of intensity measurement and Fourier transforms allows us to consider it separately without losing information and saves us a lot of trouble. Specifically, we are interested in the component given by

$$s_1(t) = \frac{\gamma I_0}{2} |w(t)|^2 \iint_S |u(x, y) g(x, y)|^2 \cos(2\pi \kappa y t) dx dy. \quad (5.7)$$

In conventional spinning mask SPIFI, we would want to convert the cosine term into a complex exponential, making our integral look like a Fourier Transform with respect to κ . If we had frequency modulation in both x and y , we could convert our integral into a 2D Fourier Transform. However, as the excitation field as 2D extent but only one dimension of frequency variation, we run into a bit of an issue cleaning up the math any more.

At this point, we ask ourselves what information we expect to get out of the signal Fourier Transform based upon the form of Equation 5.7. Provided that there are no zeros in the beam profile (except at the edges) or in the interior of the target, we will be able to recover the size of the target measured along the y axis by finding the location of the zeros in the periodogram. By knowing the frequency modulation parameters, we convert the distance between the zeros in frequency space to a physical length.

At this point, we could pat ourselves on the back and call it a day. We have achieved a theoretical framework for size measurement using a spinning modulation mask architecture. But as we discussed previously, there is shape information hiding in that time signal, but how can we get at it? We know that we cannot fully recover the shape of the target due to not having enough degrees of freedom. However, as we discussed in the last chapter, by examining the amount of energy in each frequency component, we can get information about the area in each frequency modulation row. And so long as we have a few suitable restrictions on the nature of the target, that information can be used to reconstruct the shape of the target. Our previous discussion was entirely qualitative, and it is now time to rely on the foundation of much of physics: mathematical skill and intuition.

In taking a closer look at Equation 5.7, we see that it is tantalizingly close to the format of a more conventional SPIFI signal intensity which would allow us to recast it into a convenient Fourier Transform using complex analysis shenanigans. What is stopping us? The pesky $\int dx$ and x dependent functions prevent us from making it look like a simple Fourier Transform. It would be super awesome if we could get rid of that x dependence in Equation 5.7 and just have functions dependent upon y . Unfortunately, neither $u(x, y)$ or $g(x, y)$ can readily be expressed as products of functions dependent on x and y .

After staring fruitlessly at Equation 5.7 for a while, we were hit with another flash of inspiration. With our static modulation mask system, we argued that shape information about the target was encoded in the amplitude of the signal. Specifically, the amount of power at a given frequency in the signal periodogram is directly proportional the total intensity of

fluorophores in the corresponding frequency row region. If we assume that the distribution of fluorophores on the target is uniform, this intensity is then directly proportional to the area of the target in that particular row. To put it into a more mathematically precise language, we are integrating intensity over each frequency row, and the result of that average is encoded in the amplitude at that frequency in the periodogram. The end result is that the shape is encoded in a one dimensional vector, which we designate as an “area function”.

At this point, we made a leap based upon nothing more than a bit of hope and intuition. The area function varies in y alone, but contains information from integrating across the x direction. Mathematically, the area function is the result of integrating $u(x, y)$ and $g(x, y)$ in the x direction, leaving a single function of y . When we get rid of the x integral and x dependency in Equation 5.7, it starts to look a lot more familiar. We can now rewrite Equation 5.7 as

$$s_1(t) = \frac{\gamma I_0}{2} |w(t)|^2 \int |A(y)| \cos(2\pi \kappa y t) dy. \quad (5.8)$$

where we make an ansatz and claim that $A(y)$ is the area function corresponding to the target. Now we have an integral with respect to y alone, meaning we can go one step further by recasting our equation into a Fourier Integral as was done in the derivation for conventional SPIFI microscopy. Our equation can now be rewritten as,

$$s_1(t) = \frac{\gamma I_0}{2} |w(t)|^2 \Re \left\{ \int |A(y)| e^{i2\pi \kappa y t} dy \right\}. \quad (5.9)$$

If we define $f_y = \kappa t$, as was done in the original SPIFI derivation, we can define

$$G(f_y) = \Re \left\{ \int |A(y)|^2 e^{i2\pi f_y y} dy \right\} = \mathcal{F}\{|A(y)|\} \quad (5.10)$$

which allows us to rewrite Equation 5.9 as

$$s_1(t) = \left(\frac{\gamma I_0}{2}\right) |w(t)|^2 G(f_y) \quad (5.11)$$

which is exactly the form that we want. Taking the Fourier Transform of Equation 5.11, we can see that the frequency spectrum can be written as

$$S(y = f \kappa^{-1}) = \mathcal{W}(\kappa y) * |A(y)| \quad (5.12)$$

where f is the signal frequency, $*$ is the convolution operator, and $\mathcal{W}(y) = \mathcal{F}\{|w(t)|^2\}_{f=\kappa y}$.

What this derivation shows is that with our 2D SPIFI based modulation cursor, we can use the exact same approach used in conventional SPIFI to retrieve information about the target. In conventional SPIFI, a single Fourier Transform would be a line element of a target. Therefore, in order to recover a complete image, the line cursor would need to be swept across the target. By piecing these one dimensional signals together, an image is formed. In our architecture, the entire target is “imaged” at once. Therefore, the information that we recover is simply our area function, $A(y)$. While the result shown in Equation 5.12 is remarkable (if true), we are currently relying on the ansatz that our shape information is indeed encoded in $A(y)$. We must now model the area function mathematically.

To do so, we consider a general target and excitation beam profile, $u(x, y)$ and $g(x, y)$ respectively. We will assume that the both functions are nonzero only in a finite region (just as our excitation beam and target), that the excitation beam has a greater area than the target, and that the target is entirely within the excitation beam. These assumptions allow us to integrate only in the bounds defined by the intersection of the beam and the target, as opposed to integrating over the whole real plane. In order to determine what the area function looks like, we recall two things. First, it must get rid of any y dependency by integrating in x as required by Equation 5.8. Secondly, it must be a mathematical representation of averaging across x to collapse target information into a one dimensional signal, as we reasoned must be the case. Based on these requirements, we assume that our area function can be represented as

$$|A(y)| = \int |u(x, y)g(x, y)|^2 dx = \int I(x, y) dx \quad (5.13)$$

where $I(x, y)$ is the intensity of the light produced by the fluorophores and all variables are as defined before. Let us perform a few quick checks on Equation 5.13. First, does the definition make Equation 5.7 equivalent to Equation 5.8? Fortunately, the answer is yes. Equation 5.13 is really just the result of performing the integration in the x direction first in Equation 5.7: we have not broken any rules. We show a quick demonstration of the

equivalence of using the area function in Appendix B. Second, does the function actually give us a one dimensional representation of the target shape, as we argued it must? Once again, it does. The integral in Equation 5.13 is the mathematical representation of integrating intensity information in beam frequency rows. It is this way of integrating, or averaging, that we contended collapses two dimensional shape information into lower dimensional function. We also see, mathematically, how information is lost due to the integral.

So what have we achieved? First, we now have a bridge between Equation 5.7 and Equation 5.9. Equally important, we now have a mathematical way of taking the area function recovered by performing an FFT on the signal produced by our system and converting it into useful information. Although we cannot, in general, take a recovered area function and pull out the original shape function, we can come close if we make some assumptions. For instance, if we have an approximately uniform distribution of fluorophores, we can replace $g(x, y)$ with a constant. Additionally, if we can make a similar approximation to the intensity of the excitation beam, we can similarly reduce $u(x, y)$ to a constant. Our area function then contains information about the distribution of area in the target, which can be readily converted to shape information.

5.4 Recovering Shape Information from the Area Function

We must now back up our outlandish claim that we can actually recover shape information from the area function. We must clearly define the restrictions that must be imposed, the limitations of data recovery, and the capabilities that the area function gives us. Let us begin our analysis by examining an extremely simple case: that of a perfectly circular target. We choose a circular target as it is symmetrical about a line parallel to the y axis that runs through its center, and since we can approximate un-stretched blood cells as circles. We assume that the target has no gaps in regions in its interior. Moreover, we will assume that the excitation beam has a perfectly uniform distribution whose amplitude is normalized to unity, allowing us to drop the $u(x, y)$ term in Equation 5.13. In addition to assuming that geometrically the target is perfectly circular, we further assume that the distribution

of fluorophores is uniform across the extent of target. This means that the intensity of light emitted by the target when exposed to the excitation beam will be the same at any point on the target. Again, for convenience, we normalize the distribution of fluorophores $g(x, y)$ to be equal to unity. We also set the radius of the circular target to be equal to one (using unity everywhere makes the math easier, sue me). With all of these target requirements defined, we can now define our target mathematically. Our function is defined most easily as a piecewise function, which we can write as:

$$g(x, y) = \begin{cases} 1 & x^2 + y^2 \leq 1 \\ 0 & x^2 + y^2 > 1 \end{cases} \quad (5.14)$$

Performing a quick sanity check, we see that our definition of $g(x, y)$ meets the criteria of size, shape, and appropriate normalization: we are good to go. Now, using the definition of the area function in Equation 5.13, we can compute the area function, which is also defined piecewise as

$$A(y) = \begin{cases} 2\sqrt{1-y^2} & -1 < y < 1 \\ 0 & |y| \geq 1 \end{cases} \quad (5.15)$$

which we also plot in Figure 5.3 and note a few characteristics. We see that this is the upper half of a circle multiplied by two. By remembering the definition of our area function, its shape ought to make sense. The widest extent of the target is across its center ($y = 0$), which we see reflected in the function plot as a maximum at $y = 0$. At values of $|y| > 1$, we are beyond the extent of the target, which is reflected in the fact that the area function is equal to zero for these values. We remark that that the discontinuity seen in the plot is due to the plotting software disliking regions of infinite slope, not some actual discontinuity in the function.

The real question would be how to convert $A(y)$ into useful information about $g(x, y)$. By definition of the area function, the amplitude (physically, the intensity of a given frequency of modulated light) of the area function is directly proportional to the average concentration of fluorophores in that frequency row. Because we assumed that the concentration was uniform

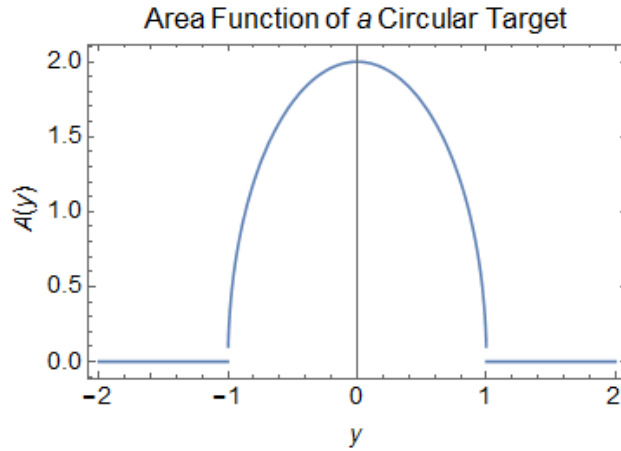


Figure 5.3: Frequency Modulated Line and Rectangular Cursor

across the entirety of the circular target, we can make the following conclusion: the amplitude of a point in the area function is directly proportional to the extent of the target in a direction parallel to the flow direction at that corresponding y value. Since we assume that the target is symmetric along its own vertical axis, we can divide the area function by two and get a representation of the shape of one half of the target. Doing so is done more for a “gee whiz” effect than anything else, but provides a nice bonus feature. We note now that any physical system will have some constants of proportionality embedded into the signal amplitude. Calibration using fluorescent targets of known shape, size, and orientation will be needed in order to determine the exact relationship of a given amplitude in the signal periodogram to a measurement of target extent in the flow direction.

What we have demonstrated that, with some rather harsh assumptions, size and shape (in the form of length measurements in flow direction at different y values) information can be recovered using our spinning mask system architecture. But what happens when we relax our assumptions? After all, our assumptions restrict what sort of targets we can measure, and it would be nice to do more. Let's start by relaxing the requirement of symmetry about the vertical axis of the target and the requirement that the target have no gaps in its interior. We will still assume a uniform excitation beam and that the target has a constant distribution of fluorophores on its surface. We now consider targets that give problematic

area functions. Figure 5.4 shows a few different targets that cause issues to arise in our use of the are function to recover the target shape.

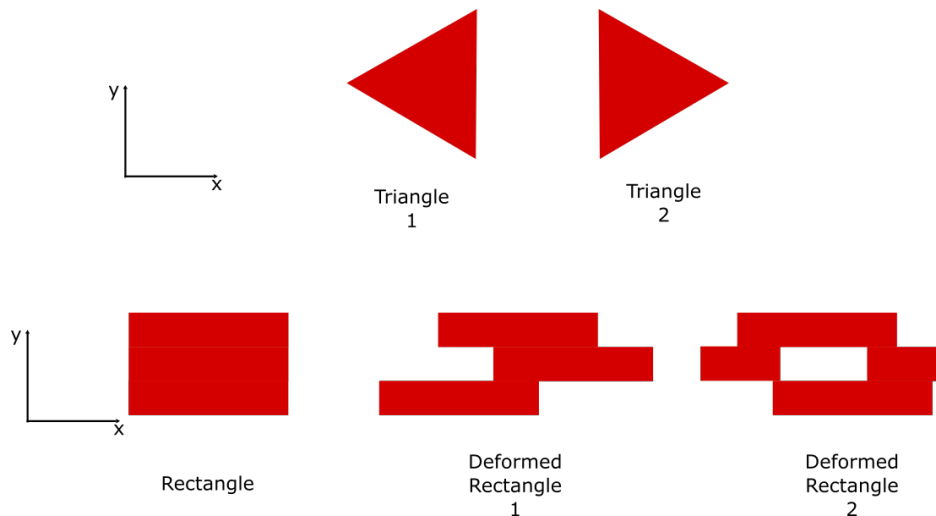


Figure 5.4: 2 Sets of Targets with Equal Area Functions

We first examine the first row of targets: Triangle 1 and Triangle 2. Both are identical in shape and size, but have different orientations. Because our system averages information in the x direction (the flow direction) as described in Equation 5.13, both Triangle 1 and Triangle 2 will have identical area functions. Additionally, because we no longer assume symmetry about the vertical axis of the target, we would not even be sure that the target was a triangle or a rhombus. However, if we were examining targets that we knew were triangular, we might still be able to get useful information from the area function. But even with that restriction, we lose orientation information about the target, and because there is no frequency sweep in the flow direction, there is no way to recover it.

We really run into trouble with then next row of targets in Figure 5.4. We have a rectangular target and two different deformed versions of it. The deformed targets have the exact same total area, and when we integrate across the x direction, all three targets will be mapped to the same area function. The three rectangle-based targets shown above are wildly different from one another: one even has a big gap in its center. But because the total amount of area in any differential dy , they will look identical to our spinning mask system.

Unfortunately, identical targets can also create different area functions if their orientation differs from one another. Consider the case shown in Figure 5.5, where we have three identical ellipsoid targets with different axial tilt. Each will produce different area functions. Each will have different locations for zeros (extent in the y direction), different locations of the maximum, and different values for the maximum. If we know that we are dealing with ellipsoid targets whose orientations are difficult to control, we can probably develop a way of making the area function useful again by doing some careful analysis as to the angular dependence of the target orientation on key parameters. But this example once again illustrates how much information is lost by collapsing two dimensional shape information into a one dimensional signal.

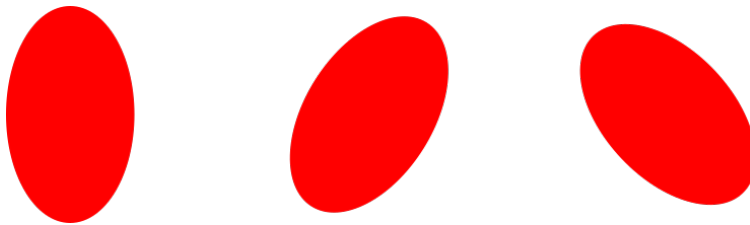


Figure 5.5: Identical Targets with Different Orientations Producing Different Area Functions

Unfortunately, the situation gets worse when we further relax our conditions on the system. If we no longer require that excitation be approximately uniform in x and y, that information just gets averaged into our signal, and suddenly we have a spatial dependence on the intensity of light produced by our fluorescent target. Variation in modulation cursor intensity in the x direction appears to be virtually impossible to resolve. Intensity variation in y can be handled far more readily, as we can expand $A(y)$ into

$$A(y) = \int |u(x, y)g(x, y)|^2 dx = |u(y)g(y)|^2, \quad (5.16)$$

where $u(y)$ and $g(y)$ are the “area functions” (defined as the integral of the function in x) for the modulation cursor electric field and the target fluorophore distribution. We should note that we are being rather tricky with our math, since normally we cannot split up integrals of products in such a manner (and a proper mathematician would just start

sobbing at this point), but it works intuitively. The argument that we make is that because neither $u(x, y)$ or $g(x, y)$ have any variation in x , the integral in x just scales the functions with constants. If our modulation cursor field amplitude has variation in y , we can compute its area function and divide it out of our system measured area function, to get the area function for the target fluorophore concentration. So we can handle modulation cursor amplitude variation in y , but not in x .

The last major wrench that we can throw into our system is relaxing the assumption of uniform fluorophore distribution on the target. When the distribution is no longer uniform, the proportionality between target extent and amplitude of a given frequency component is no longer constant. If the variation is anything more than minor, our recovered area function may be useless. If we happen to know what the distribution of fluorophores on a target is likely to be (perhaps we have a greater concentration due to surface features common across different targets), then it may be possible to tailor analysis techniques to still get meaning out of the area function, but it is more challenging. But too much unpredictable variation in fluorophore concentration will render the area function recovered virtually useless for shape analysis. We will be able to measure the extent of the target in the y direction by analyzing the location of the zeros in the periodogram peak (provided there are fluorophores on the edges of the target), so it is not a total loss, but it does substantially reduce the capabilities of our system.

Based on these examples, we can now lay out certain key requirements that we must impose on our system and the targets that it can measure. First, we will strongly desire targets that are symmetric about an axis parallel to the direction of flow. We need targets to not have any holes in their interior and have the general shape of the target vary little for given targets. The excitation beam must have minimal variation along the axis parallel to target flow, and its y variation must be characterized. Finally, we require that the concentration of fluorophores on the surface of the target must be approximately uniform. Unless all of these requirements are satisfied (or at least are approximately met), the area function

becomes of limited utility. Size measurement can still be accomplished by locating the zeros (provided the fluorophores at least cover the whole target), but that is only one data point for describing the target.

Having performed an in depth examination of the capabilities and limitations, we see that there is power in the approach, but that the information recovered is a pittance when compared to an actual image of the target. Indeed, shape information can be recovered from the area function only under a set of highly restrictive assumptions about the nature of target being analyzed. Our acknowledgment of these limitations leads us to ask ourselves why we bothered with the whole affair of extracting the area function. But fear not, determined reader: we would not force you to read an exercise in futility. It turns out the restrictions that we are required to make are actually fairly reasonable when dealing with targets like red blood cells. Because red blood cells are approximately circular, symmetrical, and continuous, the functional representation of $g(x, y)$ will not be inherently pathological. In fact, red blood cells are the perfect class of target for the spinning mask system architecture.

Even though the area function can recover shape information about a red blood cell (or other circular target), why bother? The whole reason we are doing this research is to improve the state of the art for cell size measurement. We are able to get some size information (extent in the direction perpendicular to cell flow) by examining the location of zeros of the peak in the periodogram. However, we can get more size information by looking at the area function. Using the area function, we can measure the size of the target in the direction *parallel* to the flow by examining the amplitude of the maximum of the peak in frequency space, but we can do better. Since we can recover the shape using the area function with fidelity (due to the geometry of red blood cells), we can drastically increase the number of data points used to characterize how the shape of the cell evolves with time. We have now gone from one data point for measurement to a number limited only by the spatial resolution (number of frequency rows being activated by the target) of our system. This increase in data points allows us to have compute the modulus of elasticity (our ultimate goal) more accurately:

more data points reduces the uncertainty of our measurement.

We now have a mathematical framework for our spinning mask system architecture. We note that the approach we take here is based upon a spinning mask architecture, the same concepts can be applied to our previous static mask system architecture. If we start with the equations used for static mask SPIFI, a similar approach to what we utilized here would achieve a similar result. While the exact details of the things like the window and modulation function differ, we expect a static mask system with a high resolution mask pattern to recover the area function in much the same way as our spinning mask system. We opted to not perform a similar derivation due to the anticipated greater performance potential of the spinning mask system, specifically in the realm of changing cell size. Recall: shape and size characterization using a static mask must deal with issues discussed in the previous chapter. The derivation of a similar model using a static modulation mask is left as an exercise to the reader.

5.5 Experiment and Results

In order to demonstrate that our architecture is indeed viable, it would be well for us to construct a system in order to show proof of concept. Just as with our static mask system, it is logical to construct a primitive apparatus to test our theory, rather than construct our complete proposed system. This allows us to fabricate the experiment quickly and inexpensively, both of which prevent a lot of pain should our theory prove incomplete. We construct the system shown in Figure 5.2 with a couple of minor changes, which are shown in Figure 5.6.

Instead of our target being red blood cells tagged with fluorescent dye flowing through a microfluidic channel, we use a microscope slide with small, millimeter sized opaque targets to block light. In order to compensate for the change in target, we used a 635 nm diode laser instead of a Ti:Sapphire beam as there is no requirement to activate fluorescent dyes. The spinning modulation mask was manufactured courtesy of Nathan Worts using his femtosecond laser micromachining system: a further demonstration of its utility. Using epoxy,

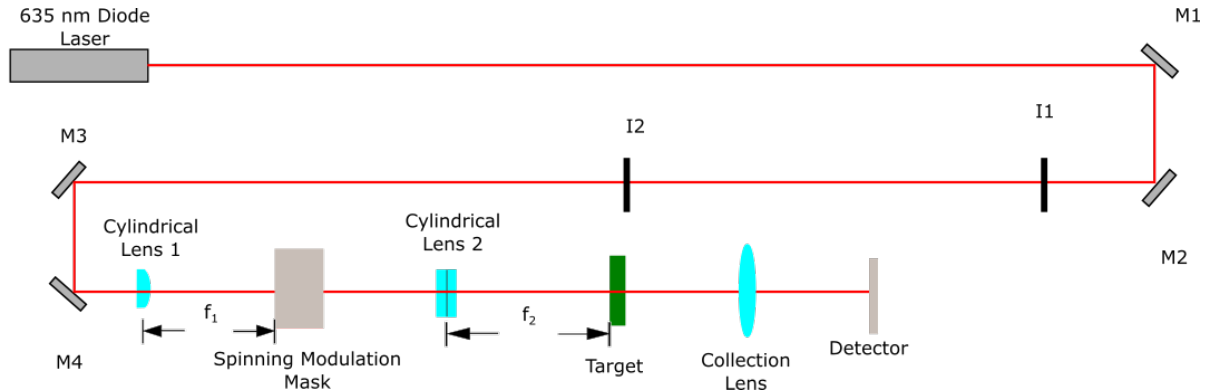


Figure 5.6: Frequency Modulated Line and Rectangular Cursor

it was attached to a spin motor, which was mounted to the optics table.

We must now consider how using an opaque target changes our expected behavior. From a mathematical perspective, it is actually rather simple. We define $g(x, y)$ in Equation 5.13 to be zero over the extent of the target and equal to one everywhere else. Physically, when no target is present, we will recover an area function corresponding to the beam profile alone. Given that most beams (without any conditioning or creative optics) are Gaussian in nature, we would expect our recovered function without a target present also be roughly Gaussian. We verify our intuition by computing the area function, $u(y)$ of some general two dimensional Gaussian, which will be

$$u(y) = \int_{-\infty}^{\infty} A \exp\left(-\frac{(x - x_0)^2}{a} - \frac{(y - y_0)^2}{b}\right) dx = \sqrt{\pi} \sqrt{a} A \exp\left(-\frac{(y - y_0)^2}{b}\right) \quad (5.17)$$

where A , a , b , x_0 , and y_0 are scaling and shifting constants. As we expected, the area function for a generalized two dimensional Gaussian function is a Gaussian in one dimension (with a few scaling constants).

When the target is actually present, it will block some of the light, which ought to cause an amplitude decrease in frequencies corresponding to the modulation rows being partially blocked. We would not expect full attenuation in these frequencies unless the target extent was greater than or equal to the extent of the modulation cursor in the “flow” direction.

For our purposes, we therefore expect the periodogram to have a Gaussian peak with some sort of attenuation shape. In fact, were we to take the recovered area function and divide it by the area function when no target is in place, we would actually simply recover the area function of the target.

Before we detail the data collected and what it means, we must define what we will consider a success. Due to the time and financial constraints imposed in this research, we do not have the resources to build a more complete system. As was stated previously, we simply wish to show that our research has merit. In order to consider our test a success, we would like to meet the following criteria: first, we must recover a signal that makes sense when no target is present. Second, we would like to see a change in the signal when the target is present. Third, we want useful shape and size information to be recoverable from the periodogram. Should we fail to meet any of these criteria, we will examine it more closely to determine the cause. If the issue arises from poor theory, we would have to start over. If it is a technical issue due to the crude nature of our apparatus, then we will discuss mitigation tactics.

We begin by collecting a signal generated by the system when no target is in place. In effect, we are collecting the area function of the modulation beam itself. Before collection, we observed that the beam was not perfectly symmetric. Such imperfections were likely due to a variety of minor alignment and beam quality issues that were not quickly resolvable. As such, we did not expect a perfectly symmetric area function. Additionally, since we have not conditioned the beam otherwise, the laser beam is approximately Gaussian in both x and y . For the purposes of this experiment, this does not cause an issue as we are looking primarily for qualitative results.

When we began the motor that spins the mask, we noted that there was a slight wobble as it spins. We expect the wobble to present as a drift in the central frequency of the modulation cursor. If left unresolved, the edges and interior of the area function will be blurred out, making size and shape measurements less reliable. Fortunately, as we discussed

previously, this wobble can be corrected [17]. Due to the fact that our goal is qualitative proof of concept rather than quantitative measurements, we choose to test whether or not the wobble is present, but we will not attempt to correct it.

Once we activated the system, we observed a periodic signal, a portion of which is plotted below in Figure 5.7. We note that the signal extends both before and after the signal packet shown in Figure 5.7 prior to repeating. We opt to truncate the less interesting part of the signal for convenience. We observe an oscillating signal bounded by an envelope function. We note that this result is consistent with what is observed in conventional spinning mask SPIFI systems [16]: a comforting result. We note that the packet we see in Figure 5.7 is due to one rotation of our modulation mask, and that our envelope is due to the fact that the various frequencies generated by the mask are coming into and out of phase.

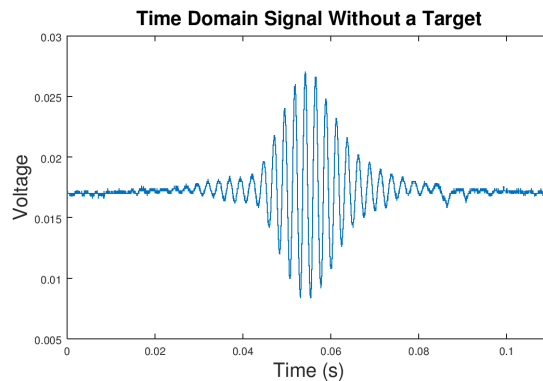


Figure 5.7: Time Varying Signal From Spinning Mask System Without a Target

While an examination of the signal in the time domain is useful, all the good stuff is hidden in the frequency domain. As such, we compute the FFT of the signal, using a Blackman window to minimize spectral leakage. We show the plot of the periodogram in Figure 5.8

For convenience, we normalize the maximum of the peak to one: no need to get lost in the weeds. We observe that our collected periodogram has a roughly Gaussian shape, though

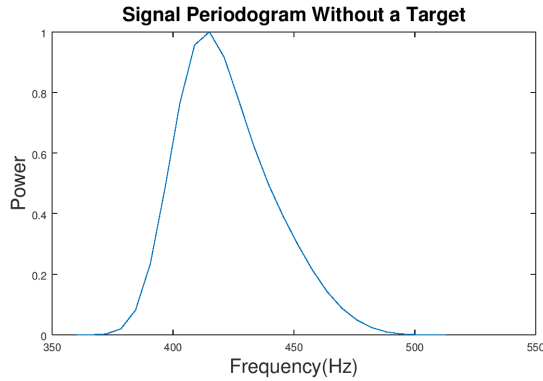


Figure 5.8: Signal Periodogram From Spinning Mask Signal Without a Target

it is indeed asymmetrical. The Gaussian nature is also consistent with what is observed in normal spinning SPIFI systems [16]. However, we still do not have our area function, which is the ultimate goal. Referring to Equation 5.12, we see that if we pretend that the window (we used a Blackman) is perfect, we can recover the area function by taking the square root of the periodogram. While no window that we can actually use will be perfect, we argue that it is close enough for our purposes (it is more reasonable than a spherical cow in a vacuum). Now, by taking the square root of the periodogram, we can recover the area function of our modulation cursor, which is plotted in Figure 5.9. Note that we leave the function in terms of the frequency: no substitution has been made to convert it into spatial information (but we could if desired by knowing the mask parameters).

We note that the area function looks a bit more Gaussian, though it is still asymmetrical. The lack of symmetry, while annoying, is consistent with the beam intensity observed, making the area function qualitatively consistent with our modulation beam: we shall accept this result and declare victory.

Now that we have examined the system without a target, our next step is to examine the signal recovered when we start blocking some of the modulation cursor with opaque targets. To reiterate: fluorescent targets are expected to be superior. But since working with a visible

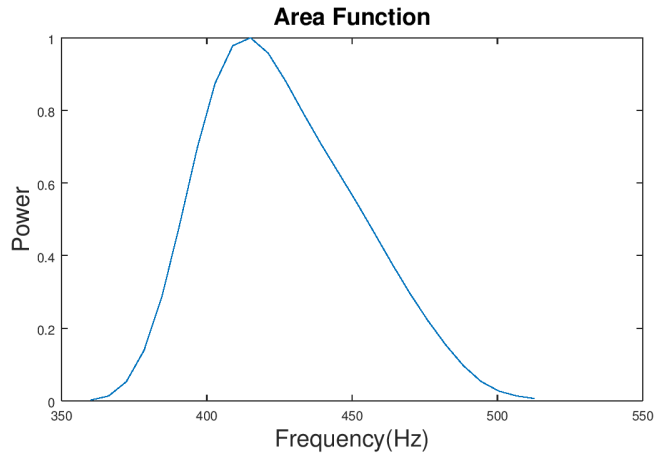


Figure 5.9: Modulation Cursor Area Function

light modulation cursor and opaque targets is far simpler due to ease of construction and cost, we opt to work with opaque targets.

We start with a circular target with a 1 cm diameter. For the target, we used a glass microscope slide with the circle machined using the femtosecond laser micromachining system, courtesy of Nathan Worts. The target is placed at the focal point of the second cylindrical lens so that it is in the same plane as the focused modulation cursor. As before, it is instructive to examine the time domain signal recovered from the photodiode, which is plotted in Figure 5.10. As before, we truncate some of the signal (where the voltage was constant) so as to focus on the part that interests us.

Once again, we see a oscillating function. However, the signal is markedly different from the signal shown in Figure 5.7. While we expect that a target blocking large amounts of various frequency components of the modulation cursor to have a direct impact on the time domain signal, it surprised us how drastic the change was. The nature of the envelope function around the oscillation changed in a clear manner. As comforting as the change in the time domain signal is, we must now look at the periodogram before any useful statements can be made. We compute the periodogram, shown in Figure 5.11. We note that we normalize

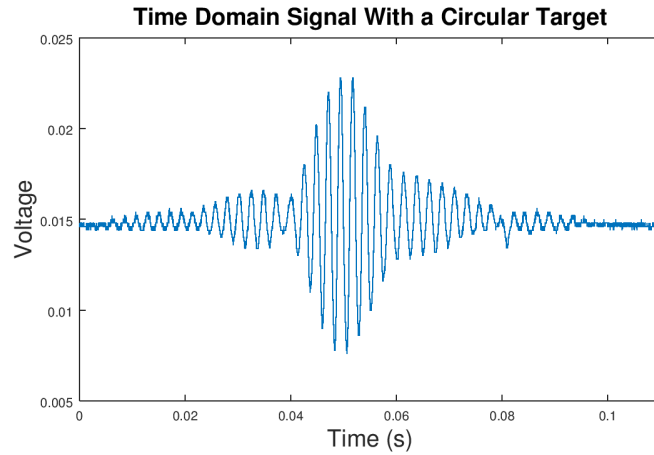


Figure 5.10: Time Carrying Signal from Spinning Mask System With a Circular Target

the periodogram with respect to the periodogram of the signal without a target (our null signal). We normalize in this manner so that we can make meaningful comparisons between the two, with respect to shape and amplitude.

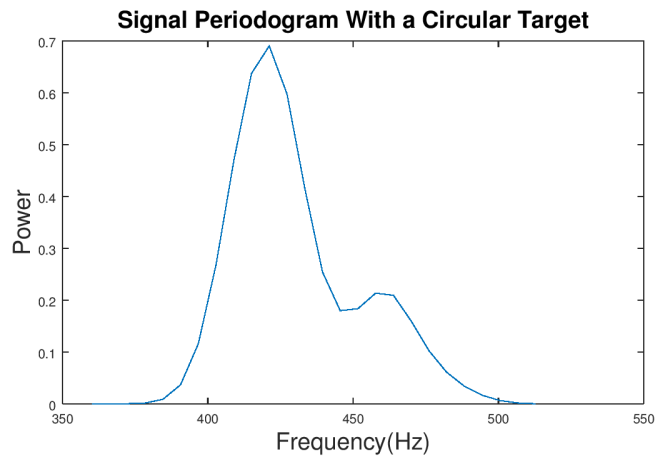


Figure 5.11: Time Carrying Signal from Spinning Mask System With a Circular Target

We immediately see that our signal area function is substantially deformed and its overall amplitude is attenuated compared to the periodogram shown in Figure 5.8. The deformation

is due to the target physically blocking modulation frequencies. As for power, we recall Parseval's theorem. Given that we are blocking light, it makes sense for there to be less total signal power, leading to our corresponding amplitude decrease in frequency space. We note the fact that the deformation is asymmetric, which suggests to us that our target center was not aligned with the modulation cursor center. As before, we can take the square root in order to examine the product of the cursor and target area functions, which we plot in Figure 5.12

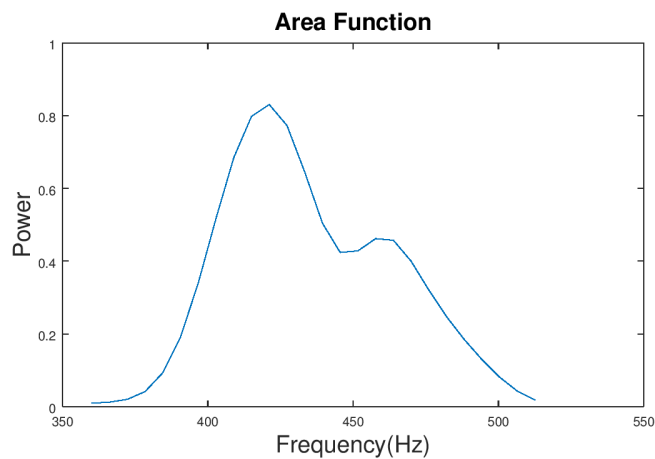


Figure 5.12: Time Carrying Signal from Spinning Mask System With a Circular Target

The presence of a deformed periodogram, area function, and indications of decreased signal power are reassuring, but do precious little to demonstrate a proof of concept. Does the area function shown in Figure 5.12 make any physical sense? Does our painstakingly derived model predict a similar result? We examine the product of the area functions corresponding to the modulation cursor and the target. The area function of the cursor can be approximated as a Gaussian function. Opaque targets are a bit more complicated, but the short version is that the function is equal to one (transmissive) in all regions except for a concave, semicircular region.

After messing with radius, amplitude, and shifting parameters (detailed below), we arrive at an area function that looks rather familiar. We defined our area functions as

$$u(y) = \exp(-5x^2) \tag{5.18}$$

and

$$g(y) = \Re\{1 - 2\sqrt{0.08 - (x - 0.10)^2}\} \tag{5.19}$$

respectively. The specific constants are not terribly interesting, but the situation that they describe is relevant. These area functions describe a gaussian beam and a circular target whose width is a bit smaller than the beam width. Additionally, the target is off center. Moreover, the scaling constants describes how the target blocks a good chunk of light near its maximum, but not all of it. With the postulated area functions described, we plot $u(y)g(y)$, or the full signal area function, in Figure 5.13.

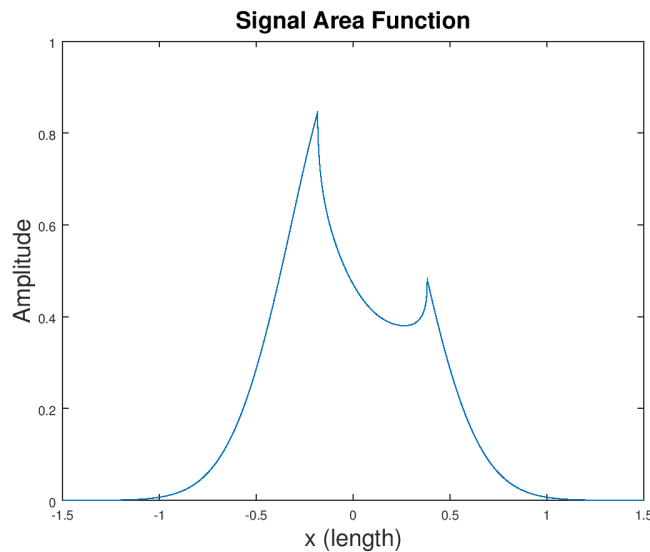


Figure 5.13: Time Carying Signal from Spinning Mask System With a Circular Target

Instead of frequency, we use length on the x axis. Recall, frequency can be transformed into x position and vice versa. We see an area function that is incredibly similar to what we see in Figure 5.12. It is asymmetrical and has the same general shape and attenuation. But what about the sharp edges? Recall, the information shown in Figure 5.12 is not simply

the area function (though that is a convenient fiction), it is the total area function *convolved* with the Fourier Transform of a temporal window function. All sampling introduces spectral leakage, which will smooth those corners, making Figure 5.12 and Figure 5.13 qualitatively consistent with one another. Our system and theoretical target are both rather crude, but we have shown a case in which our model produces results consistent with what is observed by the spinning mask system. It is worth noting that we repeated the experiment several times, each time resulting in similar periodograms and recovered area functions, lending further credence to our assertions.

A fair question for the earnest reader to ask is why we used a model test case, instead of dividing out the modulation cursor area function that we recovered previously in order to get the area function of the target? After all, Equation 5.12 and Equation 5.13 tell us that separating the cursor from the area function is not difficult. So why did we go a different path? We did indeed attempt to recover the target area function in this manner, but our results were fairly useless and random. This caused us substantial concern, until we realized that our spinning mask was still wobbling. In order to verify the presence of mask wobble, we modify our system set up a bit.

We first remove the target from the system and the second cylindrical lens (the lens turning a line cursor into a 2D modulation cursor), giving us a one dimensional line of frequency modulated light. Then, using an optical iris, we block all but a small portion of the line cursor. We therefore expect the transmitted light to be composed of a small number of frequencies that remain constant over time. In other words, if there is no wobble, we expect there to be no variation in the frequency components of the transmitted light. If wobble is present, we expect to be able to see changing frequency components in a spectrogram, which we show in Figure 5.14. Darker colors indicate low amplitude and brighter colors indicate greater amplitude.

As stated previously, if no wobble were present, we expect the frequency distribution to remain unchanged over time. This would present in the spectrogram as a straight line

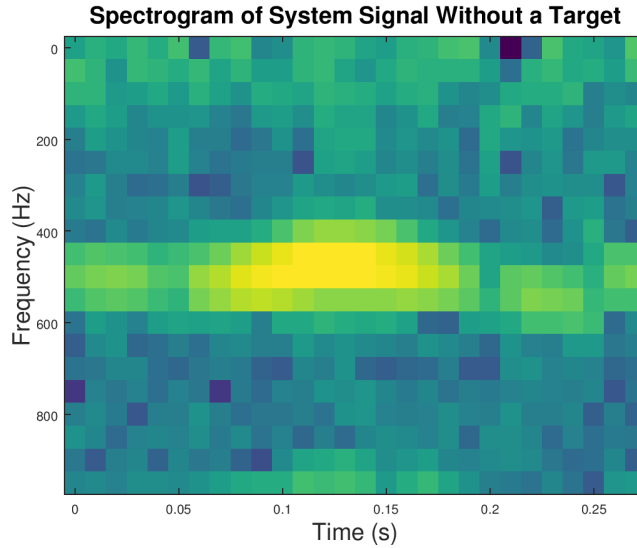


Figure 5.14: Time Varying Signal from Spinning Mask System With a Circular Target

of constant amplitude with no variation in time. Looking to Figure 5.14, we see that the frequency components drift in time, caused by the wobble of the spinning mask. As stated before, techniques exist to correct for the wobble. We can reattach the spinning mask to the motor more carefully (this was our first attempt) and get more practice. More reliably, we can use a computational technique developed by Jeffrey Field and Randy Bartels to remove the effects of the wobble. Their work was intended for more conventional SPIFI systems, but the technique translates readily to our system. However, due to time constraints on our research, we are content with what we have.

We should take a moment to summarize what we have achieved in this chapter. Based upon our understanding of the limitations of the static modulation mask architecture, we proposed a system based on spinning modulation mask SPIFI techniques. Using previous spinning mask SPIFI as a guide, we developed a mathematical framework for recovering shape and size information from a target flowing in a microfluidic channel. By examining our mathematical model, we also were able to define certain conditions that must be met for the measurement to be useful. The limitations of the system were explored and defined. Once we had a good idea of what to expect, we actually constructed a simple version of our proposed

spinning mask system. Although we utilized visible light and opaque targets instead of near IR light and fluorescent dye tagged targets, the principles are the same. Analysis showed that the data collected was qualitatively consistent with what our theory predicted. As such, we have accomplished a preliminary validation of the theory, mathematical framework, and design of our spinning modulation mask system architecture.

The experimental evidence gathered in tests for the spinning mask system demonstrates, if only qualitatively, the potential power of the spinning modulation mask system architecture. More research is necessary to fully demonstrate the veracity of our claims and the effectiveness of our system, but we believe that the results in this thesis are strong enough to warrant further time and financial resources be allocated to continue research on the spinning mask system.

5.6 The Next Steps

Having established the potential of the spinning mask but run out of time and resources to continue ourselves, we will lay out what the the next logical research steps to incremental testing of our spinning modulation mask system architecture. Although we do not have the time to perform this testing, we want to provide a framework for the next researchers to continue our work. The ultimate goal of these tests will be to design a fully functional spinning mask modulation system that can measure the size and characterize the shape of red blood cells flowing through a microfluidic masks. We note that the outline below is similar to the outline for the static mask architecture, but with added steps to reflect additional capabilities.

The first logical step for testing our system is to use fluorescent targets instead of opaque targets to test the validity of the area function and the mathematical model we have derived. Quantitative size and shape measurement should be the goal for this iteration. The targets should be macroscopic (for ease of testing). For instance, applying fluorescent dye to a microscope slide (in an appropriate shape) can act as a simple target. In order to use fluorescent dye, it will also be appropriate to change the laser light source to one with an

appropriate wavelength, generally in the near IR. Note, although we used a Ti:Sapphire source in our experiments, no such requirement for cell measurement. Ti:Sapphire is often used in SPIFI due to its ability to produce femtosecond pulses, which have applications in biological sample imaging. However, we need only to illuminate the target and activate its fluorescent dye. Excitation and emission properties will vary from between different dyes. However, inexpensive CW diode lasers with powers on the order of a few watts will likely be sufficient for our purposes. Further analysis of laser mode and power will depend upon the dye selected.

It will also be necessary to add a filter blocking the excitation beam light wavelengths from being collected on the detector, in order to measure only the light produced by the target fluorescing. The mask should be attached in order to minimize wobble, and the computational wobble correction techniques need to be utilized. Should quantitative measurements of the target size and shape be achieved, the research can proceed to a more sophisticated system.

The next logical step is to design the system to handle static microscopic targets. Fluorescent microspheres are an excellent analog to red blood cells. Additional lenses will need to be added to magnify the target, and the set up will need to be well shielded to minimize the signal to noise ratio due to stray light. Once again, quantitative size and shape measurements from the area function are required before moving to the next step.

Once static microscopic targets can be measured, a microfluidic channel and flow system ought to be added. Fluorescent microspheres flowing through the channel will be used as targets. The flow system must be capable of sending one target through the excitation field region at a time and must be able to control flow speed. So long as quantitative size and shape measurements are achieved, the system can move onto using red blood cells as targets. Once accurate measurements are demonstrated, the system can move onto the final stage of validation. We also note that if quantitative shape and size measurements are achieved with flowing microscopic targets, the spinning mask architecture can also be used for flow induced

shear stress cell elasticity measurements. A multistage approach (with two spinning masks) can first measure characterize the unstretched cells, and then measure their shape and size when under shear stress. The spinning mask architecture provides the key benefit of being less expensive (both financially and computationally) than the CCD cameras currently used in flow induced shear force cytometry. The multistage approach should also be investigated and its performance compared to that of the static mask architecture in such situations.jn

The last addition to the system is an optical stretcher. It will need to be set such that it can stretch and release a target cell while in the excitation beam (and as such, should use a frequency of light blocked by a filter to prevent signal noise at the detector). Measurement of cell size and shape while undergoing stretching and relaxation is the goal of this phase. Computations of cell elasticity should be checked for consistency with other measurement techniques. Once results achieve an equivalent (or adequate) precision and accuracy with the current state of the art, the research phase is complete.

If the system can demonstrate its effectiveness on stretching and relaxing blood cells, the engineering problems can be examined. Issues such as miniaturization, portability, simplicity, and cost ought to be addressed first. After that, expanding the system functionality is worth considering. For instance, being able to measure multiple targets at once (by having the occupy different flow streams), along with other methods of parallelization should be tested in order to increase throughput. A specialized computer program, (or even using a dedicated microprocessor/FPGA (Field Programmable Gate Array)) should be designed to streamline data analysis and make it automated. Such dedicated computational systems increase the speed of converting signal measurements into useful data. If fact, for certain medical diagnostic applications, real time (or near real time) cell elasticity measurements would be incredibly useful. These sorts of technical challenges, while a long way off, are worth bearing in mind during the research and development process.

CHAPTER 6

UNTIL NEXT TIME, DEAR READER

Over the course of this research, we designed, developed, analyzed two system architectures for the measurement of various red blood cells characteristics while moving in a microfluidic channel. The first relied on the use of a static SPIFI mask, while the second made use of a spinning SPIFI mask. In this chapter, we will review and summarize our approach, methods, and results from our research.

6.1 A Quick Review

We first review our work on the static mask system. We started by creating a Octave program that uses matrix representations of a target and mask to determine the form of the signal produced by the target flowing beneath the modulation mask. We were able to do so due to the similarities of discrete convolution and the physical process of the fluorescent target light being blocked and transmitted by the modulation mask. After some sanity checks, we used the program to model targets in various flow positions flowing beneath two rudimentary masks: one with three different spatial frequencies and one with five. We demonstrated that such masks could crudely determine the flow position of a target within a microfluidic channel through examination of the presence of specific frequencies in the periodogram of the signal produced. Further examination and reasoning showed that target size measurement can be achieved to arbitrary precision by adding more rows of different spatial frequencies and reducing their depth.

We then took a brief aside to discuss femtosecond laser micromachining as a method of producing high quality modulation masks inexpensively. Besides the cost, femtosecond laser micromachining of masks allows for highly flexible mask and modulation geometry, giving researchers more options in pursuing new mask configurations. We then built an apparatus to qualitatively test our ability to measure the size and flow position of a target. Using a

conventional 2D SPIFI mask (provided courtesy of Nathan Worts and his femtosecond laser micromachining system), possessing a large number of different frequencies with each row having a small depth, we tested the micromachined masks using a laser beam produced by a diode laser ($\lambda = 635$ nm) and a Titanium Sapphire laser ($\lambda = 800$ nm). Our experiment yielded two key results. First, we demonstrated for the first time that these femtosecond laser micromachined masks were effective at modulating visible and infrared light. The ability to modulate light in the infrared spectrum is especially important, as that wavelength is often used in conventional biological SPIFI applications. It also allows us to use these masks for our later experiments. The second result showed that a fluorescent target (modeled as the laser beam) flowing beneath a static modulation mask produces a time varying intensity signal, that through analysis of its frequency components, can yield information about the size of the target in the direction perpendicular to its flow. While not surprising (due to its similarity to conventional SPIFI), this result was useful as it was consistent with what our model predicts and with our analysis of cruder modulation masks. We also reasoned that if the depth of the individual modulation rows was sufficiently small, we could recover information about the shape of the target by examining the shape of the periodogram. The Gaussian shape of the periodogram being similar to the Gaussian profile of the laser beam was our first indication that prompted our consideration into this possibility. We set the issue of mathematical analysis of shape recovery aside for a short time due to limitations of the static mask architecture.

We then reviewed the capabilities and limitations of using a static modulation mask for measurement of red blood cell shape and size. We determine that the system ought to be capable of making precise measurements of flow position, size, and even shape of a target in a microfluidic channel provided that its shape and size were not time evolving. But recalling our overall goal, we considered the system effectiveness for a cell undergoing stretching (and subsequent relaxation) for the purposes of cell elasticity measurements. We noted that a cell undergoing shape change with respect to time would cause the frequency components

of the intensity signal produced to drift in time as well, requiring the use STFT (or similar methods) to examine the way the spectra time evolves. Given the consequences of the Gabor uncertainty principle, the scale of red blood cell relaxation times, and the geometry of the modulation mask and target, we determined that it would be difficult to accurately measure the size of the cell as it changes with respect to time. The static modulation mask has its applications, but would not achieve our main goal. However, we do believe that research on the static mask system is a worth while endeavor. What it lacks in ability compared to our other proposal is made up for from simplicity and lack of moving parts. Testing should be performed on both the primitive mask and a conventional static SPIFI mask. We already derived a way of extracting the area function using linear signals theory for the primitive mask, but an area function model must be derived for a conventional static SPIFI mask. Fortunately, the approach is nearly identical to the one we used for the spinning mask. The testing process taken is not specifically outlined here, but will generally follow the one laid out for the spinning mask architecture (sans any testing involving stretching the cells).

To solve the issue of size measurement whilst the cell undergoes relaxation, we designed our second proposed system which uses a spinning SPIFI mask architecture. We began by developing a thought experiment on cell size measurement with a conventional spinning mask SPIFI microscope. We found that by uncoupling the frequency modulation from the flow speed of the target, we had a great degree of freedom with which to optimize our system to deal with STFT analysis. By recognizing a similarity of the effective (not real, since it is produced by the cell moving) modulation field of a static modulation mask with that of a two dimensional spinning mask SPIFI system, we realized that we could convert a spinning mask produced modulated line cursor to an extended two dimensional excitation beam with modulation in only one direction. Such a modulation field is equivalent to how the static modulation mask system operates but without the dependence upon target velocity within the flow. We laid out general system architecture to provide a framework for mathematical modeling and laboratory experimentation.

We then set to deriving a model for mathematically describing signals produced by our spinning mask system. Using the original spinning mask SPIFI derivation as a guide, we were able to define the expected signal produced by a fluorescing target in terms of a double integral over its shape, fluorescent dye distribution, and mask parameters. We could now determine the flow position and the extent of a target in the direction perpendicular to its flow, even if the shape is time evolving. We opted to take it a step further. By recalling our arguments about how some shape information is contained in the shape of the periodogram, we recast the integral in terms of what we called an “area function”, which is a one dimensional representation of the two dimensional shape information of the target. We then showed that, so long as certain requirements are met, shape information can be recovered from the area function. We also note that a similar derivation for shape recovery using a static mask can be readily performed using the same approach we used.

Next, we constructed a simple apparatus in order to qualitatively test our theory on macroscopic targets. We first examined the periodogram produced by the laser beam, as we were able to treat it as a fluorescent target. We found that the periodogram we recovered was qualitatively consistent with what our model predicted for a roughly Gaussian laser beam. We used laser micromachined circular opaque targets on microscope slides instead of fluorescent targets due to ease of construction and limitations on resources and time. Again, we found that the periodogram was qualitatively consistent with the predictions of our mathematical model. We then noted the imperfections of our system caused due to mask wobble, which causes blurring of shape of the periodogram, and stated that future work should take advantage of existing wobble correction techniques utilized by SPIFI microscopy users. However, we were satisfied that we had demonstrated the potential of a spinning mask system to measure flow position, shape information, and size (to include time evolving size).

We then provided an outline of what steps ought to be taken next to further validate our proposed spinning mask system. Each iteration moves closer to a fully functional design. While we wish we could carry out these steps ourselves, we are short on a critical resource:

time. The temporal restrictions imposed by the nature of this thesis preclude us from seeing the research to its completion. However, we believe that the results we have shown in this thesis do warrant further research. Of the two system designs we present in this thesis, we believe that the bulk of any financial and manpower resources ought to be dedicated to the spinning mask system due to its applications in cell elasticity measurement. Ideally, the work should be undertaken by an individual or team with a background in optical system design, signal processing, and a basic understanding of conventional SPIFI techniques.

6.2 A Final Farewell

Our research has presented two system designs, based on conventional SPIFI techniques. The static mask has the potential for use in flow position, target shape, and target size measurement of constant shape. Such a simple system may have applications in cell sorting applications and more. Our second system design, utilizing a spinning mask, has the ability to perform the previous measurements and do so while the target size is changing, lending itself directly to cell elasticity cytometry. Given the potential medical research implications of a fast, cheap, and deployable system to take these measurements, we strongly believe that our work ought to be continued. We hope that one day, spinning mask based cell elasticity cytometers will help medical researches learn more about disease and human health. We pursued this research so vigorously because we believe it has the potential to help people. We strongly urge others to take up the torch that we can no longer bear, so that the full potential of this research to reduce human suffering may one day be realized.

REFERENCES CITED

- [1] I. Sraj *et al.* Cell Deformation cytometry using diode-bar optical stretchers. *J. Biomed. Opt.*, **15**, 2010.
- [2] C.T. Lim M. Dao and S. Suresh. Mechanics of the human red blood cell deformed by optical tweezers. *Journal of Mechanics and Physics of Solids*, **51**:2259–2280, 2003.
- [3] Chwee T. Lim Gabriel Y.H. Lee. Biomechanics approaches to studying human diseases. *Trends in Biotechnology*, **25**:111–118, 2007.
- [4] Sraj I. *et al.* Erythrocyte deformation in high-throughput optical stretchers. *Physical Review E*, **85.4**, A.D. 2012.
- [5] Roth *et al.* Imaging of a linear diode bar for an optical cell stretcher. *Biomedical optics express*, **6.3**:807–814, 2015.
- [6] Frederick J Schoen Jack E Lemons Buddy D. Ratner, Allan S. Hoffman, editor. *Bio-materials Science: An Introduction to Materials in Medicine, 2nd Edition*. Elsevier, 2004.
- [7] A. Ashkin. Acceleration and Trapping of Particles by Radiation Pressure. *Phys. Rev. Lett.*, 24:156–159, Jan 1970. doi: 10.1103/PhysRevLett.24.156. URL <https://link.aps.org/doi/10.1103/PhysRevLett.24.156>.
- [8] H Mahmood T J Moon CC Cunningham J Guck, R Ananthakrishnan and J Kas. The Optical Stretcher: A Novel Laser Tool to Micromanipulate Cells. *Biophysical Journal*, 81.2:767–784, 2001.
- [9] Jeffery S. et al Sanders. Imaging with frequency-modulated reticles. *Optical Engineering*, **30**:1720–1724, 1991.
- [10] Jeffery J. Field et al. Superresolved multiphoton microscopy with spatial-frequency modulated imaging. *Proceedings of the National Academy of Sciences of the United States of America*, **113**(no. 24):6605–6610, 2016.
- [11] Michael D Young et al. A pragmatic guide to multiphoton microscope design. *Advances in Optics and Photonics*, **7**:276–378, 2015.
- [12] Rebecca M. Williams Warren R. Zipfel and Webb Watt W. Nonlinear magic: multiphoton microscopy in the biosciences. *Nature Biotechnology*, **21**:1369–1377, 2003.

- [13] RKP Benninger and Piston DW. Two-Photon Excitation Microscopy for the Study of Living Cells and Tissues. *Current protocols in cell biology / editorial board, Juan S Bonifacino et al.*, 2013.
- [14] Alberto Diaspro *et al.* Multi-photon excitation microscopy.
- [15] Gina Eldridge. *Spatial Frequency Modulation for Imaging with Incoherent Light Sources*. Master's thesis, Colorado School of Mines, 2016.
- [16] David G. Winters Greg Futia, Phillip Schlup and Randy A. Bartels. Spatially-chirped modulation imaging of absorption and fluorescent objects on single-element optical detector. *Optical Express*, **19**:1626–1640, 2011.
- [17] Jeffrey J. Field and Randy A. Bartels. Digital aberration correction of fluorescent images with coherent holographic image reconstruction by phase transfer (CHIRPT). *Proc. SPIE*, page 97130B, 2016.
- [18] David G. Winters and Randy A. Bartels. Two-dimensional single-pixel imaging by cascaded orthogonal line spatial modulation. *Optics Letters*, **40**:2774–2777, 2015.
- [19] David G. Winters. *Advances in single-pixel imaging towards biological applications*. PhD thesis, Colorado State University, 2014.
- [20] Greg Futia Philip Schlup and Randy Bartels. Lateral tomographic spatial frequency modulated imaging. *Applied Physics Letters*.
- [21] Steffen Hard and Friedhelm Schönfeld, editors. *Microfluidic Technologies for Miniaturized Analysis Systems*. Springer.
- [22] John M. Cimbala Yunus A. Cengel. *Fluid Mechanics: Fundamentals and Applications*. McGraw-Hill, 2006.
- [23] Silvia Maria Alessio. *Digital Signal Processing and Spectral Analysis for Scientists: Concepts and Applications*. Springer, 2016.
- [24] Ronald W. Schafer Alan V. Oppenheim and John R. Buck. *Discrete-Time Signal Processing 2nd Edition*. Prentice Hall, 1999.
- [25] Springer Series in Optical Science. *Solid-State Laser Engineering*. Springer, 2006.
- [26] Jeff Field Randy Bartels Jason Jones Nathan Worts, Michael Young and Jeff Squier. Fabrication and Characterization of Modulation Masks for Multimodal Spatial Frequency Modulated Microscopy. Forthcoming.
- [27] *Springer Handbook of Nanotechnology, 4th Edition*. Springer, 2010.

APPENDIX A

OCTAVE CODE FOR STATIC MASK SIGNAL PREDICTION

This appendix contains the GNU Octave code used for static modulation mask signal prediction. The code should be completely compatible with MathWorks MATLAB, though it has not been tested in it. This code and structure should also be simple to port over into Python. The Octave code is also included in Appendix C.

A.1 Detector Output Waveform Modeling

Figure A.1 contains the Octave code for the computation of detector output with various targets and static modulation masks.

```
% ModelWaveform Function: Version 3
% Author: Jacob Neumann
% Created: 29 January 2017
% [Intensity,Length] = ModelWaveform(Target,Mask) computes the predicted waveform on a PMT or photodiode
% when the target (Target) is passed under the mask (Mask).
% Function returns the intensity waveform vector and the length of the vector
% # Rows of Target must = # Rows of Mask

function [Intensity,Length] = ModelWaveform2 (Target, Mask) % Returns predicted waveform and length of the signal.

DepthMask = size(Mask,1); % # of rows in mask matrix
DepthTarget = size(Target,1); % # of columns in target matrix

if DepthTarget > DepthMask % Error Message
    disp('Error: Depth of Target is greater than depth of Mask')
    return
elseif DepthTarget < DepthMask % Error Message
    disp('Error: Depth of Target is less than depth of Mask')
    return
end

Length = size(Target,2) + size(Mask,2)-1; #Length due to length of the convolution of two vectors.
IntensityVec = zeros(1,Length); %Instantiate Intensity vector

for i = 1:DepthMask % Iterate through all rows of the target and mask matrices.
    Y = conv(Mask(i,:),Target(i,:)); % Convolve rows of target and mask
    IntensityVec = IntensityVec + Y;
end

Intensity = IntensityVec;
endfunction
```

Figure A.1: Octave code for Detector Output Waveform Modeling

A.2 Octave Code for Creating a Matrix Representation Circular Target

Figure A.2 contains the Octave code for computing a matrix representation of general circular targets. This code is used in concert with the detector output waveform modeling code in Appendix A.1.

```
% CircTarget Function v2
% Author: Jacob Neumann
% Created: 16 April 2016
%
% [Target] = CircTarget(n) creates a matrix representing a circular target of diameter n
%
% n must be an even number

function [Target] = CircTarget (n)

f = @(x) sqrt((n/2)^2 - x.^2); % Define upper half of circle

x = linspace(-n/2,n/2,n);      % Define sampling points

y = round(f(x));              % Sample and round

onesvec = 4*floor(y/2);        % Vector states how many ones in each row, forces them to be even

Target = zeros(n,n);          % Instantiate Target vector

% Loop iterates through rows of target, creates onesvec(i) ones centered, rest are zeros
for i = 1:n
    Target(i,:) = [zeros(1,(n - onesvec(i))/2),ones(1,onesvec(i)), zeros(1,(n - onesvec(i))/2)];
end

endfunction
```

Figure A.2: Octave code for Matrix Representation of Circular Targets

APPENDIX B

FURTHER EXPLORATION OF THE AREA FUNCTION

In this appendix, we utilize *Mathematica* to demonstrate that our definition of the area function in Equation 5.13 and Equation 5.9 gives us the same result as in Equation 5.7. We consider two carefully chosen test cases: a circular target and a square target. It turns out that these integrals can be challenging for even *Mathematica* perform analytically. While it took some very scientific “messaging around”, we eventually found physically realistic sizes and positions for our target that yield analytical answers from *Mathematica*. We would expect less convenient test cases to work just fine if computed numerically, but we wanted to show exact equivalence in a way that only analytical functions really can. The *Mathematica* notebook is contained in Figure B.1, Figure B.2, Figure B.3, and Figure B.4. The *Mathematica* notebook is also contained in Appendix C.

Equivalency of the Area Function with the Standard Approach

The Standard Approach - The Circular Target

The standard, unsimplified method relies on using a double integral in x and y and yields a signal in the time domain. In standard SPIFI, since there is no y component, it is easy to make the integral for the time domain signal look like a Fourier Transform, but alas, we have not that luxury. We start by defining a fluorescent circular target of radius $\frac{1}{2}$, centered at $x = \frac{1}{2}$ and $y = \frac{1}{2}$. This way, the target lies completely in quadrant I of the real plane. This makes the math a lot more convenient.

```
In[50]:= a = 1/2;  
b = 1/2;  
r = 1/2;  
F[x_, y_] =  
Piecewise[{{1, r^2 >= (x - a)^2 + (y - b)^2}, {0, r^2 < (x - a)^2 + (y - b)^2}}]  
Out[52]:= 
$$\begin{cases} 1 & \frac{1}{4} \geq \left(-\frac{1}{2} + x\right)^2 + \left(-\frac{1}{2} + y\right)^2 \\ 0 & \text{True} \end{cases}$$

```

Next, we compute the function for the time domain signal using the double integral. Note, we force the y integration to take place first, as Mathematica does not return a "nice" answer otherwise. These sorts of integrals can be rather challenging to perform analytically.

```
In[63]:= Integrate[(F[x, y]) Cos[2 π y t], {y, 0, 1}, {x, 0, 1}]  
Out[63]:= 
$$\frac{\text{BesselJ}[1, \pi t] \text{Cos}[\pi t]}{2 t}$$

```

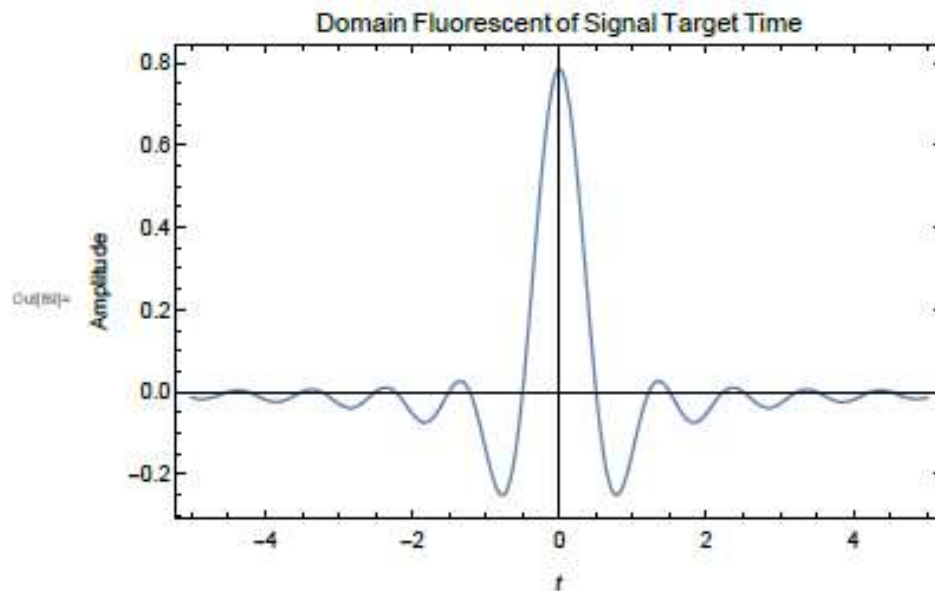
We find that, without a window function, our time domain signal produced by a fluorescent circular target will be an oscillating function. Note that while the signal shown here is negative at times (which is unphysical), the result is still valid. We are actually computing the signal corresponding to the first sideband: there is a DC component that, while present, is not terribly relevant to our discussion.

Figure B.1: Page 1 of Mathematica Notebook

```

In[88]:= Plot[ $\frac{\text{BesselJ}[1, \pi t] \text{Cos}[\pi t]}{2 t}$ , {t, -5, 5},
PlotRange -> All, Frame -> True, FrameLabel -> {t, Amplitude},
PlotLabel -> Time Domain Signal of Fluorescent Target, LabelStyle -> {12}]

```



Taking the Fourier Transform of the signal, we recover what we have previously defined as the "area function". We will want to compare it to our mathematical definition of the area function using our work around.

```

In[89]:= H[ $\omega$ _] = FourierTransform[ $\frac{\text{BesselJ}[1, \pi t] \text{Cos}[\pi t]}{2 t}$ , t,  $\omega$ , FourierParameters -> {1, 1}]

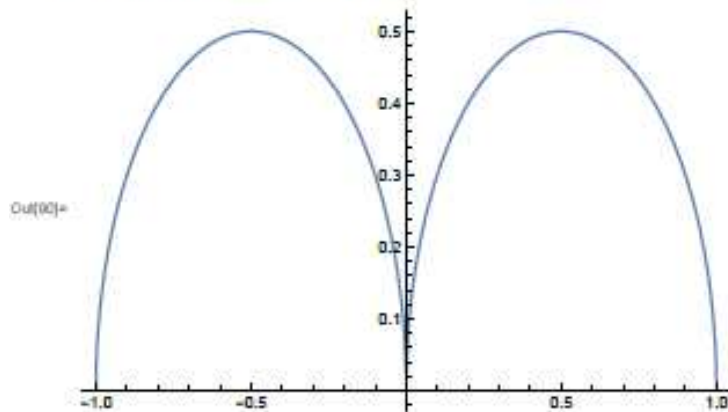
```

$$\text{Out[89]} = \frac{1}{2} \left(\frac{\sqrt{-2 \pi \omega - \omega^2}}{\pi} + \frac{\sqrt{2 \pi \omega - \omega^2}}{\pi} - \frac{\sqrt{2 \pi \omega - \omega^2} \text{UnitStep}\left[1 - \frac{\pi^2}{(\pi - \omega)^2}\right]}{\pi} - \frac{\sqrt{-2 \pi \omega - \omega^2} \text{UnitStep}\left[\frac{\omega (2 \pi + \omega)}{(\pi + \omega)^2}\right]}{\pi} \right)$$

The Fourier Transform is entirely real, so we can plot it directly.

Figure B.2: Page 2 of Mathematica Notebook

```
In[93]= Plot[H[2 π f], {f, -1, 1}]
```



Interesting. We see zeros at $f = 0$ and $f = 1$, which makes sense based upon the size of the target. The widest point in the x direction of the target is at $y = 0.5$, which corresponds to a maximum in the plot above. Note that the above is the Fourier Transform. In a laboratory setting, we would be most often computing the one sided periodogram. The periodogram of the above Fourier Transform would just be the positive frequency peak multiplied by two.

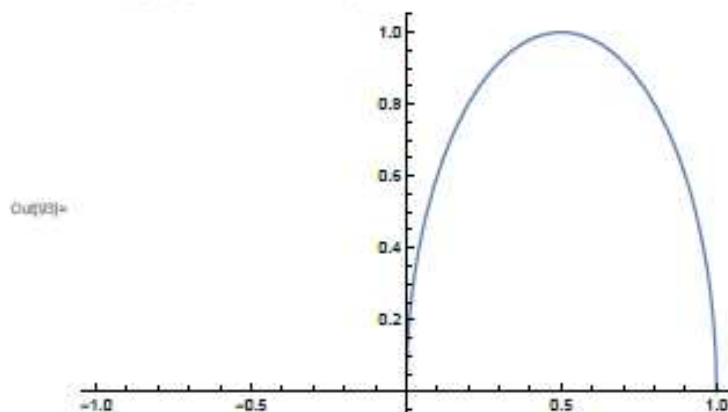
The Area Function Definition - The Circular Target

Now, we must test the veracity of our claim that the area function can be computed using a single integral. We first compute the area function (based on our mathematical definition) for our target.

```
In[94]= G[y_] = Integrate[F[x, y], {x, 0, 1}]
```

$$\text{Out[94]= } \begin{cases} 1 & y = \frac{1}{2} \\ 2\sqrt{-(-1+y)y} & 0 < y < \frac{1}{2} \text{ || } \frac{1}{2} < y < 1 \\ 0 & \text{True} \end{cases}$$

```
In[95]= Plot[G[y], {y, -1, 1}]
```



This looks rather familiar. In fact, it looks exactly like what we would expect the one sided periodogram of the Fourier Transform of the standard approach time domain signal. It has the right shape, the zeros

Figure B.3: Page 3 of Mathematica Notebook

in the right places and a maximum that makes sense. Lets compute its Fourier Transform, since we claim that the time domain signal (sans the window function) is equal to the Fourier Transform of the area function. We must not forget to take the real part of the Fourier Transform, as we required in our derivation.

```
In[94]:= FullSimplify[Re[FourierTransform[G[y], y, 2 π t, FourierParameters → {1, 1}]],
Assumptions → t ∈ Reals && t > 0]
Out[94]= 
$$\frac{\text{BesselJ}[1, \pi t] \text{Cos}[\pi t]}{2 t}$$

```

This gives us the exact same time domain signal that we had before. Outstanding.

A Second Case - The Square Target

We consider another simple case to test the validity of our definition of the area function: that of a square target. We define our target to be a square of height and width equal to unity, centered at $x = \frac{1}{2}$ and $y = \frac{1}{2}$, just as we did for the circular target.

```
In[94]:= F1[x_, y_] = Piecewise[{{(1, 0 ≤ x ≤ 1 && 0 ≤ y ≤ 1), (0, x > 1 || y > 1)}}]
Out[94]= 
$$\begin{cases} 1 & 0 \leq x \leq 1 \ \&\& \ 0 \leq y \leq 1 \\ 0 & \text{True} \end{cases}$$

```

Using the "brute force" tactic that does not use a Fourier Transform, we compute the signal produced by a fluorescent square target.

```
In[95]:= Integrate[F1[x, y] Cos[2 π y t], {y, 0, 1}, {x, 0, 1}]
Out[95]= 
$$\frac{\text{Sin}[2 \pi t]}{2 \pi t}$$

```

A Sinc function: fascinating. But does our predicted area function give us the same result? We compute the area function using our definition.

```
In[96]:= G1[y_] = Integrate[F1[x, y], {x, 0, 1}]
Out[96]= 
$$\begin{cases} 1 & 0 \leq y \leq 1 \\ 0 & \text{True} \end{cases}$$

```

We take the real part of the Fourier Transform of the area function as we did before.

```
In[104]:= FullSimplify[Re[FourierTransform[G1[y], y, 2 π t, FourierParameters → {1, 1}]],
Assumptions → t ∈ Reals && t > 0]
Out[104]= 
$$\frac{\text{Cos}[\pi t] \text{Sin}[\pi t]}{\pi t}$$

```

By recalling that $\text{Cos}[\pi t] \text{Sin}[\pi t] = \frac{\text{Sin}[2 \pi t]}{2}$, we see that the Fourier Transform of the area function is $\frac{\text{Sin}[2 \pi t]}{2 \pi t}$, as was required using the brute force method.

Figure B.4: Page 4 of Mathematica Notebook

APPENDIX C

SUPPLEMENTAL ELECTRONIC FILES

The supplemental electronic files contain two categories of code: Octave code, and a *Mathematica* notebook. The Octave code has two files. The first is `ModelWaveform2.m`, which contains the code to compute predicted detector output, as shown in Appendix A.1. The second Octave file is `CircTarget.m`, which contains code to output a matrix representation of a circle of arbitrary size, as shown in Appendix A.2. The *Mathematica* notebook, titled `Area_Function_Equivalence.nb`, contains the *Mathematica* code used to demonstrate the equivalence of the area function definition with a brute force integration for our spinning mask architecture, as shown in Appendix B. While the code in these supplemental files is included in the other appendices, we believe that it is good manners to include them in digital form as well, for easy use and editing.